

Prediction of mobility, handling, and tractive efficiency of wheeled off-road vehicles

Carmine Senatore

Dissertation submitted to the Faculty of the
Virginia Polytechnic Institute and State University
in partial fulfillment of the requirements for the degree of

Doctor of Philosophy
in
Engineering Mechanics

Dr. Shane Ross, Co-Chair
Dr. Corina Sandu, Co-Chair
Dr. Mark Cramer
Dr. Norman Dowling
Dr. Scott Hendricks

May 3, 2010
Blacksburg, Virginia

Keywords: energy efficiency, fuel economy, multi pass
lateral force, torque distribution, tractive efficiency
tire dynamics, off-road, tire soil interaction

Copyright 2010, Carmine Senatore

Prediction of mobility, handling, and tractive efficiency of wheeled off-road vehicles

Carmine Senatore

ABSTRACT

Our society is heavily and intrinsically dependent on energy transformation and usage. In a world scenario where resources are being depleted while their demand is increasing, it is crucial to optimize every process. During the last decade the concept of *energy efficiency* has become a *leitmotif* in several fields and has directly influenced our everyday life: from light bulbs to airplane turbines, there has been a general shift from pure performance to better efficiency.

In this vein, we focus on the mobility and tractive efficiency of off-road vehicles. These vehicles are adopted in military, agriculture, construction, exploration, recreation, and mining applications and are intended to operate on soft, deformable terrain.

The performance of off-road vehicles is deeply influenced by the tire-soil interaction mechanism. Soft soil can drastically reduce the traction performance of tires up to the point of making motion impossible. In this study, a tire model able to predict the performance of rigid wheels and flexible tires is developed. The model follows a semi-empirical approach for steady-state conditions and predicts basic features, such as the drawbar pull, the driving torque and the lateral force, as well as complex behaviors, such as the slip-sinkage phenomenon and the multi-pass effect. The tractive efficiency of different tire-soil configurations is simulated and discussed. To investigate the handling and the traction efficiency, the tire model is implemented into a four-wheel vehicle model. Several tire geometries, vehicle configurations (FWD, RWD, AWD), soil types, and terrain profiles are considered to evaluate the performance under different simulation scenarios. The simulation environment represents an effective tool to realistically analyze the impact of tire parameters (size, inflation pressure) and torque distribution on the energy efficiency. It is verified that larger tires and decreased inflation pressure generally provide better traction and energy efficiency (under steady-state working conditions). The torque distribution strategy between the axles

deeply affects the traction and the efficiency: the two variables can't clearly be maximized at the same time and a trade-off has to be found.

Acknowledgments

I am heartily thankful to my advisors, Dr. Shane Ross and Dr. Corina Sandu, whose encouragement, guidance and support helped me achieve my goals. I wish to also thank the members of my Ph.D. committee for their valuable time and suggestions in improving upon my research work.

I am grateful to Dr. Brendan Juin-Yih Chan for the work he has done on off-road tire modeling: his research has been inspirational for my thesis. For all the helpful suggestions and encouragements, I thank my friends and fellow students of the ESM department, Piyush Grover, Phanindra Tallapragada, and Amir Ebrahim Bozorg Magham.

I truly appreciate the friendship and encouragements I received from my friends Kaushik Das, Bob Simonds, Jose Herrera-Alonso, Gabriela Lopez-Velasco, Tom Pardikes, Kevin Bierlein, Golnaz Taghvatalab. A special thanks goes to Nancy and Gary Rookers for their constant encouragement and help. During the last five years many Italians crossed my path in Blacksburg, a dynamic group of lovely and exquisite persons: Matteo Alvaro, Attilio Arcari, Vincenzo Antignani, Andrea Apolloni, Fabrizio Borghi, Gabriele Enea, Rosario Esposito, Letizia Imbres, Paolo Finotelli, Davide Locatelli, Andrea Mola, Marta Murreddu, Maurizio Paschero, Silvia Perotta, Massimiliano Rolandi, Giovanni Sansavini, Davide Spinello.

It has been an honor for me to meet with Edoardo Nicoli, a sincere friend, a wise counselor, and an extraordinary bicycle mate. I am grateful to Fabrizio Re, for his support and friendship during my years in Milan. I would like also to thank my *old* friends Paolo Avagliano, Antonio Castaldo D'Ursi, and Andrea Salerno: three wonderful persons that never stopped to inspire, support, and help me.

This thesis would not have been possible without the love and the encouragement of my family: my father Antonio, my mother Teresa, and my sister Danila have always supported me and they helped me realizing my dreams.

Finally, I would like to express my gratitude to Anna Laura for her love and patience. She has always been a source of inspiration and motivation, I am forever indebted to her.

Contents

- 1 Introduction** **1**
- 1.1 Preface 1
- 1.2 Problem Statement 4
- 1.3 Research Objectives 5
- 1.4 Research Contribution 7
- 1.5 Dissertation Outline 7

- 2 Review of Literature** **9**
- 2.1 Tire Mechanics Terminology 9
- 2.2 Tire History and Evolution 12
- 2.3 Terramechanics Approach to Tire-Terrain Modeling 13
 - 2.3.1 Empirical Methods 14
 - 2.3.2 Semi-Empirical Methods 17
 - 2.3.3 Analytical Methods 19
 - 2.3.4 Finite Element Methods 21
- 2.4 Off-Road Vehicle Dynamics 22
- 2.5 Tractive Efficiency 24
- 2.6 Review of Literature Summary 26

- 3 Tire Model Development** **27**
- 3.1 Pressure-Sinkage Equation 27

3.1.1	Discussion on the Use of the Reece Equation for Tire Stress Distribution Estimation	30
3.2	Shear Stress	30
3.3	Normal and Tangential Stress Distribution	31
3.4	Rigid Wheel and Flexible Tire	35
3.5	Drawbar Pull, Driving Torque, and Lateral Force	37
3.6	Multi-Pass Effect	40
3.7	Results	43
3.7.1	Dry Sand - Rigid Wheel	44
3.7.2	Moist Yolo Loam - Flexible Tire	47
3.8	Considerations	49
4	Tractive Efficiency	51
4.1	Power-train Efficiency	52
4.1.1	Internal Combustion Engine	52
4.1.2	Electric Motor	55
4.2	Aerodynamic Efficiency	55
4.3	Tractive Efficiency	57
5	Vehicle Model Development	61
5.1	Mathematical Model	61
5.1.1	Equations of Motion	62
5.1.2	External Forces	66
5.1.3	Internal Forces	70
5.1.4	Tire Forces Generation Process	71
5.1.5	Velocity Controller	74
5.1.6	Torque Distribution	74
5.1.7	Vehicle Parameters	75

5.2	Vehicle Model Validation	75
5.2.1	Acceleration and Braking	76
5.2.2	Double Lane Change	78
5.3	Results	81
5.3.1	Dry Sand Longitudinal	82
5.3.2	Moist Yolo Loam Longitudinal	88
5.3.3	Dry Sand Lateral	93
5.3.4	Moist Yolo Loam Lateral	95
6	Conclusions and Future Work	97
6.1	Research Summary and Contribution	97
6.2	Recommendations for Future Research	98
	Bibliography	100

List of Figures

1.1	Renewable energy sources worldwide at the end of 2008 [1].	2
1.2	Energy flow in a typical mid-size car traveling on flat, hard surface. (Reprinted from [2] , obtained from Transportation Research Board Special Report 286 under the FOIA.)	4
2.1	Definition of the tire axis system and most relevant quantities according to SAE J670e [3].	11
2.2	Construction layout of a bias-ply (a) and a radial-ply (b) tire. Adapted from [4]	13
2.3	Descriptive plot of a wheel rolling into soft terrain.	21
2.4	Definition of the vehicle axis system according to SAE J670e [3].	23
2.5	Torque <i>flow</i> in a four wheel drive vehicle. The torque produced by the engine is split by the central differential and reaches the axles. At the axles is split again by the axles differentials delivered to the wheels. Arrows' length is not proportional to torque magnitude; the axle differentials always split the torque equally between the axles.	26
3.1	A schematic representation of the bevameter test. A load is applied on a penetrometer while sinkage z and normal pressure σ_n are recorded. The experimental data is then fitted with (3.1).	29
3.2	(a) An example of a deformed tire driven on a soft surface. The tire is deforming and sinking into the ground. (b) A detail of the contact patch area. The normal stress σ_n and the tangential stress τ_x acting along the contact patch are shown.	32
3.3	A schematic representation of the normal stress distribution as adopted by Harnisch et al. [5] and by Wong at al. [6]. In this study, Wong's approach is used.	33

3.4	(a) Normal stress distribution along the contact patch of a driven ($s_d = 0.2$) rigid wheel. The stress increases from the entry angle θ_e , reaches the maximum at θ_m , and decreases back to zero at the exit angle θ_b . (b) Tangential stress distribution along the contact patch under the same assumptions.	34
3.5	Exaggerated plot of a deformed tire sitting on hard surface (a) and driven on a soft terrain (b). When stationary the only portion in contact with the terrain is the flat region between θ_r and θ_f which in this particular configuration correspond to θ_b and θ_e . When the tire is rolling, the section of maximum deflection is rotated on an angle $\theta_m = \frac{\theta_f}{2}$ and the entry and exit angle $\theta_{e,b}$ don't necessarily correspond to θ_f and θ_r	36
3.6	A schematic representation of the lateral force generation. The lateral force is composed of two components: the shear force in the lateral direction F_{ys} and the bulldozing force F_{ybd} . The first one is due to the lateral slip of the tire imposed by the steering action. This force acts along the contact patch beneath the tire. The bulldozing force acts on the side of the tire and is due to the wheel compacting the terrain in the lateral direction.	39
3.7	Response to repetitive load of a mineral terrain.	41
3.8	Example of terrain properties variation for multiple passage. The data has been extrapolated from the Figure 25 of [7] and regards a loam soil with fine grained sand at 16.5% of moisture content.	42
3.9	Trend of drawbar pull (a) and driving torque (b) for different vertical loads and slip ratio. Results obtained for a rigid wheel running on dry sand.	44
3.10	Experimental data compared with the model prediction. Rigid wheels with different geometries have been tested on dry sand.	44
3.11	Slip-sinkage behavior of rigid wheels of different geometries.	45
3.12	Lateral force versus slip angle for different slip ratios (a) and vertical loads (b). Results obtained for a rigid wheel on dry sand.	45
3.13	Combined slip envelope for different slip angles (a) and vertical loads (b). Results obtained for a rigid wheel on dry sand.	46
3.14	Multi-pass influence on the performance of rigid wheels on dry sand. In (a) the longitudinal force is presented while (b) shows the relative sinkage.	47
3.15	Trend of drawbar pull (a) and driving torque (b) for different vertical loads and slip ratio. Results obtained for flexible tire on moist Yolo loam.	47

3.16	Variation of drawbar pull (a) with inflation pressure and trend of the sinkage (b) with inflation pressure. Results obtained for flexible tire on moist Yolo loam.	48
3.17	Lateral force versus slip angle for different slip ratio (a) and vertical load (b). Results obtained for flexible tire on moist Yolo loam.	48
3.18	Combined slip envelope for different slip angles (a) and vertical loads (b). Results obtained for flexible tire on moist Yolo loam.	49
3.19	Multi-pass influence on the performance of flexible tires on moist Yolo loam. (a) presents the variation of longitudinal force while (b) the relative sinkage for multiple passages over the same patch of terrain.	49
4.1	Energy requirement for two driving conditions [8].	52
4.2	Exemplar torque/power curve for an engine. The maximum output power is 120 kW at 3300 RPM, while the maximum torque is 270 Nm at 1450 RPM.	53
4.3	Map of a diesel engine. The power/torque specifications are the same as Figure 4.2. The <i>islands</i> represent lines of constant Brake Specific Fuel Consumption (BSFC), the grams of fuel burned to produce a kWh of energy. The maximum occurs close to 1600 RPM at full load (thicker boundary line). On the y -axis is the brake mean effective pressure (bmep), a measure of an engine's capacity to do work directly related to the torque.	54
4.4	Typical efficiency map for an electric motor for hybrid vehicles applications.	56
4.5	Tractive efficiency under different operational scenarios for a tire rolling on dry sand. In (a) different sizes and the multi-pass effect influence is showed. In (b) different loads are investigated.	59
4.6	Tractive efficiency under different operational scenarios for a tire rolling on moist Yolo loam. In (a) different inflation pressures, tire sizes, and the multi-pass effect influence is showed. In (b) different loads are investigated.	60
5.1	Schematic representation of the vehicle model. The earth-fixed reference frame X, Y, Z is showed and can be arbitrarily located. The vehicle motion is described in terms of the right-handed reference frame x, y, z attached to the vehicle center of gravity. The wheels displacement is constrained in the z -direction of the vehicle-fixed reference frame. To keep the plot clear the x', y', z' frame is illustrated in more detail in Figure 5.2.	63

5.2	Top-view of a vehicle during a right turn. The wheels reference frames x', y', z' are highlighted and the Ackermann steering geometry is presented.	66
5.3	A schematic representation of how the driver input is translated into actual driving forces at the wheels.	72
5.4	Longitudinal velocity of the vehicle during an acceleration and braking maneuver.	76
5.5	Pitch angle of the vehicle during an acceleration and braking maneuver.	77
5.6	Pitch angle of the vehicle during an acceleration and braking maneuver.	77
5.7	Trajectory followed by the vehicle during a double lane change maneuver.	78
5.8	Vehicle longitudinal velocity during a double lane change maneuver.	79
5.9	Vehicle roll angle during a double lane change maneuver.	79
5.10	Vehicle pitch angle during a double lane change maneuver.	80
5.11	Vehicle yaw angle during a double lane change maneuver.	80
5.12	Vertical load distribution during a double lane change maneuver. Solid lines: Model. Dashed lines: CarSim. The vertical load increases on the outer wheels and decreases on the inner ones due to dynamic weight transfer phenomenon.	81
5.13	(a) Velocity profile for a vehicle running on a flat dry sand terrain. The simulation starts from a slightly lower velocity in order to reach smooth steady state conditions. (b) The torque delivered at the tires during the maneuver.	82
5.14	(a) Sinkage distribution for the three vehicle configurations. The value of sinkage is relative to each wheel. (b) Vertical load distribution during the maneuver. When steady state conditions are reached the load transfer phenomena still persist because the tires are still producing longitudinal forces that influence the pitch angle of the vehicle.	83
5.15	(a) Sinkage distribution for the three vehicle configurations. The value of sinkage is relative to each wheel. (b) Vertical load distribution during the maneuver. When steady state conditions are reached the load transfer phenomena still persist because the tires are still producing longitudinal forces to overcome the resistance forces; this influence the pitch angle of the vehicle.	84
5.16	(a) Tire angular velocity and (b) instantaneous power requirement to move at 25 km/h on dry sand.	84

5.17	Power vs. torque distribution for a vehicle traveling at 25 km/h on flat dry sand. 0 % (100 %) on the x -axis means that the torque is fully biased on the front (rear) axle of the vehicle. On the same plot the slip difference between the front and rear axle is presented.	85
5.18	Power vs torque distribution for a vehicle traveling at 25 km/h on a 10 % incline. 0 % (100 %) on the x -axis means that the torque is fully biased on the front (rear) axle of the vehicle.	86
5.19	(a) Vehicle with a significant static load distribution unbalance during a straight run at 50 km/h on dry sand. (b) Power vs torque distribution among the axles.	86
5.20	Power requirement for four vehicle configurations. Vehicle speed is 50km/h and the terrain is flat dry sand. Nominal parameters (concerning the standard case) are: Radius = 0.4 m, Width = 0.265 m, Torque = 50%F - 50% R. . . .	87
5.21	(a) Velocity profile for a vehicle running on a flat loamy terrain. The simulation starts from a slightly lower velocity in order to reach smooth steady state conditions. (b) The torque delivered at the tires during the maneuver.	88
5.22	(a) Sinkage distribution for the three vehicle configurations. The value of sinkage is relative to each wheel. (b) Vertical load distribution during the maneuver. When steady state conditions are reached the load transfer phenomena still persist because the tires are still producing longitudinal forces that influence the pitch angle of the vehicle.	89
5.23	(a) Sinkage distribution for the three vehicle configurations. The value of sinkage is relative to each wheel. (b) Vertical load distribution during the maneuver. When steady state conditions are reached the load transfer phenomena still persist because the tires are still producing longitudinal forces that influence the pitch angle of the vehicle.	89
5.24	(a) Tire angular velocity and (b) instantaneous power requirement to move at 50 km/h on moist loam.	90
5.25	Power vs torque distribution for a vehicle traveling at 50 km/h on flat loam. 0 % (100 %) on the x -axis means that the torque is fully biased on the front (rear) axle of the vehicle.	90

5.26	(a) Longitudinal velocity for three vehicles traveling at 50 km/h on a 10% inclined moist loam terrain. The rear wheel drive configuration does not allow to reach comfortably the desired target speed. (b) Power requirement for the same maneuver; the RWD saturates because the imposed slip ratio limit is achieved during the simulation. The FWD vehicle is able to climb the hill but it is less efficient than the AWD one.	91
5.27	Torque distribution influence on the performance of an AWD vehicle driving at 50 km/h on a 10% inclined loam terrain. The best efficiency is reached when 60% of the total torque is delivered to the rear axle.	92
5.28	(a) Sinkage of a vehicle with decreased tire pressure traveling at 50 km/h on moist loam. (b) Slip under the same conditions.	92
5.29	(a) Longitudinal tire forces for a vehicle with decreased tire pressure traveling at 50 km/h on moist loam. (b) Power requirement for the same maneuver.	93
5.30	Torque distribution influence on the performance of an AWD vehicle driving at 50 km/h on a flat loamy terrain with reduced tire inflation pressure. The best efficiency is reached when 60% of the total torque is delivered to the rear axle.	93
5.31	Steering action during the lateral dynamic test. The steering angles δ comply with the Ackermann steering geometry introduced in (5.4). For a right turn the outer wheel is the left one and consequently $\delta_0 = \delta_l$ and $\delta_i = \delta_r$	94
5.32	(a) Roll angle of FWD, RWD, and AWD vehicles during a right turn maneuver on dry sand. (b) The load is transferred to the outer wheels (the left ones).	94
5.33	(a) Sinkage of FWD, RWD, and AWD vehicle during a right turn maneuver on dry sand. The outer wheels (left ones), being more loaded, sink more. (b) The instantaneous power requirement to complete the maneuver.	95
5.34	(a) Roll angle of FWD, RWD, and AWD vehicles during a right turn maneuver on moist Yolo loam. (b) The load is transferred to the outer wheels (the left ones).	95
5.35	(a) Sinkage of FWD, RWD, and AWD vehicle during a right turn maneuver on moist Yolo loam. The outer wheels (left ones), being more loaded, sink more. (b) The instantaneous power requirement to complete the maneuver.	96

List of Tables

3.1	Undisturbed soil properties adopted in the simulations.	43
3.2	Nominal tire properties adopted in the simulations.	43
5.1	Vehicle specifications.	75

Chapter 1

Introduction

1.1 Preface

Energy is a concept that can be elegantly understood through the first law of thermodynamics:

$$dU = \delta Q - \delta W \tag{1.1}$$

This simple equation states an extremely important concept of classical physics: work W and heat Q are two aspects of the same concept, the *energy*. The energy radiating from the sun makes life on earth possible; it remained the only source of energy until hominids became capable of controlling the fire. This became an essential tool for human beings and, in combination with devices able to harvest energy from water flows or wind (i.e. mills and sailboats), represented the main source of energy until the 18th century (without considering the muscular work of slaves, draft and pack animals).

The revolution occurred after the invention of the steam-engine: a machine able to produce mechanical work from the the combustion of coal. In history books it has gained the appellative of industrial revolution, but it would deserve the name of *energetic* revolution. The introduction of the steam-engine boosted the development of steam-powered ships, railways, and later in the 19th century of the internal combustion engine and electri-

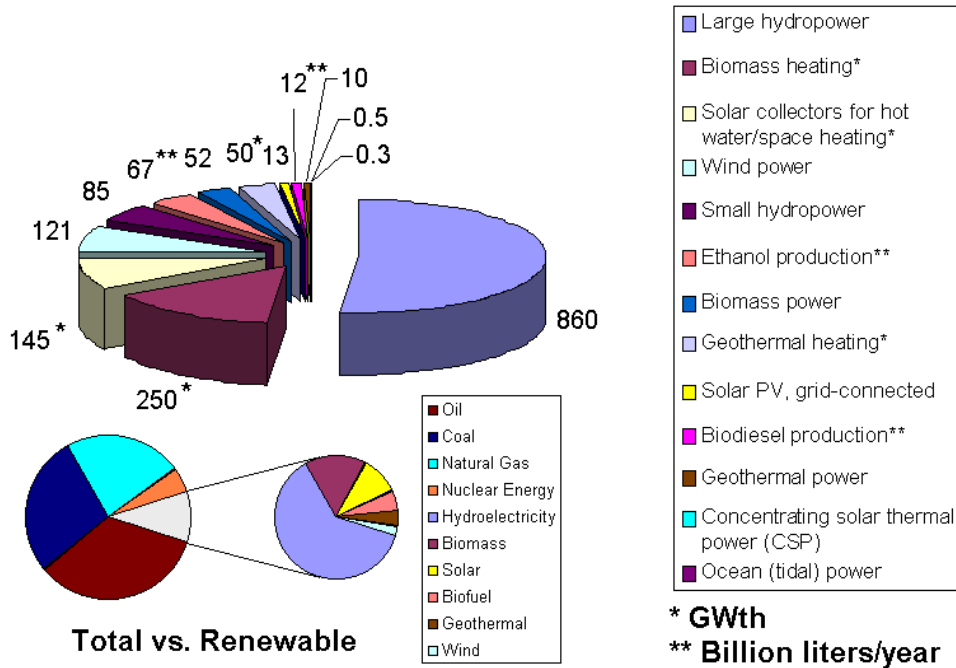


Figure 1.1: Renewable energy sources worldwide at the end of 2008 [1].

cal power generation systems. Since then the main source of energy fossil fuels. The only competitive alternative appeared with the introduction of nuclear power generation. This technology was undermined by some accidents (Three Mile Island, Chernobyl, Tokaimura the most (in)famous) that understandably turned public opinion against atomic energy. The higher cost (financial and political) due to higher safety requirements and the problem of radioactive waste disposal still remain an issue and, together with the scarcity of uranium, will probably continue to determine the fate of this technology.

Although strenuous efforts to move to alternative/renewable sources have been made, at the end of 2008 more than 80% of world electric energy was produced from fossil fuels (see Fig. 1.1). These resources are constantly depleting without regeneration and even if it is true that the oil shortages are often a result of market's laws (drilling capacity is decided by the countries/companies) there is no doubt that one day the oil will end. The first energy crisis struck in the 70's and highlighted how much our society is energy-dependent.

Figure 1.1 shows that it would be naive to think that a single technology could be the panacea for the energy crisis. A very specialized and targeted effort in several fields is necessary, in order to harvest energy in the most efficient way from many different sources.

The problem of energy production and transformation is directly linked to another challenge that our generation has to face: global warming [9]. Increasing the efficiency is not only a way to reduce energy consumption but also emissions.

The problem is not limited to energy production but it directly extends to the energy consumption. Highly efficient devices help to reduce the energy requirement or, from another perspective, guarantee the same standards to a larger number of persons, while exploiting the same resources. For this reason during the last decade the concept of energy efficiency has become a *leitmotif* in several fields, and it has directly influenced our everyday life. The introduction of the Toyota Prius [10], the first full hybrid electric mid-size car, has marked an era and opened new frontiers for more efficient vehicles. It is symptomatic that in many fields a general shift from pure performance to increased efficiency is occurring. For example computer components (processors, video cards, hard disks etc) are now marketed and reviewed not only by performance but also by their consumption. Even the motor-sport competition world is moving in the same direction: FIM (Fédération Internationale de Motocyclisme) regulations [11] now require reduced fuel tank size for Moto-GP competitions (in order to push manufacturers to increase fuel economy) while the FIA [12] (Fédération Internationale de l'Automobile) introduced the KERS (Kinetic Energy Recovery Systems) for the 2009 Formula 1 season. Ferrari (Ferrari 599 HY-Kers [13]) and Porsche (Porsche Intelligent Performance [14]), two brands historically synonymous with pure performance, have revealed projects for high performance hybrid cars: a shock for some purists, yet a courageous commitment by the companies. The aforementioned only represent a handful of examples among many.

It is clear that in an energy-dependent society, energy efficiency is a critical component of machinery design and plays a central role when resources are scarce. The results obtained in this dissertation are not limited to devices operated using fossil fuels: they regard a general class of vehicles or particular sub-systems that can find applications regardless of the main source of vehicle power.

1.2 Problem Statement

The following discussion will start from on-road vehicles and successively move to off-road vehicles. The automotive sector started to consciously think about the fuel economy only in the 70's, when the first energy crisis occurred. That event encouraged researchers and companies [15] to spend great effort in order to optimize the energy consumption of vehicles.

Regarding fuel economy, the power-train is the first component that comes to mind, but there are two other factors that have great impact on the overall energetic performance: the aerodynamic drag and the rolling resistance.

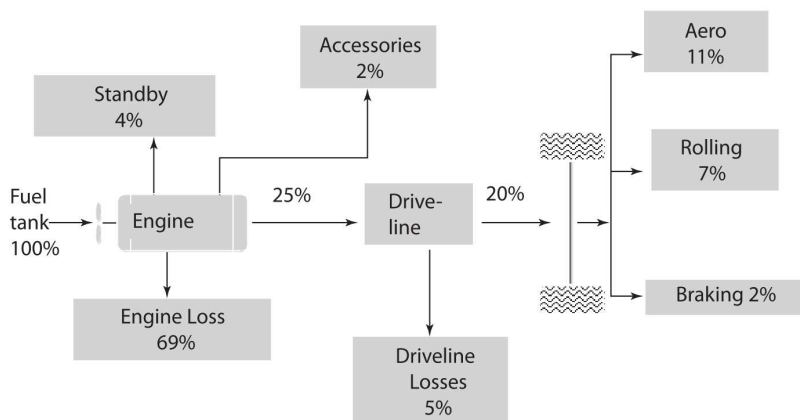


Figure 1.2: Energy flow in a typical mid-size car traveling on flat, hard surface. (Reprinted from [2] , obtained from Transportation Research Board Special Report 286 under the FOIA.)

After the impulse given by the 1973's crisis faded, the average miles per gallon (or MPG) of the American car fleet almost flattened and new interest in the topic arose again only in 2005, when the oil reached unprecedented price record. The performance of internal combustion engines remains bounded by the physical limit imposed by the 2^{nd} law of thermodynamics and modern engines already approach this limit of 20-35% efficiency (in this case defined as energy stored in the fuel divided by the mechanical energy delivered by the engine). From this point of view the 4-7% of energy absorbed in rolling resistance and the 3-11% in aerodynamic drag represent a consistent share of the output available from the engine (see Fig. 1.2). As a consequence tire dynamics still plays a crucial role in energy consumption analysis. In response to increasing oil prices, the European market is witnessing a shift toward smaller engine cars: the idea is to reduce the weight of the vehicle

introducing smaller and more efficient engines. This process, commonly called downsizing, is necessary in order to exploit resources in a better way and it is slowly finding its way also in the American market. Dr. Lino Guzzella (a professor at the ETH Zurich and an expert of modeling and control of internal combustion engine systems) during a plenary lecture at the 2008 American Control Conference held in Seattle [16], highlighted that better fuel economy will be achieved through the following strategies:

- decrease car weight through the reduction of passive and active safety devices that will become less important when cars will share informations between each other (presence of obstacles ahead, traffic information, threat forecasting),
- adoption of smaller and more efficient engines (possible for lighter vehicles).

The energy efficiency of off-road vehicles has not been extensively studied in recent years. Main contributors to the field are Bekker and Wong which laid the foundation for the off road mobility studies [17, 18]. In the off-road context the energy flow showed in Figure 1.2 is still valid but the rolling resistance assumes a predominant role. Mobility is highly dependent on soil properties, factors like the sinkage and the slippage deeply affect the capability of a vehicle to move. In military applications, off-road operations are common and the possibility of saving fuel has a strategic and tactical relevance. Vehicle operation on unpaved surfaces is common also in agriculture, construction, exploration, recreation, and mining machinery. These applications would benefit from a better understanding of parameters that affect the fuel consumption.

1.3 Research Objectives

The scope of this research is to establish a tool for predicting mobility, handling and tractive efficiency of off-road vehicles. The study of off-road vehicles has originally focused on the mobility aspect, having as a primary objective the capability to ascertain if a vehicle was able to move on a certain terrain. The performance of land vehicles are intrinsically influenced by tire behavior. The present work focuses on the development of a tire model able to describe not only the mobility but also the salient features encountered in off-road operations (i.e.

slip-sinkage, bulldozing, multi-pass, parameter sensitivity). The sinkage represents the main source of rolling resistance during off-road operations while the repetitive passage over the same patch of terrain can significantly modify the response of the tires. A tire model able to predict these aspects allows one to comprehensively study the performance of an off-road vehicle. For this reason the tire model developed is then implemented into a full-vehicle model in order to simulate the tractive efficiency of a full vehicle during standard maneuvering.

The objectives can be summarized as follows:

1. Development of a semi-empirical tire model able to predict: longitudinal force, torque, lateral force, slip-sinkage effect, multi-pass behavior and bulldozing phenomenon. The tire model is based on empirical expressions and theoretical assumptions in order to realistically estimate the parameters influence.
2. Investigate the influence of tire parameters on the tractive efficiency. Verify the capability of the developed tire model to correctly predict the tractive efficiency of tires during off-road operations.
3. Combine the information obtained above to simulate the performance of a vehicle transversing unprepared terrain. The tractive efficiency of the vehicle is analyzed and general directions for torque distribution strategies are provided. Standard maneuvers are simulated in order to characterize the handling of the vehicle.

These aims will be achieved under the assumptions that:

1. The tire properties remain constant during the simulation. No heating and wearing phenomenon are considered.
2. The terrain is homogeneous.
3. The full-vehicle model satisfies simplifying assumptions that will be discussed in more detail in Chapter 5.

1.4 Research Contribution

This research describes and implements a detailed semi-empirical tire model for off-road vehicle simulations. An accurate tire model is necessary for the analysis of mobility, handling and tractive efficiency during off-road operations. The principal contributions of this study can be summarized as follows:

- Improved existing semi-empirical off-road tire model for faster, but still accurate, vehicle dynamics simulations. The tire model accounts for complex behaviors such as the multi-pass effect and the slip-sinkage phenomenon.
- Simulation of a full vehicle while adopting a detailed off-road tire model.
- Analysis of the torque distribution strategy that can help in minimizing the energy consumption.

1.5 Dissertation Outline

The dissertation is outlined proceed as follows.

Chapter 2 will present a review of literature introducing the basic concepts of tire mechanics. A brief overview of tire history will be given and the terramechanics approach to tire-terrain problems will be illustrated. The chapter is concluded by a discussion of a full off-road vehicle simulation.

Chapter 3 introduces the tire model. The development of the model is explained and the method is discussed in detail. Results for longitudinal, lateral, and combined slip operations are presented.

Chapter 4 discusses the economy of land vehicles. A brief review of internal combustion engines and electric motor efficiency is given. Thereafter the basic concepts related to the aerodynamic drag are presented, and finally the tractive efficiency of tires operating in off-road conditions is discussed.

Chapter 5 introduces the full vehicle model. The model is illustrated and basic back-

ground of vehicle dynamics is provided. The chapter shows the simulation results of vehicles running on flat terrain, sloped terrain, sand, and loam. Different drive configurations are analyzed (RWD,FWD,AWD) as well as tire parameters (size, width, inflation pressure).

Chapter 6 will present conclusive remarks, highlight the research findings and propose future work directions.

Chapter 2

Review of Literature

The dynamics of a wheeled vehicle are substantially influenced by the behavior of its tires. The tire is the device that allows the vehicle to convert the energy delivered by the engine into useful work (motion). Behind a simple description and appearance it is hidden an extremely complex engineering subsystem: its geometry, design and construction can deeply affect vehicle performance and efficiency. For this reason a realistic analysis of the dynamics of a vehicle cannot be achieved without an accurate tire model.

This chapter will present:

1. a brief introduction on tire mechanics terminology,
2. an overview of tire evolution,
3. the main contributions to tire models development for off-road applications,
4. a discussion of full off-road vehicle models for dynamics simulations, and
5. a brief introduction on vehicle efficiency.

2.1 Tire Mechanics Terminology

This section introduces the basic terminology commonly adopted by the vehicle dynamics community. The SAE standard [3], extensively used in the automotive industry, is adopted.

The origin of the tire axis system is located at the bottom of the tire, ideally at the center of the contact patch in contact with the soil. A Cartesian right-handed axis system is chosen with the x -axis pointing in the direction of wheel heading, the z -axis perpendicular to the road plane with a positive direction downward, and the y -axis in the road plane with its direction chosen to make the axis system orthogonal, as shown in Figure 2.1. The definition of the most relevant quantities is given below:

- The slip angle α is the angle between the x -axis and the direction of travel of the center of the contact patch. A positive slip angle corresponds to a clockwise rotation of the tire when looking from the top.
- The inclination angle γ (also camber angle) is the angle between the z -axis and the wheel plane.
- The longitudinal force F_x is the component of the tire force vector in the x -direction.
- The lateral force F_y is the component of the tire force vector in the y -direction.
- The normal or vertical force F_z is the component of the tire force vector in the z -direction.
- The overturning moment M_x is the component of the tire moment vector tending to rotate the tire about the x -axis, positive clockwise when looking in the positive direction of the x -axis.
- The rolling resistance moment M_y is the component of the tire moment vector tending to rotate the tire about the y -axis, positive clockwise when looking in the positive direction of the y -axis.
- The aligning moment (or torque) M_z is the component of the tire moment vector tending to rotate the tire about the z -axis, positive clockwise when looking in the positive direction of the z -axis.
- The wheel torque T is the external torque applied to the tire from the vehicle about the spin axis. Since the inclination angle γ will be taken equal to zero, the wheel torque will correspond to the resistance moment throughout the dissertation.

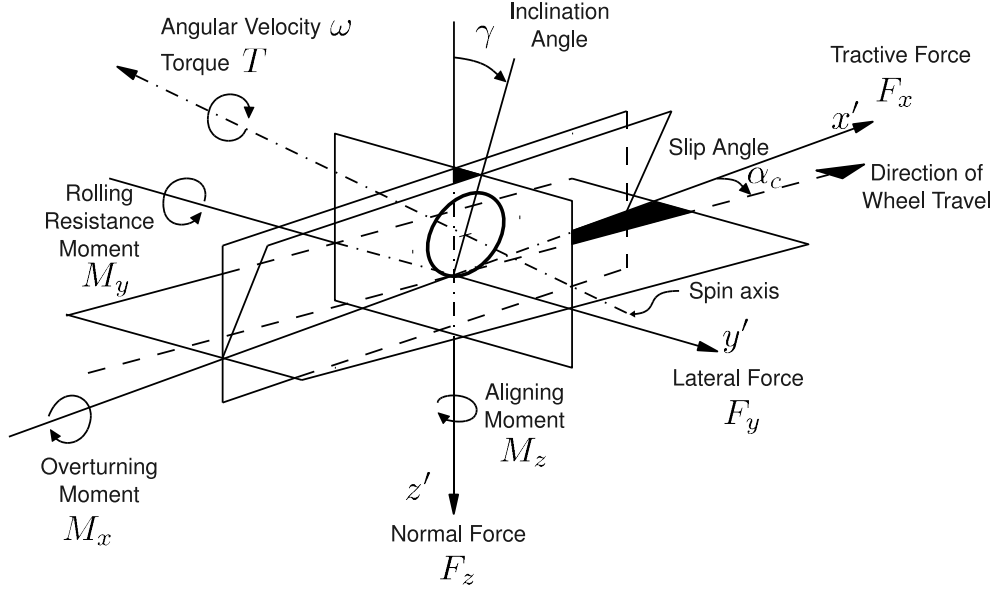


Figure 2.1: Definition of the tire axis system and most relevant quantities according to SAE J670e [3].

- The undeformed tire radius R_u is the radius of the newly unloaded tire inflated to the normal recommended pressure and mounted on the specified rim.
- The angular velocity of the wheel (or spin) ω is the angular velocity of the wheel on which the tire is mounted.
- The longitudinal slip or slip ratio s_d is a measure of the difference between the effective angular velocity ω and the longitudinal velocity of the tire (the speed of the center of the wheel in the longitudinal direction). Due to a relative slip between the tire and the road there will be a difference between the theoretical tire velocity (i.e. ωR_u for a rigid wheel) and the actual velocity of the tire in its the travel direction (denoted here as V).

$$s_d = 1 - \frac{V}{\omega R_u}. \quad (2.1)$$

Among the quantities that we have just introduced two of them deserve particular attention: the slip ratio s_d and the slip angle α . The ability of a tire to produce longitudinal (lateral) force is strictly related to its slip ratio (angle). When a vehicle accelerates, brakes or simply coasts the tires are not *simply* rolling but there is always a relative motion somewhere

in the contact patch (i.e. the slip).

2.2 Tire History and Evolution

Tire history begins after the introduction of the vulcanization process by Charles Goodyear in 1843. Vulcanized rubber made possible the construction of flexible wheels (the tire), that later became an essential component of motor vehicles. In the following years a series of design evolutions occurred and the most relevant can be summarized as follow: pneumatic removable tires (1890 circa), cord reinforced tires (1900 circa), grooved tires (1908), radial tires (1946).

The tire, as a vehicle subsystem, has multiple roles:

- It has to support the vehicle load.
- It has to *transfer* to the ground the energy delivered by the engine and provide the vehicle with steering capabilities.
- It behaves as a secondary suspension. This guarantees better performance and comfort (it should be noted here that for the primary suspension system comfort is *only* a side effect, handling being the principal reason for its introduction).

The dominant design today is the radial-ply construction. This approach was introduced originally by Michelin and quickly became the standard as it brought consistent advantages over the bias-ply design. Examples of the most common tire structures are given in Figure 2.2.

Tires are not simply a rubber structure but are made of several layers of different materials. In order to guarantee the desired strength, layers of polyester, steel and/or other textile materials are joint together into a complicated structure. The bias-ply or cross design was the first design introduced but it has now almost disappeared from the market in favor of the radial design. The radial design provides a wider footprint on the ground, better ground pressure distribution, and reduced friction [19]. These results are obtained thanks to the different orientation of the plies and the introduction of reinforcing steel belts: such

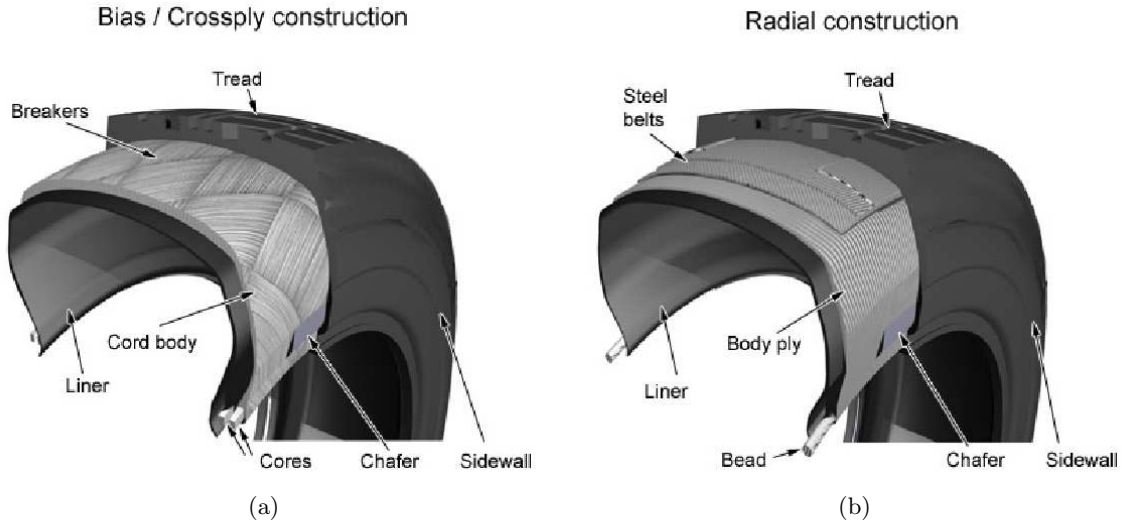


Figure 2.2: Construction layout of a bias-ply (a) and a radial-ply (b) tire. Adapted from [4]

modifications allow the sidewall and tread to deform independently and avoid the heat generation produced by the friction of the crossed plies. These enhanced properties allow the radial design to attain better tire life, improved handling and fuel economy. This study will not consider the differences between bias-ply and radial-ply design because during off-road operations, the principal resistance force is not tire hysteresis but the terrain compaction. Under this assumption the tire construction technique does not play a major role.

2.3 Terramechanics Approach to Tire-Terrain Modeling

The reference book for on-road tire modeling is the work by Pacejka [19]. However, the development of tire models for off-road applications follows distinct methodologies that will be presented in this section. In some cases, Pacejka's and similar on-road models have been modified to account for off-road testing by reducing the coefficient of friction in order to simulate the lack of traction on rough terrain. This represents a very first approximation since it disregards effects such the sinkage, the multi-pass, the bulldozing effects etc.

The tire model presented in this dissertation follows the approach proposed by the terramechanics community. Terramechanics is the engineering field that studies the soil properties and the interaction between wheeled or tracked vehicles and deformable terrain.

The *father* of this discipline is considered M. G. Bekker, author of *Theory of land locomotion* [17], published in 1950 and become a *classic* in the terramechanics community. After the Second World War the proliferation of automobiles has pushed the automotive industry to focus on on-road locomotion problems but the study of vehicles moving on unprepared terrain remained a subject of interest for the Army, for planetary exploration agencies, agricultural field, construction, recreation, and mining industries.

Amongst the terramechanics community four primary approaches can be summarized:

- empirical methods,
- semi-empirical methods,
- analytical methods,
- finite element methods.

The main features of the aforementioned methodologies will be presented in the following sections.

2.3.1 Empirical Methods

The first methods introduced to study the mobility of vehicles over unprepared terrain are mainly empirical. The most common one was introduced by M. G. Bekker [17, 20, 21], while working for the Land Locomotion Laboratory in the U.S. Army Detroit Arsenal in the 50's. The key contribution of Dr. Bekker is the introduction of a semi-empirical equation that relates the sinkage with the normal pressure of a plate pushed down into the soil. The proposed relation is commonly referred as Bekker equation,

$$\sigma_n = \left(\frac{k_c}{b} + k_\phi \right) z^n, \quad (2.2)$$

where:

σ_n = pressure normal acting on the sinkage plate,

k_c = cohesion-dependent parameter,

k_ϕ = friction angle dependent parameter,

n = sinkage index,

b = plate width,

z = sinkage.

The parameters introduced in (2.2) are obtained from field tests conducted with a bevameter. The bevameter is a device that records the sinking and the normal pressure exerted on a plate of width b while it is pressed into the terrain at constant displacement rate. Bekker proposed also a relation to characterize the shear strength of the soil,

$$\tau = \frac{K_3}{2K_1\sqrt{K_2^2-1}} \left(e^{(-K_2+\sqrt{K_2^2-1})K_1z} - e^{(-K_2-\sqrt{K_2^2-1})K_1z} \right), \quad (2.3)$$

where K_1 , K_2 , and K_3 are constants obtained through experiment similar to the one described above. It should be mentioned that in the method proposed by Bekker there is no coupling between the shear displacement and the normal stress. For this reason Janosi and Hanamoto [22] introduced an alternative formulation that has gained great popularity in the terramechanics community. They assumed that the shear stress, tangential to the surface of the sinkage plate, can be predicted through a combination of the Mohr-Coulomb Failure Criterion and the normal stress distribution,

$$\tau = (c + \sigma_n \tan(\phi)) \left(1 - e^{-\frac{j}{k}} \right), \quad (2.4)$$

where:

$c + \sigma_n \tan(\phi)$ = is the Mohr-Coulomb failure criterion,

c = soil cohesion,

j = soil-plate interface shear displacement,

k = shear deformation modulus in the direction of motion,

ϕ = internal angle of friction.

However, this formulation is still empirical, it introduces a strong causative physical connection between the kinematics (the shear displacement) and the stresses (the Mohr-Coulomb criterion) which is completely absent in the Bekker shear equation (2.3). Several researches used the approach proposed by Janosi and Hanamoto with good results: especially on sand, saturated clay, fresh snow and peat [23].

A development of Bekker (2.2) was proposed by Reece, with the intent of giving more physics insight to the pressure sinkage dependency. Reece suggested an equation that separately accounts for the cohesion of the soil and the soil weight,

$$\sigma_n = (ck'_c + b\gamma_s k'_\phi) \left(\frac{z}{b}\right)^n, \quad (2.5)$$

where:

σ_n = pressure normal to the sinkage plate,

k'_c = cohesion-dependent parameter,

k'_ϕ = friction angle dependent parameter,

n = sinkage index,

b = plate width,

γ = unit weight of the soil,

c = soil cohesion.

15

The Reece equation (2.5) is extremely similar to Bekker's (2.2) but it has the advantage to adopt purely dimensionless constants (k'_c and k'_ϕ) and normalized sinkage ($\frac{z}{b}$).

The Bekker/Reece equations (2.2),(2.5) and Janosi-Hanamoto equation (2.4) represent the foundation of empirical and semi-empirical models. They have been extensively used by several researchers to model locomotion problems, and even with some limitations, they proved to be valid modeling tools.

Researchers at the Waterways Experimentation Station (WES) [24] developed a popular empirical method for determining the mobility of both wheeled and tracked vehicles. The method assesses the mobility on a "go/no go" basis. A cone penetrometer is used to measure the strength of the soil and obtain a cone index. The cone index is compared with a mobility index obtained from the vehicle characteristics such as the vehicle weight, the contact area, the size of grouser, the engine power, and the type of transmission. If the mobility index exceeds the cone index the motion is possible; otherwise the vehicle is stuck. A similar approach was proposed by Brixius [25] for agricultural vehicle mobility prediction. These methods are purely empirical, they solely provide information regarding the mobility of the vehicle; a detailed analysis of the tire-terrain interaction is not conducted.

2.3.2 Semi-Empirical Methods

The tire model adopted and expanded in this study, follows the semi-empirical model proposed by Chan and Sandu [26, 27, 28, 29]. This section presents an overview: a detailed description will be provided in Chapter 3 where the tire model will be explained step by step.

Bekker developed the first semi-empirical method based on (2.2),(2.3). This method [21] provides estimate for the sinkage, drawbar pull, resistance force, and other significant variables through empirical formulas related to the properties of the terrain. A significant step forward was the model proposed by Wong and Reece [6, 30]. In their formulation the the normal stress and the shear stress along the wheel were calculated starting from (2.2),(2.4). The stresses were integrated along the contact patch in order to calculate the forces acting on the wheel. More details regarding this method will be given in Chapter 3. It should be mentioned that this approach has been implemented by many researchers and demonstrated to provide reasonable results especially for non cohesive soils, for example, the dry sand. Wong and Reece did not investigate lateral dynamics. Amongst the best and most comprehensive studies in this field there is the one by Schwanghart [31]. The author calculated the lateral force considering two contribution: the lateral shear at the contact patch (based on (2.4)) and the bulldozing effect (based on the work by Hettiaratchi-Reece [32] and Terzaghi [33]).

Grečenko's [34, 35] slip and drift model (SDM) was the first model that included both the longitudinal (slip) and lateral (drift) dynamics. The SDM model follows a completely different approach compared to Wong and Schwanghart and will be briefly introduced. Grečenko defined the deformation gradient as follows,

$$u = \frac{j}{x} = f\left(\frac{F_u}{F_z}\right), \quad (2.6)$$

where:

u = deformation gradient,

j = shear deformation,

x = coordinate along the contact patch,

F_u = total shear force,

F_z = total normal force.

A constraint equation that relates the lateral and longitudinal forces is stipulated,

$$(1 - s_d)F_x \tan(\alpha) - F_y s_d = 0. \quad (2.7)$$

Grečenko then calculates:

- the coefficient of friction as a function of the gradient of deformation $\mu = f(u)$
- the maximum shear stress as a function of the shear deformation $\tau_{max} = f(j)$

The longitudinal and lateral forces are finally linked to the total shear force through the following expression,

$$F_u = (F_x^2 + F_y^2)^{1/2} = \tau_m b \int_0^1 f(ux) dx. \quad (2.8)$$

None of the aforementioned studies included the multi-pass effect. When a tire rolls (being either driven, braked, or towed) on a patch of terrain it compacts the soil and creates

a rut. Soil properties in the rut region are different from the properties of undeformed terrain. The repetitive loading of terrain has been studied by Bekker [21] and Wong [23, 18]; both authors highlighted that during the unloading process the pressure-sinkage relation follows a constant slope line. This finding was exploited by Harnisch et al. [5] to develop an off-road tire model capable of simulating the multi-pass effect. The Harnisch et al. model follows an approach similar to Wong and will be discussed in more detail in Chapter 3.

Holm [7] collected extremely valuable experimental data regarding the multi-pass effect of tires. The author did not propose a theory to explain the results, but he provided experimental evidence that supports the approach proposed in this work: the soil density and cohesion increases after each pass (similar conclusions are presented in Bekker’s work [21]).

Among the most advanced off-road tire models for real-time vehicle simulation is the System Technologies Inc. (STI) tire model. It was developed in 1997 for on-road applications and was later extended to account for off-road operations [36]. The model is based on Wong and Bekker studies and it seems to account only for rigid tire operating mode.

2.3.3 Analytical Methods

Analytical methods follow a different approach from empirical and semi-empirical models. They are not based on (2.2): the stress state under the contact patch is reconstructed solving the differential equations that govern the soil state under the wheel. The benchmark study in the field remains the one performed by Karafiath and Nowatzki [37]. The authors calculated the stress state at the tire contact patch by computing the forward and backward slip line fields of the soil. Adopting plasticity theory they characterized the soil under the wheel as follows,

$$(1 + \sin(\phi) \cos(2\theta)) \frac{\partial \sigma}{\partial x} + \sin(\phi) \sin(2\theta) \frac{\partial \sigma}{\partial z} - 2\sigma \sin(\phi) \left(\sin(2\theta) \frac{\partial \theta}{\partial x} - \cos(2\theta) \frac{\partial \theta}{\partial z} \right) = \gamma \sin(\epsilon), \quad (2.9)$$

$$\sin(\phi) \sin(2\theta) \frac{\partial \sigma}{\partial x} + (1 - \sin(\phi) \cos(2\theta)) \frac{\partial \sigma}{\partial z} + 2\sigma \sin(\phi) \left(\cos(2\theta) \frac{\partial \theta}{\partial x} + \sin(2\theta) \frac{\partial \theta}{\partial z} \right) = \gamma \cos(\epsilon), \quad (2.10)$$

where:

ϵ = angle of inclination of the x -axis from the horizontal,

θ = angle between the horizontal and the direction of the major principal stress,

ϕ = angle of internal friction.

These equations are valid for the plane strain condition and assume the Mohr-Coulomb failure criteria to hold. Equations (2.9) and (2.10) elegantly describe the state of stress of the soil beneath the tire but their solution relies on the definition of the proper boundary conditions. The position of the slip line fields are defined by three *central* angles (illustrated in Figure 2.3.3) :

θ_e = the entry angle,

θ_b = the exit angle,

θ_m = angle of separation (angle at which the slip lines fields meet).

These angles are not known a priori. Only two conditions can be derived to characterize them:

- Equilibrium of vertical forces requires that the vertical component of the stresses integrated along the contact patch must equal the vertical load acting on the tire.
- Continuity requires that the normal and shear stress at the angle of separation θ_m must match.

One of the angles introduced above have necessarily to be assumed because only two conditions are available and three variables need to be calculated. A similar problem also arises with semi-empirical models where the stress state is solved through (2.2),(2.4) instead

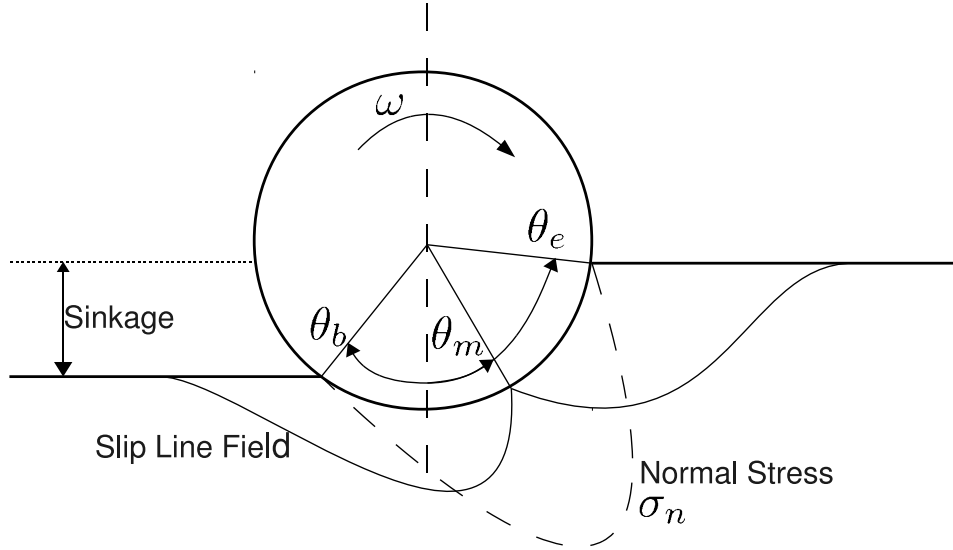


Figure 2.3: Descriptive plot of a wheel rolling into soft terrain.

of (2.9),(2.10) but the entry, exit, and separation angles need to be calculated in some way. More details will be given in the tire development chapter, Chapter 3. The Karafiath and Nowatzki method has a strong theoretical background but is computationally expensive and not suitable for vehicle dynamics simulation.

2.3.4 Finite Element Methods

The increase of computing power over the last three decades boosted the introduction of finite element methods (FEM) for the solution of continuum mechanics problems. The application of finite element codes to tire mechanics problems allows the researcher to study the behavior of tires in detail; full three-dimensional analysis including heating and vibrational effects of the carcass are possible. The vast majority of the literature available regards on-road tire models but there are also good studies in the area of terramechanics.

Shoop et al. [38, 39] have successfully adopted FEM codes to simulate tires rolling on deformable terrain and snow (see also [40]). Nakashima et Oida [41] combined finite element analysis (FEA) and discrete element analysis (DEA) to model the tire-soil behavior. Adopting a diversified approach, the tire is considered as a continuum (FEA) and the terrain as an agglomerate of discrete particles (DEA). Similar approaches have been followed by many researchers [42, 43, 44]: this methodology is attractive because it produces an extremely

realistic kinematic simulation of the soil particles (especially for non cohesive soils).

The principal limitation associated with FEM analysis is the long computational time, and the need to provide accurate boundary conditions. Finite element methods provide extremely detailed information that would certainly help the tire design, but they are at the moment not suitable for real-time vehicle simulation.

2.4 Off-Road Vehicle Dynamics

Vehicle dynamics is a well documented subject and extensively analyzed in the literature. The simulation of an off-road vehicle differs from the on-road counterpart mainly for the tire-terrain model. Books by Genta [8] and Gillespie [45] represent a good source of information for understanding the principles of vehicle dynamics and the best approaches to modeling. To a good, first approximation, the vehicle can be modeled as a rigid body having six degrees of freedom that can be described by the coordinates illustrated in Figure 2.4:

- u = longitudinal velocity. The component of velocity in the x -direction of the vehicle-fixed reference frame.
- v = side or lateral velocity. The component of velocity in the y -direction of the vehicle-fixed reference frame.
- w = normal or vertical velocity. The component of velocity in the z -direction of the vehicle-fixed reference frame.
- p = roll velocity. The component of angular velocity in the x -direction of the vehicle-fixed reference frame.
- q = pitch velocity. The component of angular velocity in the y -direction of the vehicle-fixed reference frame.
- r = yaw velocity. The component of angular velocity in the z -direction of the vehicle-fixed reference frame.

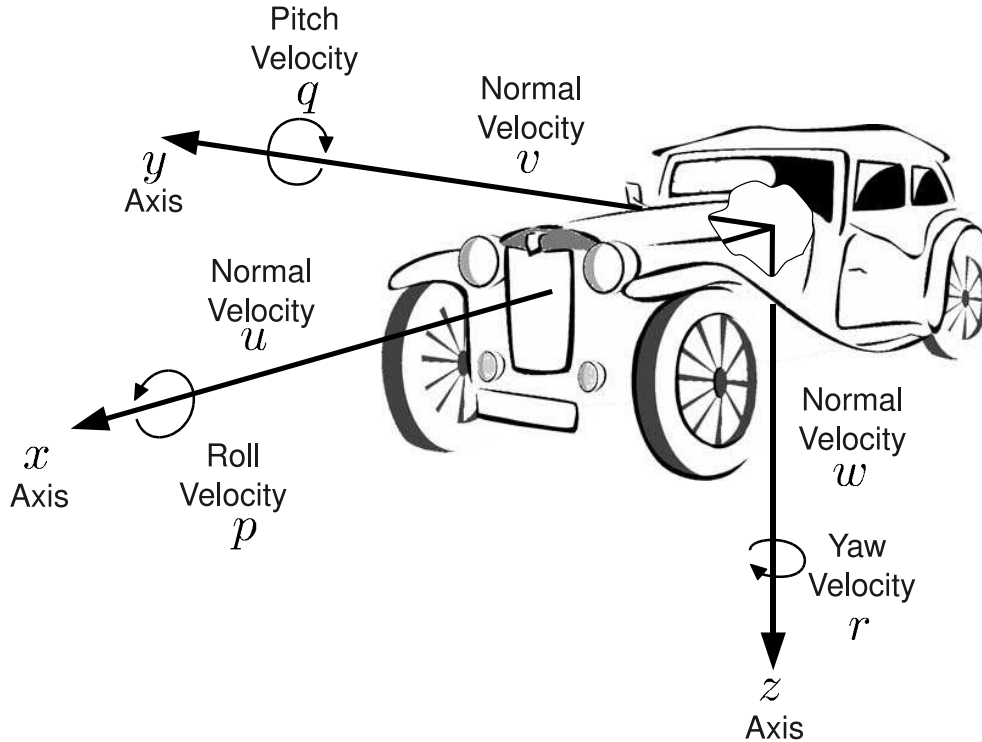


Figure 2.4: Definition of the vehicle axis system according to SAE J670e [3].

This thesis follows a well-established approach to study the dynamics of the vehicle that will be discussed later in Chapter 5. It should be mentioned that due to the lack of off-road tire models for real-time vehicle simulations there is not a rich literature in the field.

Letherwood and Gunter [46] modeled a heavy vehicle adopting a simplified tire model and “after an extensive set of parameter and design studies, it was determined that better correlation between the simulation results and the field and laboratory test results could not be achieved partly because of errors introduced into the model results by the use of simplified tire and steering models”.

Cranfield University at Silsoe started a program dedicated to off-road vehicle testing but for the moment only direct testing has been performed [47].

Studies have been conducted in the field of unmanned vehicles (DARPA Grand Challenge, but also other projects sponsored by the same agency) where the University of Stanford has taken the lead [48, 49]. In this case, the tires have been modeled in a simplified way, starting from an on-road model. It should be mentioned that the off-road sections of

the DARPA challenge were not extremely severe, and a simplified tire model still provided acceptable results.

A vehicle model that incorporates a full scale off-road tire model has been proposed by Sharaf et al. [50]. The authors adopted Harnisch et al. AS2TM tire model [5] and performed standard handling maneuvers. The results were not validated against experiments but yield to realistic prediction of the quantities of interest.

2.5 Tractive Efficiency

The efficiency of land vehicles (on and off-road) depends on three main factors:

- Power-train: thermodynamics losses in the engine and frictional losses in the engine and drive-train.
- Aerodynamics: frictional and shape losses due to the the viscous effects of the air flowing around the vehicle.
- Tire rolling resistance: resistance force that develops at the tire-terrain interface. For on-road applications it is mainly due to the hysteresis of the tire, for off-road to the terrain compaction (the hysteresis phenomenon is still present but on a reduced scale).

This study sets aside the first two aspects and focuses on the impact of the rolling resistance (more details will follow in Chapter 4). A well documented parameter to study the tractive efficiency is the following,

$$\eta_t = \frac{F_x v_x}{T\omega}. \quad (2.11)$$

The tractive efficiency η_t measures the ratio between driving power $T\omega$ applied to the wheels and the tractive power $F_x v_x$ effectively generated. Under ideal assumptions the entire torque transmitted to the wheels would be transformed into forward velocity (pure rolling without slipping). In reality, slip phenomena and terrain compaction limit the net traction and reduce the tractive efficiency. An exhaustive discussion on tractive efficiency is given

by Zoz and Grisso [51]. Their analysis focuses on agricultural tires but it can be extended, without loss of generality, to off-road vehicles in general. Adopting the Brixius approach [25] they discuss the performance and efficiency of agricultural tractors. The outcomes are:

- Peak of tractive efficiency is reached in the 10-20% slip range.
- Larger tires provide better efficiency.
- Lower inflation pressure increases the tractive efficiency.
- Increased axle load has contrasting effects.

A tire model for vehicle simulation has to correctly predict the aforementioned results in order to provide realistic estimates of the energy consumption. Chapter 4 will show the results obtained with the proposed tire model and will present a general discussion on the efficiency of off-road vehicles.

Another parameter that influences the mobility (and the efficiency) is the torque distribution among the axles. In order to improve traction, off-road vehicles usually adopt all wheel drive schemes (AWD or 4WD). An excellent review of strategies and the philosophies behind various traction schemes is given by Mohan [52]. Figure 2.5 presents the typical torque path into an off-road vehicle. The axle differentials splits the torque evenly between the left and right wheels while the central differential can be tuned to distribute the torque unevenly between the axles.

Sharaf et al. [53] simulated a full vehicle adopting the AS2TM tire model developed by Harnisch et al. [5] and concluded that “in order to achieve the maximum tractive efficiency, the driving torque should be distributed to match the weight distribution between the front and rear axles in a manner as to minimize the slip difference between them”.

Yamakawa et al. [54] studied independent wheel drive vehicles and highlighted in their conclusions that “torque allocation based on the vertical load on the individual wheels is one possible method for efficiently controlling wheel torque for vehicles with independently driven wheels”.

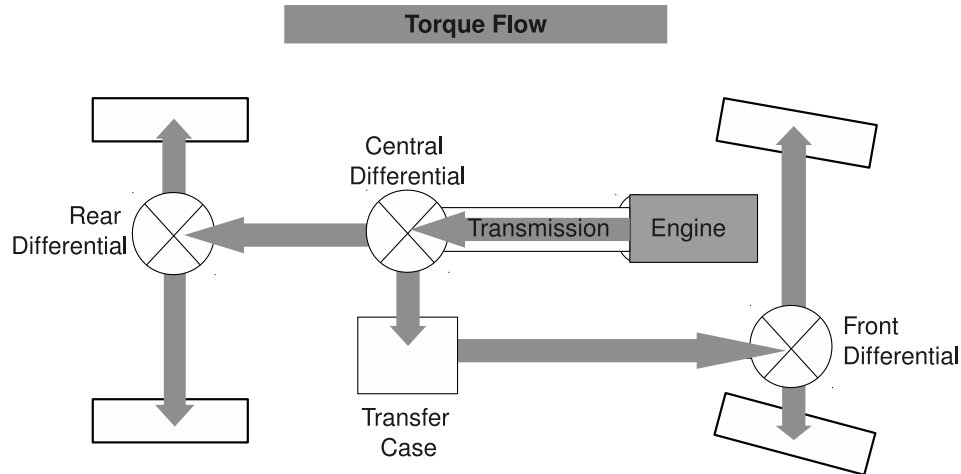


Figure 2.5: Torque *flow* in a four wheel drive vehicle. The torque produced by the engine is split by the central differential and reaches the axles. At the axles is split again by the axle differentials delivered to the wheels. Arrows' length is not proportional to torque magnitude; the axle differentials always split the torque equally between the axles.

Chapter 5 will analyze the torque distribution adopting the tire model proposed in this study and will present an extensive analysis on the tractive efficiency of off-road vehicles.

2.6 Review of Literature Summary

This chapter provided an overview of the previous studies on tire-terrain interaction and discussed the most advanced methodologies to analyze the tractive efficiency of off-road vehicles. The research presented in this thesis attempts to overcome some limitations introduced by the Chan and Sandu tire model [26, 27, 28] and implements the model into a full vehicle in order to predict both the mobility and the efficiency. Most of the previous studies on tire-soil interaction primarily dealt with mobility and focused on tractive capabilities rather than tractive efficiency. The studies that analyzed the tractive efficiency adopted pure empirical models (Zoz and Grisso [51]), simplified models (Yamakawa et al. [54]) or focused on different aspects (Sharaf et al. studied visco-lock differentials [53]).

Chapters 3, 4, and 5 will present in detail the development of the tire model, the discussion on the tractive efficiency, and the study of mobility and efficiency of a full-vehicle during off-road operation.

Chapter 3

Tire Model Development

The model presented in this chapter is valid for both rigid wheels and flexible tires. The rigid wheel implementation is based on the model developed by Wong and Reece [6, 30] while the flexible tire implementation follows the approach proposed by Chan and Sandu [26, 27, 28]. The original formulations have been modified in several aspects in order to improve the model capabilities. These aspects will be clarified in the following sections where the model peculiarities will be explained. The rigid wheel can be considered a first approximation of a flexible tire. When the terrain stiffness is significantly lower than the total tire stiffness (the carcass stiffness plus the inflation pressure), the flexible tire can be approximated as a rigid wheel, greatly simplifying the analysis. The study of rigid wheels is relevant as some vehicles are natively equipped with rigid wheels. This is the case of robots for extraterrestrial exploration [55, 56, 57] where rubber compounds cannot be used because of the severe environmental conditions (extreme temperature gradients and, possibly, unfavorable atmospheric chemical composition).

3.1 Pressure-Sinkage Equation

The first step for a semi-empirical method is to estimate the stress distribution along the contact patch. Normal and shear stresses develop at the interface between a rotating tire and the soil surface. The normal stress is calculated from the pressure-sinkage equation

originally introduced by Bekker [17] and later modified by Reece (3.1),

$$\sigma_n = (ck'_c + b\gamma_s k'_\phi) \left(\frac{z}{b}\right)^n, \quad (3.1)$$

where:

σ_n = pressure normal to the sinkage plate,

z = sinkage,

n = sinkage index,

c = soil cohesion,

γ = soil density,

k'_c = cohesion dependent soil coefficient,

k'_ϕ = frictional dependent soil coefficient,

b = parameter related to the geometry of the penetrometer (the radius for circular plates or the smaller linear dimension for rectangular plates).

Equation (3.1) is a modified version of the Bekker sinkage-pressure equation (2.2), also known as Bekker-Reece equation, where the ratio z/b is introduced for two reasons: make the parameters k'_c and k'_ϕ dimensionless and provide a single equation that accounts for different plate shapes. The exponent n , is crucial because it defines the trend of the relationship. Most soils behave almost linearly having n in the range of [0.8-1.2]. The density γ can be readily obtained while the cohesion c is usually calculated through a series of uni-axial and tri-axial compression tests [58]. The sinkage index n , and the constants k'_c and k'_ϕ are obtained using a bevameter or a penetrometer. These devices apply a constantly increasing load on a plate which is pushed perpendicularly down into the terrain. At the same time the sinkage is measured and the experimental data points are assumed to be represented by (3.1) with appropriately chosen parameters (a more detailed description of the procedure can be found in [18], a schematic representation of the test is shown 3.1).

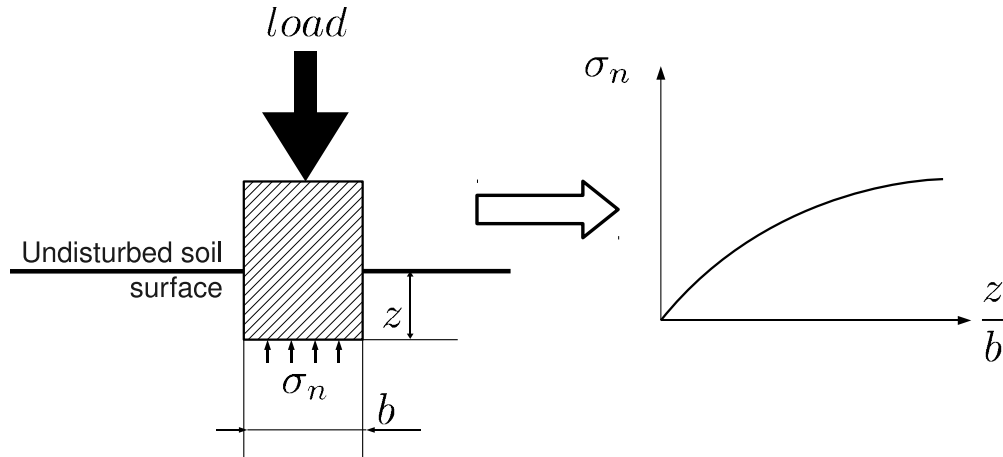


Figure 3.1: A schematic representation of the bevameter test. A load is applied on a penetrometer while sinkage z and normal pressure σ_n are recorded. The experimental data is then fitted with (3.1).

Direct terrain testing is not the only way to obtain terrain parameters. In the robotic field alternative methodologies to estimate terrain properties have been developed (primarily intended for unmanned vehicles). The novel approaches can be divided into two classes:

1. on-line parameter estimation,
2. computer vision terrain analysis.

The first strategy has been developed by Iagnemma [59, 60, 61] and consists of a parameter estimation algorithm based on the dynamics of the vehicle. The terrain properties can be estimated measuring the torque, the vertical load, the sinkage, and the slip ratio of the wheel: however, this assumes that the response of the wheel is well known (i.e. there is a need of an accurate tire model). The second strategy follows a computer science approach: a camera mounted on the vehicle takes a picture of the terrain and compares the picture with an internal database. Once the soil has been recognized (at least which kind of soil) its standard properties can be extrapolated [62, 63].

3.1.1 Discussion on the Use of the Reece Equation for Tire Stress Distribution Estimation

In the terramechanics community it is widely accepted to use the Reece-Bekker equation (3.1) to calculate the normal stress distribution along the contact patch of a tire. In order to have a better understanding of the limitations and features of this formulation some remarks are necessary. During the characterization of (3.1) the constants are obtained for a plate sinking perpendicularly to the terrain surface; the pressure acts along the z direction. For a sinking wheel, the stress calculated at any sinkage is considered to act along the radial direction of the wheel and not along the z direction. Another approximation is represented by the fact that the tire contact patch is thought as the penetrometer plate: the former has a round shape while the latter has a flat contact surface. The Reece equation is obtained under tri-axial loading conditions while the rotating tire not only exerts a vertical load but it also applies a shear during the penetration. It should be mentioned here that this formulation also assumes the terrain to be homogeneous and isotropic.

These approximations should be kept in mind in order to understand the great variability of experimental results.

3.2 Shear Stress

The calculation of the shear stress beneath the wheel is based upon an empirical expression first introduced by Janosi and Hanamoto [22] and widely used,

$$\tau_x(\theta) = \tau_{max} \left(1 - e^{-\frac{j_x}{k_x}} \right), \quad (3.2)$$

where:

τ_{max} = the limiting shear stress,

j_x = the shear displacement of the terrain,

k_x = the shear deformation modulus.

The shear deformation modulus can be obtained experimentally from shear tests and it has a strong impact on the prediction of the shear stress.

The limiting shear stress τ_{max} can be related to the normal stress through the Mohr-Coulomb equation:

$$\tau_{max} = c + \sigma_n(\theta) \tan \phi, \quad (3.3)$$

where:

c = soil cohesion (as previously stated in (3.1)),

ϕ = the angle of shear resistance or angle of internal friction.

It should be mentioned that the terrain below a rolling tire is under a complex stress state which theoretically is not properly represented by the Mohr-Coulomb failure criterion as expressed by (3.3). The shear displacement j_x is calculated integrating the shear velocity of the terrain in contact with the wheel (assuming that the velocity of terrain particles at the interface matches the velocity of the tire):

$$j_x(\theta) = \int_{\theta_b}^{\theta_e} R_{eff}(\theta) [1 - (1 - s_d) \cos(\theta)] d\theta \quad (3.4)$$

An example of tangential shear distribution is given in Figure 3.4b. Notwithstanding the discussed approximations, equations (3.2),(3.3), (3.4) have been shown to describe fairly well the shear distribution over a wide range of terrain [23].

3.3 Normal and Tangential Stress Distribution

The normal stress is calculated from (3.1) where the sinkage z is substituted by the following expression,

$$z = R_{eff}(\cos(\theta) - \cos(\theta_e)), \quad (3.5)$$

where:

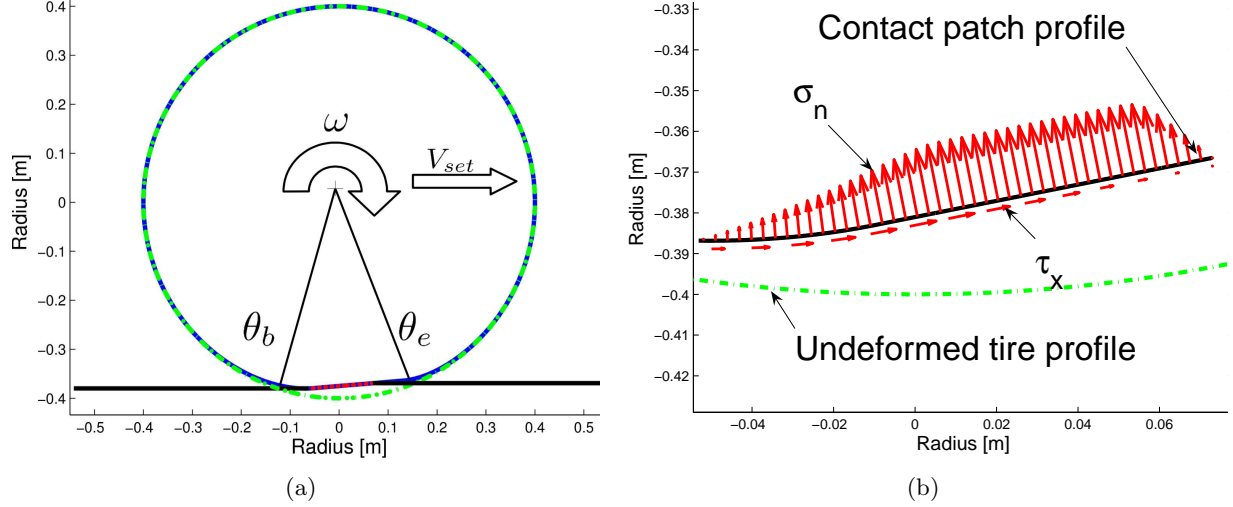


Figure 3.2: (a) An example of a deformed tire driven on a soft surface. The tire is deforming and sinking into the ground. (b) A detail of the contact patch area. The normal stress σ_n and the tangential stress τ_x acting along the contact patch are shown.

θ = the central angle (i.e. the angle describing the angular position of the tire element starting counterclockwise from the bottom of the tire).

θ_e = the entry angle (i.e. the angle at which the terrain enters in contact with the wheel).

R_{eff} = the effective radius which will be discussed later in section 3.4.

Substituting (3.5) into (3.1) leads to a pressure distribution along the contact patch that starts from zero at the entry angle and monotonically increases. The maximum is reached at the point where the highest sinkage occurs; this point, for a rigid wheel, is necessarily located at the bottom of the wheel. This method has been adopted by Harnisch et al. [5] but it should be noted that experiments and the theory of plastic equilibrium [37, 18, 64] show that the maximum of the pressure distribution occurs somewhere half-way between the entry and exit angles and is a function of the slip ratio; even though the sinkage increases monotonically from the entry angle to the bottom of the wheel, the stress distribution does not follow this trend (see Fig. 3.3).

In order to reproduce a stress distribution similar to the one highlighted in the experiments, the normal stress is defined in this study as a piecewise function [6]. From the leading edge θ_e to the location of the maximum normal stress, θ_m , the stress is calculated using (3.6),

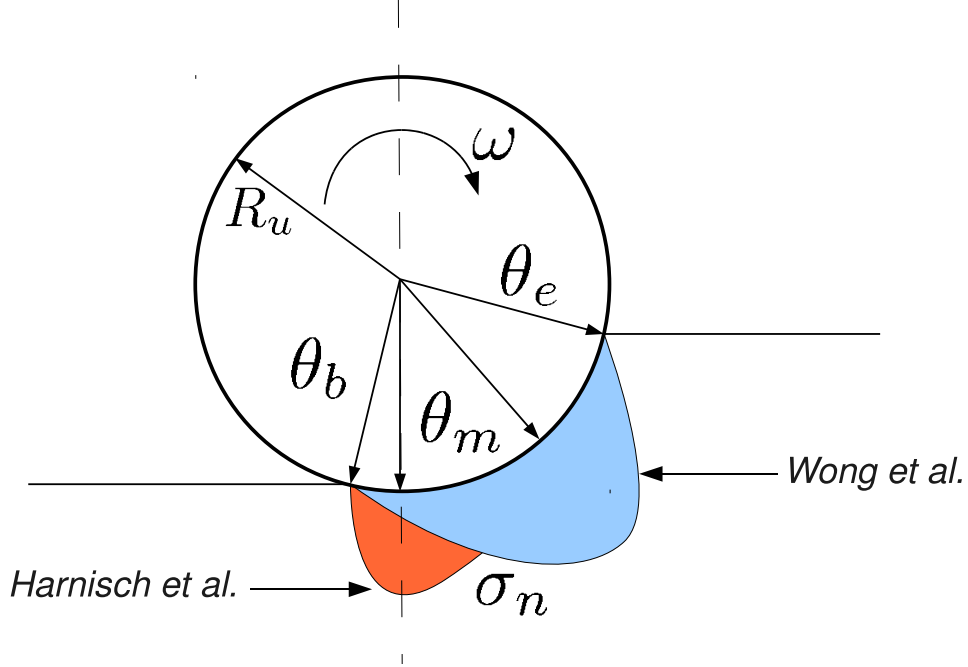


Figure 3.3: A schematic representation of the normal stress distribution as adopted by Harnisch et al. [5] and by Wong et al. [6]. In this study, Wong's approach is used.

$$\sigma_{nf}(\theta) = (ck'_c + b\gamma_s k'_\phi) \left(\frac{R_{eff}}{b} \right)^n (\cos(\theta) - \cos(\theta_e))^n, \quad (3.6)$$

while the normal stress that goes from the maximum stress point, θ_m , to the trailing edge, θ_b , can be evaluated by (3.7),

$$\sigma_{nr}(\theta) = (ck'_c + b\gamma_s k'_\phi) \left(\frac{R_{eff}}{b} \right)^n \left(\cos \left(\theta_e - \left(\frac{\theta - \theta_r}{\theta_m - \theta_r} \right) (\theta_e - \theta_m) \right) - \cos(\theta_e) \right)^n. \quad (3.7)$$

In these equations the quantity b is defined as:

$$b = \min(l'_p, w), \quad (3.8)$$

where l'_p is the projected contact patch length and w is the tire width. This distinction is important because for some tire geometry the smallest dimension of the contact patch is the contact patch length and not the tire width. An example of normal stress distribution is given in Figure 3.4.

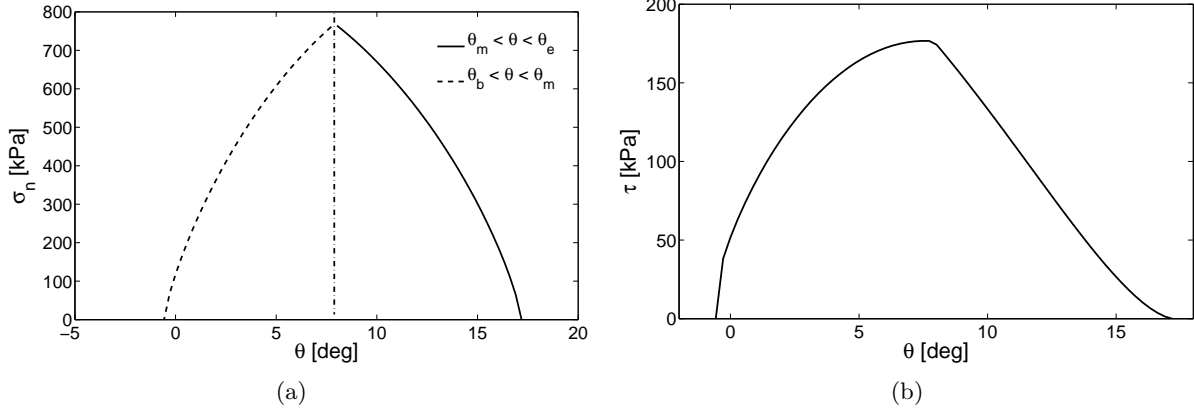


Figure 3.4: (a) Normal stress distribution along the contact patch of a driven ($s_d = 0.2$) rigid wheel. The stress increases from the entry angle θ_e , reaches the maximum at θ_m , and decreases back to zero at the exit angle θ_b . (b) Tangential stress distribution along the contact patch under the same assumptions.

With this implementation it is crucial to correctly estimate the value of θ_m . Chan and Sandu [26] proposed a method based on the Mohr-Coulomb failure criterion and the theory of plastic equilibrium: this approach is elegant but does not always lead to accurate results in terms of sinkage prediction [26, 65]. In this study, θ_m is thought to be a linear function of the slip ratio and the entry angle. This is an empirical estimation successfully implemented in other studies [6, 66, 67].

$$\theta_m = (c_0 + c_1|s_d|)\theta_e, \quad (3.9)$$

c_0 and c_1 are two constants. Since θ_m is usually half-way between the entry angle and exit angle, c_0 can be selected in the range of $[0.4, 0.5]$ and $c_1 \in [0.2, 0.4]$ (this has been verified in [6]). Equation (3.9) guarantees that θ_m increases with the slip resulting in a better prediction of slip-sinkage behavior. Another method adopted to improve the calculation of slip-sinkage is to linearly relate the sinkage exponent n to the slip ratio [67].

$$n = n_0 + n_1|s_d| \quad (3.10)$$

This is again an empirical approximation but it contains some physical insight. The exponent n is experimentally obtained for steady soil loading tests performed with a penetrometer. The response of the soil in contact with a rolling/slipping tire is presumably

different. Equation (3.10) describes this phenomenon as suggested in [67].

3.4 Rigid Wheel and Flexible Tire

A tire operating on deformable soil can be approximated as a rigid wheel if the pressure distribution along the contact patch does not exceed the inflated carcass stiffness. When this is verified the effective radius is a constant, and it equals the undeformed radius, $R_{eff} = R_u$. When the inflated carcass pressure is exceeded, the tire deforms and a different approach is needed. The problem becomes extremely complex because both the tire and the terrain are deformable. Chan and Sandu proposed to calculate the deflected shape of the tire through the following equation:

$$R_{eff} = \begin{cases} R_u - R_u \left(1 - \frac{1 - \frac{\delta}{R_u}}{\cos(\theta)} \right) & \text{if } \theta_r < \theta \leq \theta_f \\ R_u - R_u \left(1 - \frac{1 - \frac{\delta}{R_u}}{\cos(\theta_f)} \right) e^{-\beta(\sqrt{1+\zeta^2+\zeta})(\theta-\theta_f)} & \text{if } \theta_f < \theta \leq \pi \\ R_u - R_u \left(1 - \frac{1 - \frac{\delta}{R_u}}{\cos(2\pi+\theta_r)} \right) e^{\beta(\sqrt{1+\zeta^2-\zeta})(\theta-(2\pi+\theta_r))} & \text{if } \pi < \theta \leq 2\pi + \theta_r \end{cases} \quad (3.11)$$

ζ and β are two parameters related to the stiffness, damping, size, inflation pressure, angular velocity and construction of the tire and are obtained experimentally [26, 68, 69, 70]. An example of a deformed tire is given in Fig. 3.5. The tire has a flat shape between the angles θ_f and θ_r and a round shape (connected through a logarithm spiral) elsewhere.

The Harnisch et al. model [5] adopts the larger substitute circle to model the behavior of an elastic tire. The basic principle was suggested by Bekker but never carried out because of the complexity of the calculation. This approach consists in the substitution of a larger radius for the calculation of the contact patch: this allows one to have a flatter contact region that mimics the shape of a deflected tire. This approach led to satisfactory results, but in this study the method proposed by Chan and Sandu is preferred because:

- it provides a more solid theoretical approach,
- the shape parameters can be calculated from physical characterization tests,

- it directly relates tires properties such as the inflation pressure and the carcass stiffness to the tire vertical deformation (a parameter easily obtainable from direct testing),
- the calculated shape matches the experimental results obtained by Freitag [71].

Freitag [71] showed that a driven tire tends to assume an undeformed rigid wheel shape for increasing slip ratio. In order to simulate this behavior the inflation pressure is artificially related to the slip ratio,

$$p_i = p_0 + p_1 |s_d|, \quad (3.12)$$

where p_0 is the original inflation pressure and p_1 is a constant. Equation (3.12) guarantees that the tire deflection decreases for high slip operations (this behavior has been measured also by Holm [7]).

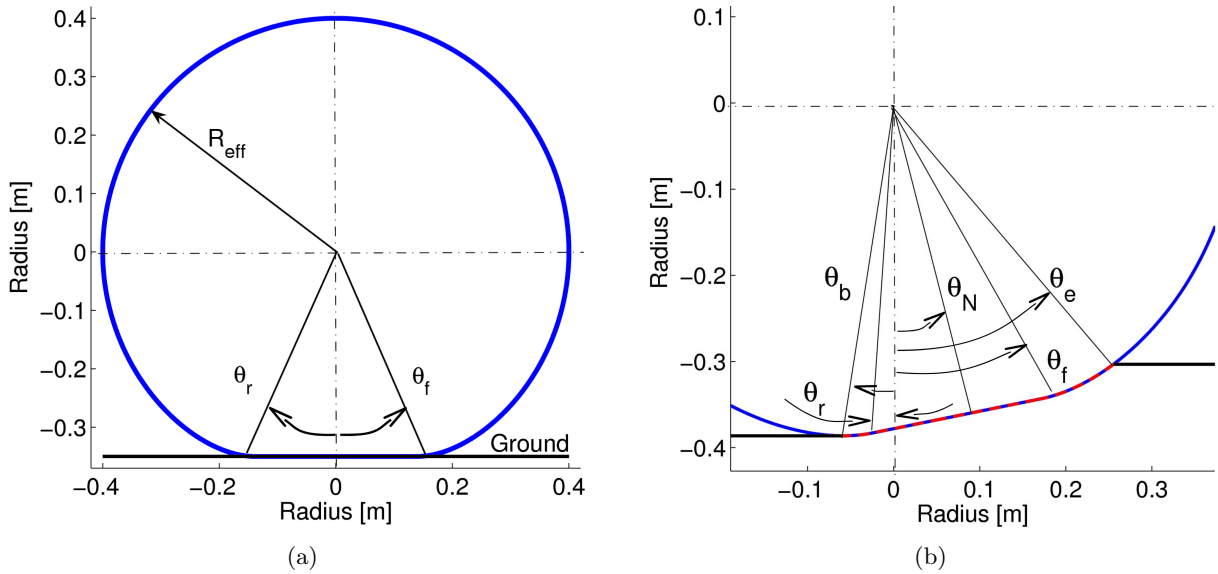


Figure 3.5: Exaggerated plot of a deformed tire sitting on hard surface (a) and driven on a soft terrain (b). When stationary the only portion in contact with the terrain is the flat region between θ_r and θ_f which in this particular configuration correspond to θ_b and θ_e . When the tire is rolling, the section of maximum deflection is rotated on an angle $\theta_m = \frac{\theta_f}{2}$ and the entry and exit angle $\theta_{e,b}$ don't necessarily correspond to θ_f and θ_r .

When the tire is driven on deformable soil, the flat section between θ_f and θ_r (first line of (3.11)) rotates counterclockwise [71, 37]. This phenomenon determines the amount of sinkage and it is a function of the slip, the vertical load and the inflation pressure. Assuming that the maximum deflection of the tire corresponds to the point where the maximum stress occurs,

the rotation of the flat section can be set equal to the angle θ_m . For flexible implementation θ_m is calculated as follow,

$$\theta_m = (c_0(F_z, p_i) + c_1(F_z, p_i)|s_d|)\theta_e. \quad (3.13)$$

Equation (3.13) is identical to (3.9) but the terms c_0 and c_1 are now a function of the vertical load F_z and inflation pressure p_i . This ensures that the predicted sinkage increases with vertical load and decreases with inflation pressure.

3.5 Drawbar Pull, Driving Torque, and Lateral Force

Once the normal and tangential stress distributions are known it is possible to calculate the drawbar pull and the driving torque. The balance of vertical forces needs to be calculated first: it ensures that the vertical force produced along the contact patch balances the vertical load of the vehicle, as given in (3.14),

$$W = w \int_{\theta_b}^{\theta_e} R_{eff}(\theta) (\sigma_n(\theta) \cos(\theta_{eff}) + \tau_x(\theta) \sin(\theta_{eff})) d\theta, \quad (3.14)$$

where W is the weight force of the vehicle and the right hand side term represents the integrated stress along the contact patch acting in the vertical direction (i.e., the vertical force exerted by the tire). The tire width is w while θ_{eff} is the effective angle that the deformed tire shape creates with the vertical axis; for the rigid wheel model θ_{eff} is equal to θ . In (3.14) we have two unknowns: the entry angle θ_e and the exit angle θ_b . The exit angle is smaller than the entry one because the wheel (rigid or flexible) is sinking into the ground and while it is moving forward it compacts the terrain, as seen in Fig. 3.2. Since no other analytical expressions can be derived, θ_b is estimated as follows (a distinction between the rigid wheel and flexible tire operational mode is required):

For rigid wheel implementation, the exit angle is assumed to be constant and small in magnitude. The wheel necessarily leaves the terrain flat and so the exit angle cannot physically be large (indeed, it is not equal to zero because of frictional phenomenon that

displace the ground under the rotating wheel and because of the elastic response of the terrain).

For flexible tire implementation we propose to calculate the exit angle based on the lowest point in contact with the terrain. After calculating the shape of the tire (3.11) and the counterclockwise rotation (i.e., θ_m calculated in (3.13)) it is assumed that the lowest point in the tire deformed configuration is the last point in contact with the terrain and θ_b is calculated accordingly; the entry angle θ_e is still determined by (3.14). The value of the exit angle plays an important role in the determination of tractive performance. In fact, θ_b influences the size and location of the contact patch and can drastically change the model outcome.

The drawbar pull (which will be labeled as F_x) is calculated from the integration of the normal and shear stresses decomposed along the longitudinal direction,

$$F_x = w \int_{\theta_b}^{\theta_e} R_{eff}(\theta) (\tau_x(\theta) \cos(\theta_{eff}) - \sigma_n(\theta) \sin(\theta_{eff})) d\theta. \quad (3.15)$$

It should be mentioned that this expression already includes the soil compaction resistance, given by the last term of the integral.

The driving torque is given by the following expression:

$$T = w \int_{\theta_b}^{\theta_e} R_{eff}^2(\theta) \tau_x(\theta) d\theta. \quad (3.16)$$

The lateral force F_y is generated by the lateral shear displacement j_y and by the bulldozing effect (due to the tire sinkage and soil surcharge, see Fig. 3.6). The component F_{ys} associated with the lateral shear is calculated similarly to (3.2), as given in (3.17),

$$F_{ys} = w \int_{\theta_b}^{\theta_e} \tau_y(\theta) d\theta = w \int_{\theta_b}^{\theta_e} (c + \sigma_n(\theta) \tan(\phi)) \left(1 - e^{\frac{-j_y}{k_x}}\right) d\theta. \quad (3.17)$$

The lateral force F_{ybd} associated with the bulldozing effect is calculated as a function of the sinkage, z , as presented in (3.18),

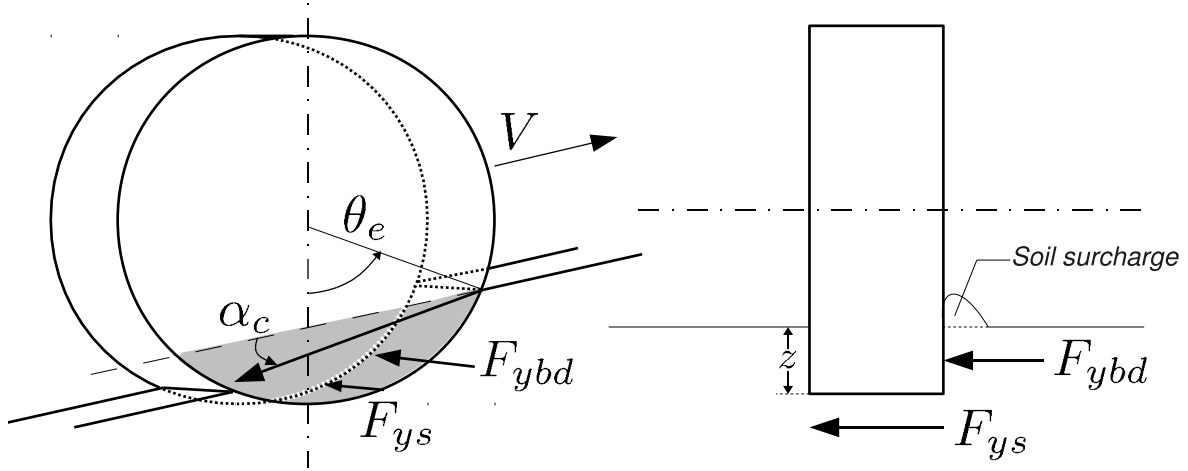


Figure 3.6: A schematic representation of the lateral force generation. The lateral force is composed of two components: the shear force in the lateral direction F_{ys} and the bulldozing force F_{ybd} . The first one is due to the lateral slip of the tire imposed by the steering action. This force acts along the contact patch beneath the tire. The bulldozing force acts on the side of the tire and is due to the wheel compacting the terrain in the lateral direction.

$$F_{ybd} = w \int_{\theta_b}^{\theta_e} (\gamma_s z^2 N_\gamma + cz N_c + qz N_q) \cos(\delta_f) d\theta, \quad (3.18)$$

where

N_γ = soil specific weight coefficient,

N_c = soil cohesion coefficient,

N_q = soil surcharge load coefficient,

q = surcharge load from accumulated bulldozed soil,

δ_f = angle between the normal to the surface of the wall and the direction of motion.

Equation 3.18 is based on the Hettiaratchi-Reece equation [32] for a wall moving into a mass of soil and was adopted for the first time by Schwanghart [31], to model the lateral stress due to sinkage. The total lateral force acting on the tire can be calculated through:

$$F_y = F_{ys} + F_{ybd}. \quad (3.19)$$

During combined slip operation the lateral and longitudinal shear stresses acting at the contact patch are limited by a failure envelope. The following criterion is adopted:

$$\left(\frac{\tau_x}{\tau_{xmax}}\right)^2 + \left(\frac{\tau_y}{\tau_{ymax}}\right)^2 \leq 1. \quad (3.20)$$

During cornering the soil undergoes complex loading state and the adoption of (3.20) represents only the first approximation as previously discussed for the definition of τ_{max} .

3.6 Multi-Pass Effect

The multi-pass effect has a strong impact on the evaluation of the traction of off-road vehicles. Repetitive loading of deformable soils showed that during the unloading and reloading process the pressure-sinkage relation can be approximated with a straight line [18, 21]. An example of repetitive loading is given in Figure 3.7. A body of undisturbed soil undergoes an initial loading from 0 to A. The unloading and successive reloading follows the dashed line to point B. The same happens with successive reloading. The pressure-sinkage from 0 to A is modeled with Reece equation 3.1 while Wong [23] suggests to model the section AB as follow:

$$\sigma = p_u - k_u(z_u - z) \quad (3.21)$$

where

p_u = pressure when the unloading begins (A or C),

z_u = sinkage when the unloading begins (A or C),

k_u = terrain stiffness parameter representing the average slope of the unloading-reloading section (AB or CD).

The terrain stiffness k_u is found to be a function of z_u , and Wong proposes a linear approximation to model it:

$$k_u = k_0 + A_u z_u \quad (3.22)$$

where k_0 and A_u are soil dependent parameters that can be calculated from experimental data.

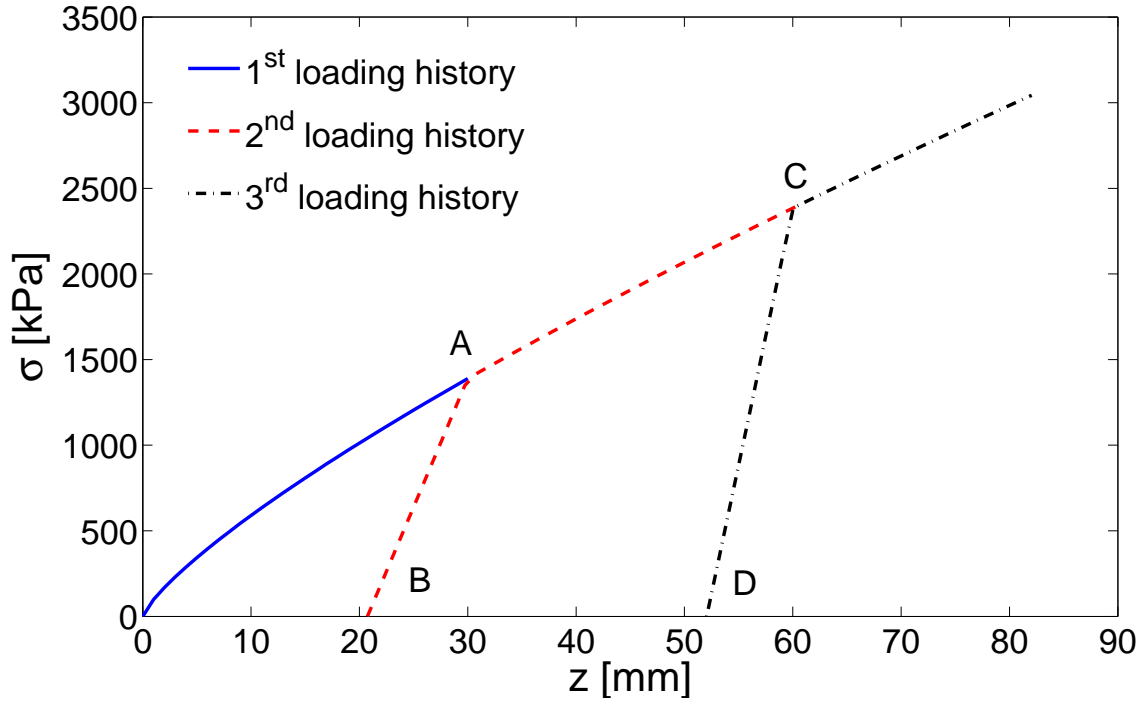


Figure 3.7: Response to repetitive load of a mineral terrain.

The modeling of repetitive loading introduced by Wong cannot be directly implemented into the model because of the way the normal stress along the contact patch have been obtained (a piecewise function that does not strictly follow the monotonic trend of the sinkage). The repetitive loading method proposed by Wong was directly implemented by Harnisch et al. [5]. They estimated the normal stress strictly following the pressure-sinkage equation (see Fig. 3.3), the stress reach the maximum for the maxim value of sinkage). This allowed them to straightforwardly calculate the multi-pass effect following the repetitive loading curve of Figure 3.7.

In this thesis a different approach is taken. The most relevant study concerning the multiple pass of wheels on the same patch of terrain is the one performed by Holm [7]. The

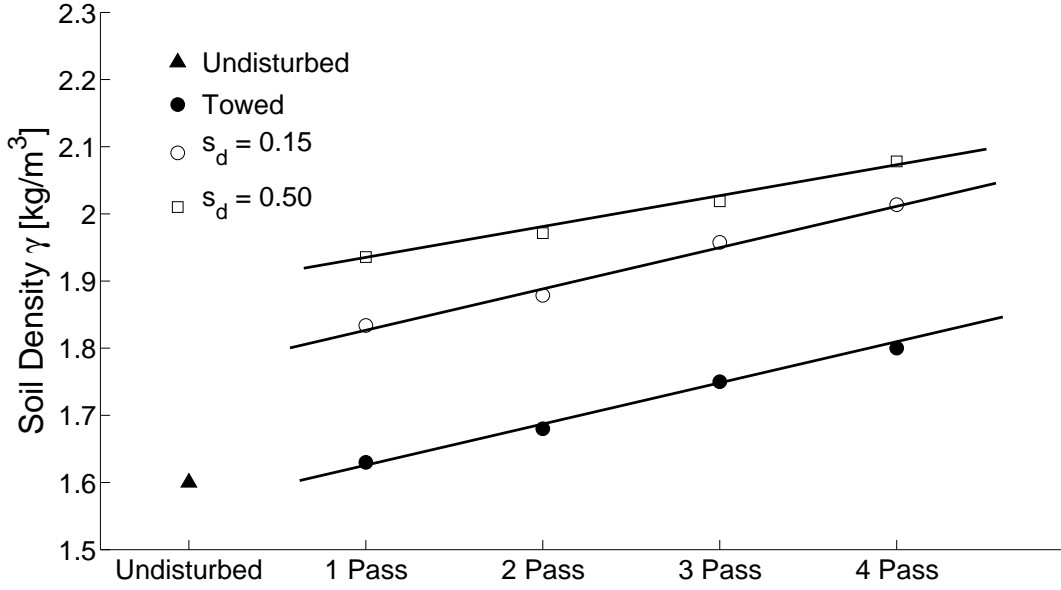


Figure 3.8: Example of terrain properties variation for multiple passage. The data has been extrapolated from the Figure 25 of [7] and regards a loam soil with fine grained sand at 16.5% of moisture content.

study shows that the terrain changes its properties after each pass and the variations are a function of the slip. If the first wheel is towed (zero torque pass) the terrain properties vary mildly, while the passage of a slipping tire produces a stronger effect on the soil, as shown in Figure 3.8. Terrain density increases after each pass and, considering the obtained results and related work from Bekker [21], also the cohesion of the material is considered to have increased. The greatest variation occurs between the first and second pass: successive runs have less impact on the behaviour of the terrain. This phenomenon is incorporated into the model introducing a dependency of soil properties c , γ_s , and k_x upon the number and type of passes,

$$c = (c + c_{sd}) + c_1 s_d, \quad (3.23)$$

$$\gamma_s = (\gamma_s + \gamma_{sd}) + \gamma_{s1} s_d, \quad (3.24)$$

$$k_x = (k_x + k_{sd}) + k_{x1}s_d, \quad (3.25)$$

where the parameters c_{sd} , γ_{sd} , and k_{sd} are functions of the type of pass. For a pass of a towed wheel they are equal to zero while they increase for passages performed at higher slip. Parameters c_1 , γ_{s1} , and k_{x1} are functions of the number of passes and determine the variation of soil properties after each pass.

3.7 Results

The results are divided into two subsections: dry sand and moist Yolo loam. Dry sand is a non-cohesive and loose soil; on such terrain the inflated carcass pressure is never exceeded and the tire operates as a rigid wheel. The Yolo loam is a firmer soil which exhibits a steeper pressure-sinkage curve; on this terrain both the soil and the tire deforms. The aforementioned sections will discuss the longitudinal and lateral traction, the sinkage and the multi-pass effect. The soil and tire properties adopted in this thesis are taken from [26] and summarized in Tables 3.1, 3.2.

No direct testing has been performed; the capabilities and features of the model are compared with literature data. In the case of rigid wheels on dry sand the data collected under known experimental setup by B. Taylor [65] is explicitly presented and discussed.

Table 3.1: Undisturbed soil properties adopted in the simulations.

Soil	k'_c	k'_{phi}	n	c [Pa]	ϕ [deg]	k_x, k_y [m]	γ_s [kg/m ³]
Dry Sand	2	17,658.75	0.77	130	31.1	0.038	15,696
Yolo Loam	3.25	4,600	0.99	22,670	22	0.015	12,341

Table 3.2: Nominal tire properties adopted in the simulations.

R_u [m]	w [m]	p_i [kPa]
0.4	0.265	240

3.7.1 Dry Sand - Rigid Wheel

Longitudinal Motion

On dry sand the tire operates as a rigid wheel. Figure 3.9 shows the trend of the drawbar pull and torque versus the slip ratio at different vertical loads. The longitudinal force is much higher (in absolute value) for negative slip because of the sinkage phenomenon: the terrain compaction force always acts against the direction of travel.

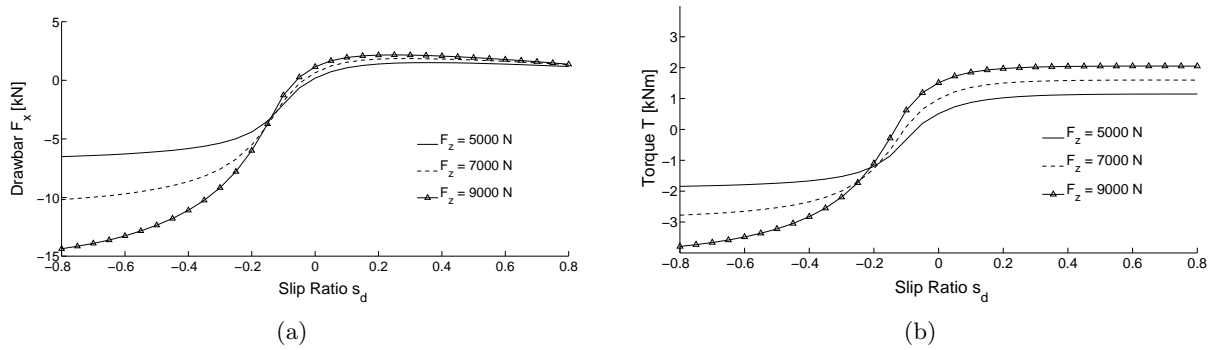


Figure 3.9: Trend of drawbar pull (a) and driving torque (b) for different vertical loads and slip ratio. Results obtained for a rigid wheel running on dry sand.

Figure 3.10 presents a comparison between experimental data and the model proposed in this thesis. The tested wheels are rigid rims without lugs and the following geometric properties: 20x7, 32x7 and 32x11 (*diameter x width* in inches).

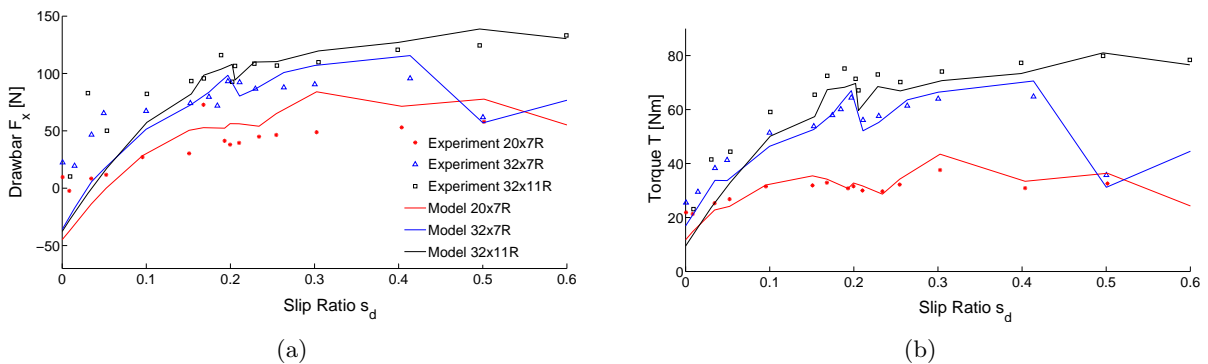


Figure 3.10: Experimental data compared with the model prediction. Rigid wheels with different geometries have been tested on dry sand.

The nominal vertical load is set to 507N, but for technical reasons, it does not remain constant during the test [65]; this partially explains the scatter in the data. For this reason,

the results are obtained using the measured vertical load instead of the nominal one (it should be mentioned that [65] used the nominal vertical load to fit the data). The figures show that the model is able to predict fairly well the performance of the three wheels for positive slip: in particular, it shows to be sensitive to the wheel geometry. For negative slip, the model is in poor agreement with the experiments.

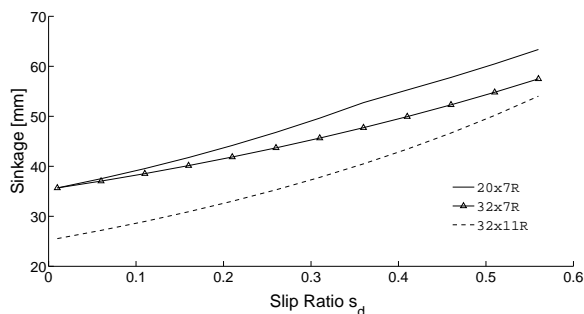


Figure 3.11: Slip-sinkage behavior of rigid wheels of different geometries.

Figure 3.11 presents the slip sinkage behavior predicted. The trend is qualitatively in agreement with experimental results presented in [67, 72]: the sinkage continuously increases with slip and larger wheels sink less.

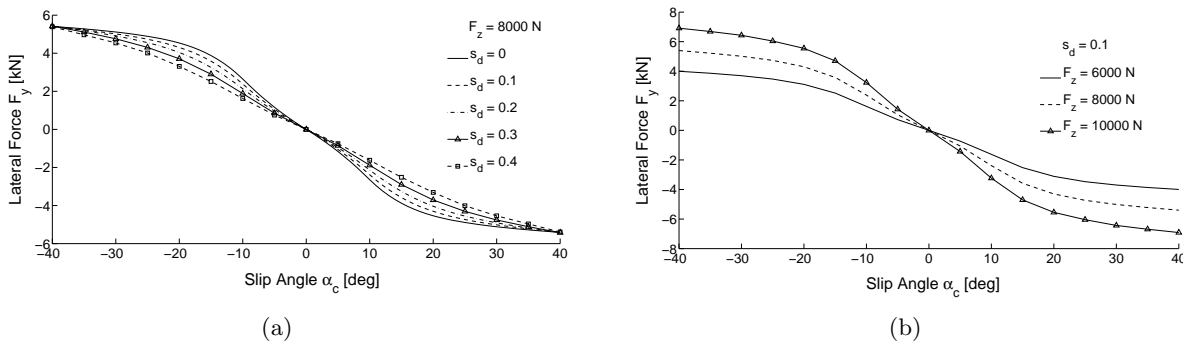


Figure 3.12: Lateral force versus slip angle for different slip ratios (a) and vertical loads (b). Results obtained for a rigid wheel on dry sand.

Lateral Motion and Combined Slip

Figure 3.12 shows the trend of lateral force versus slip angle α_c for various slip ratios and vertical loads. While tires rolling on hard surfaces (i.e., on-road) show a flat response for higher slip angle this does not happen on soft terrain: the lateral force does not exhibit a maximum. This happens because the lateral force is due not only to the shear displacement

at the contact patch but also to the bulldozing effect (3.19). The term F_{ys} saturates for large slip angles but the term F_{ybd} monotonically increases because of the slip-sinkage phenomenon. Same results have been obtained by [31].

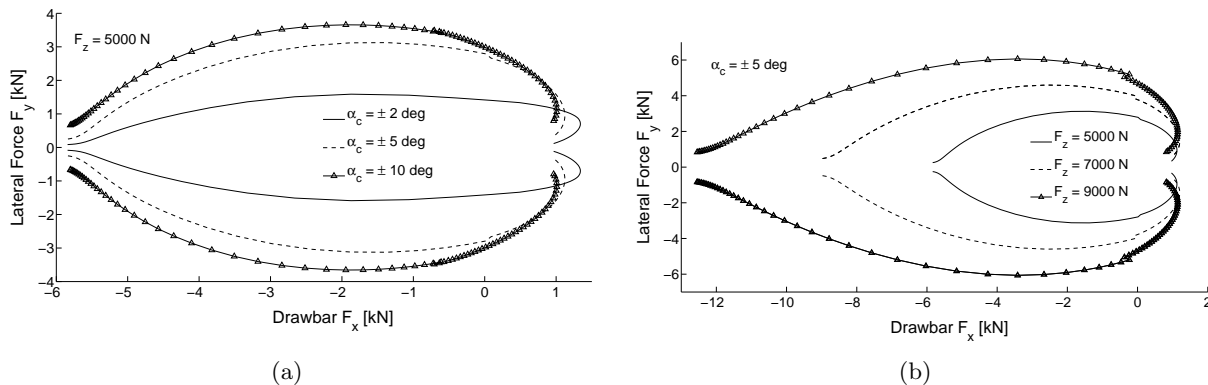


Figure 3.13: Combined slip envelope for different slip angles (a) and vertical loads (b). Results obtained for a rigid wheel on dry sand.

Figure 3.13 presents the combined slip F_y vs. F_x for various slip angles and vertical loads. The plot is biased towards negative values of drawbar pull because of the slip-sinkage behavior. The combined slip envelopes degenerate for larger slip angles: during off-road maneuvering the forces that the tire is able to exchange with the terrain are limited. For modest values of vertical loads (compared to the tire geometry) it is possible to obtain combined slip results for larger slip angles [73]

Multi-pass on Dry Sand

The multi-pass effect can radically change the performance of tires rolling into ruts created by other tires of the same or other vehicles. Figure 3.14 shows the variations of drawbar pull and sinkage for multiple passages predicted by the model. As mentioned previously the way the first pass is performed affects the terrain properties and the performance of the second pass. This has direct implications for multi-axle vehicles where only some of the axles are driven. The drawbar pull increases at the successive passages while the relative sinkage decreases because of terrain compaction.

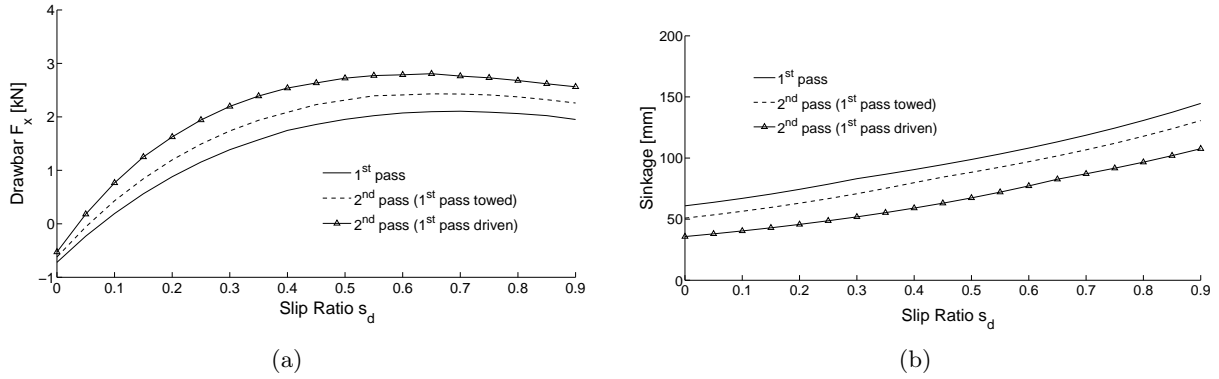


Figure 3.14: Multi-pass influence on the performance of rigid wheels on dry sand. In (a) the longitudinal force is presented while (b) shows the relative sinkage.

3.7.2 Moist Yolo Loam - Flexible Tire

Longitudinal Motion

On moist Yolo loam the tire operates in the flexible mode. The loam being a firmer soil, the sinkage effect is reduced, this leads to improved drawbar pull capabilities. Figure 3.15 shows the trend of the drawbar pull and torque versus the slip ratio at different vertical loads.

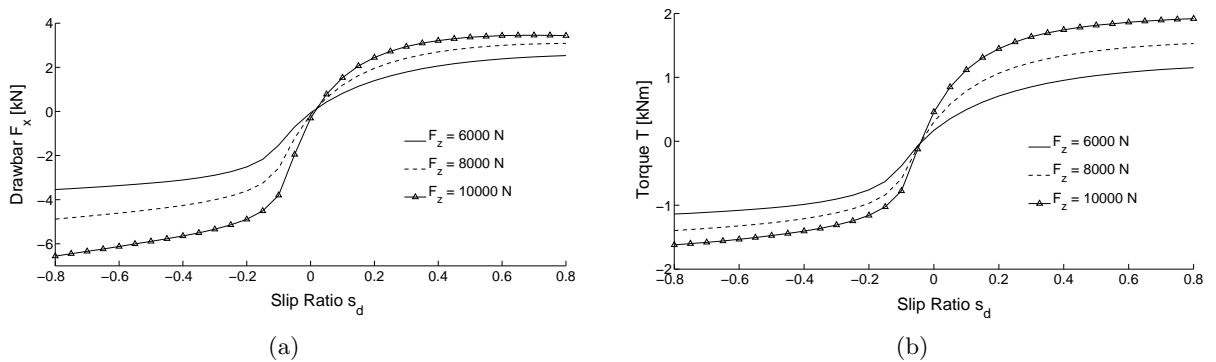


Figure 3.15: Trend of drawbar pull (a) and driving torque (b) for different vertical loads and slip ratio. Results obtained for flexible tire on moist Yolo loam.

Figure 3.16 presents the drawbar pull and the sinkage at various inflation pressure. Decreasing the inflation pressure provides a larger contact patch that helps improve the traction and at the same time reduces the sinkage [74].

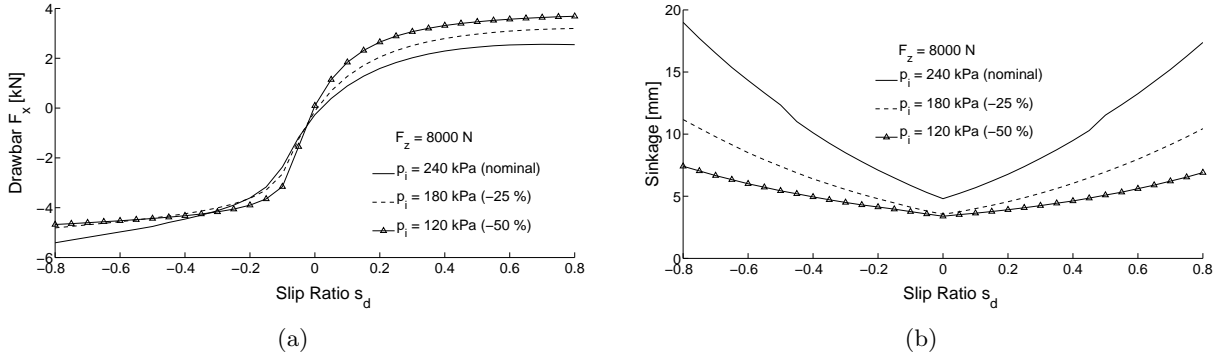


Figure 3.16: Variation of drawbar pull (a) with inflation pressure and trend of the sinkage (b) with inflation pressure. Results obtained for flexible tire on moist Yolo loam.

Lateral Motion and Combined Slip

Figure 3.17 shows the trend of lateral force versus slip angle α_c for various slip ratios and vertical loads. The results are similar to the ones obtained with rigid wheels on dry sand; the lateral force does not exhibit a maximum or a plateau.

Figure 3.18 presents the combined slip F_y vs. F_x for various slip angles and vertical loads. Also, in this case, the flexible tires behave similarly to the rigid wheels. However, larger slip angles can be reached during combined slip maneuver.

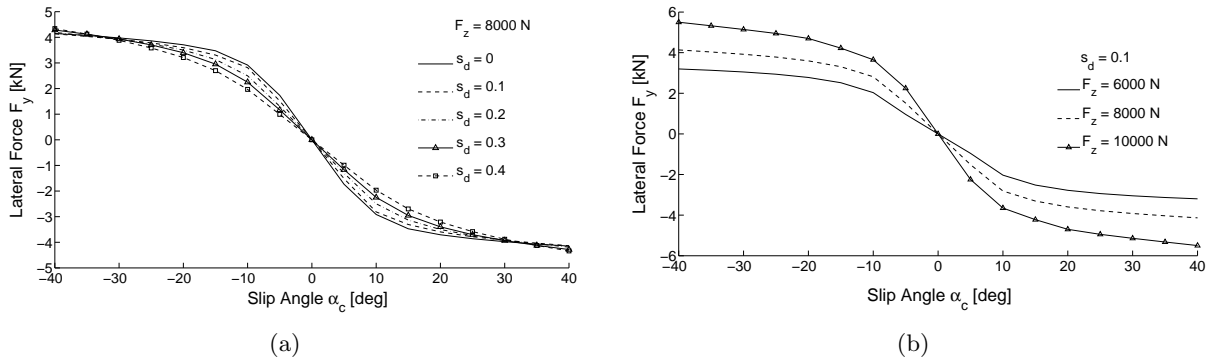


Figure 3.17: Lateral force versus slip angle for different slip ratio (a) and vertical load (b). Results obtained for flexible tire on moist Yolo loam.

On dry sand, conspicuous sinkage generated large resistance forces in the longitudinal direction: this limited the combined slip. When the tire is steered the ability to produce longitudinal force (in the tire-fixed reference frame) suddenly drops: the phenomenon is more significant in dry sand because of the larger sinkage.

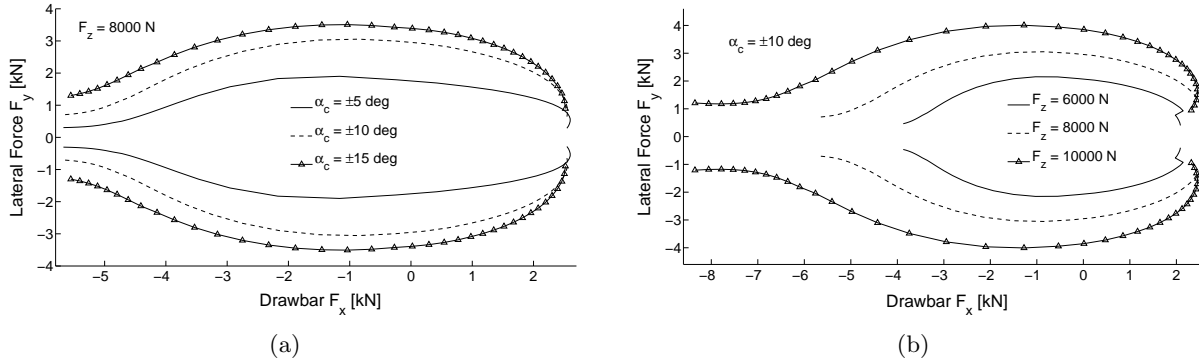


Figure 3.18: Combined slip envelope for different slip angles (a) and vertical loads (b). Results obtained for flexible tire on moist Yolo loam.

Multi-pass on Moist Yolo Loam

Also when the tires behaves in a flexible way the multi-pass effect produces similar results. Successive passes increase the traction capability and decrease the relative sinkage, this is shown in Figure 3.19.

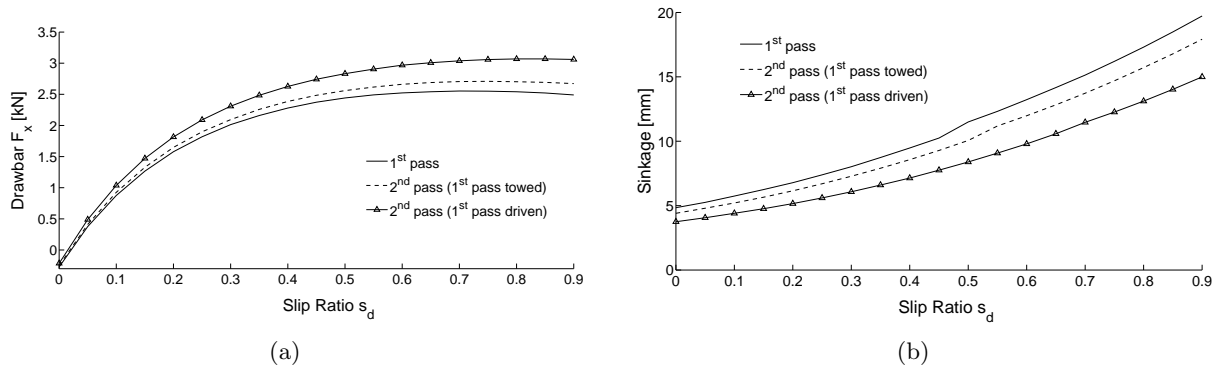


Figure 3.19: Multi-pass influence on the performance of flexible tires on moist Yolo loam. (a) presents the variation of longitudinal force while (b) the relative sinkage for multiple passages over the same patch of terrain.

3.8 Considerations

In this chapter, an enhanced off-road capable tire model has been developed. The semi-empirical approach, well established in the terramechanics community, has been discussed and improved in order to combine, into a single model all the salient features that an off-road tire exhibits. The model is sensitive to tire geometry and consistently predicts the response

to variable tire sizes and inflation pressure.

The results show that it is licit to assume the sinkage exponent n is a function of the slip. This ensures a more accurate estimate of the sinkage without deteriorating the prediction of the traction and torque. An adequate tuning of the parameters introduced in the (3.10), (3.9), (3.12), (3.23), (3.24), (3.25) allows one to obtain from a single model consistent measures of drawbar pull, torque, lateral force, sinkage, multi-pass effect. These parameters can be identified from terrain and tire testing.

The results obtained in this chapter will be exploited in following chapters to analyze the efficiency of tires rolling on deformable terrain (Chapter 4) and to simulate a full vehicle (Chapter 5).

Chapter 4

Tractive Efficiency

The efficiency of land vehicles (on and off-road) depends on three main factors:

- Power-train: thermodynamic losses in the engine and frictional losses in the engine and drive-train.
- Aerodynamics: frictional and shape losses to the the viscous effects of the air flowing around the vehicle.
- Tire rolling resistance: resistance force that develops at the tire-terrain interface. For on-road applications this is mainly due to the hysteresis of the tire while in off-road to the terrain compaction (the hysteresis phenomenon is still present but on a reduced scale).

This study does not consider the first two aspects, however, a brief description of their influence will be given in the next sections.

It should be kept in mind that the efficiency is largely influenced by the mass of the vehicle. Figure 4.1 shows the energy requirement for different driving conditions [8]; during a standard city cycle, the acceleration contribution (directly related to the vehicle mass) is predominant. For highway operations, when the traveling velocity stays constant, the mass has no impact; on the contrary it is interesting to notice that the rolling resistance has a steady impact.

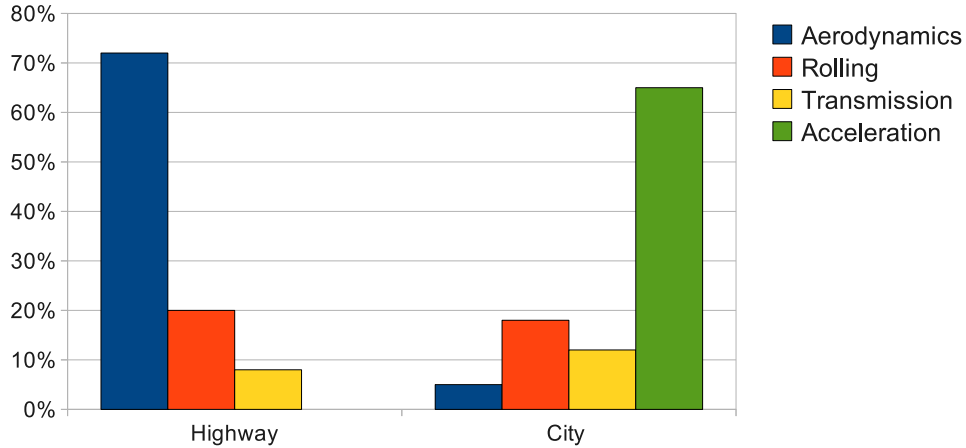


Figure 4.1: Energy requirement for two driving conditions [8].

4.1 Power-train Efficiency

In a motor vehicle, the term power-train refers to the group of components that generate power and deliver it to the road surface, water, or air. This includes the engine, transmission, drive-shafts, differentials, and the final drive. Large off-road vehicles usually adopt internal combustion engines while small robotic vehicles preferably implement electric motors. A brief description of the efficiency of both solutions will be given.

4.1.1 Internal Combustion Engine

In the internal combustion engine (ICE) the combustion of a fuel (generally fossil fuel) with an oxidizer (usually air) produces an expansion of high temperature and pressure gases that, acting on the movable piston(s), generates useful mechanical work. In this section, some of the relevant features of internal combustion engines will be discussed; for an exhaustive dissertation on the topic the reader can refer to specialized books [75, 76, 77].

The torque/power vs. RPM (revolution per minute) plot of an engine provides useful information regarding engine performance. Figure 4.2 presents the engine power/torque curves for a large displacement engine (the plot has been created bearing in mind the specification of a large SUV engine). In the automotive practice these plots are obtained at full load (full throttle overture) and they provide concise information of the vehicle's performance.

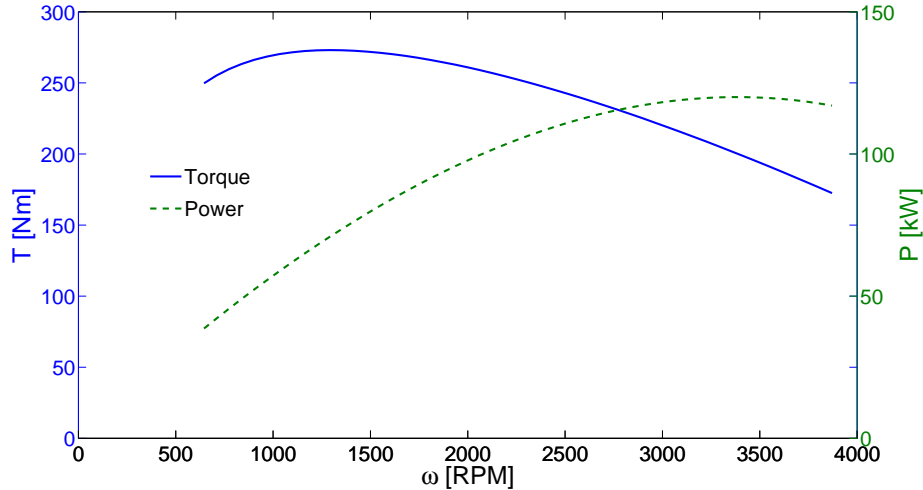


Figure 4.2: Exemplar torque/power curve for an engine. The maximum output power is 120 kW at 3300 RPM, while the maximum torque is 270 Nm at 1450 RPM.

However, the power/torque curves do not provide any information regarding the efficiency of the engine.

A measure of the fuel consumption is given by the brake specific fuel consumption (BSFC) map presented in Figure 4.3 [8, 78]. The BSFC has a maximum close to the maximum of the torque at full load (the thicker blue line represents the torque at full load), this means that the engine reaches its peak of efficiency if operated at full load at 1700 RPM and 80 kW. A careful analysis reveals that for a given power requirement the engine is more efficient if operated at lower RPM: on a manual transmission it is always better to drive with the highest possible gear in order to be more efficient.

The gearbox of a car is designed in such a way that for every driving condition the engine works as close as possible to the efficiency peak. One of the drawbacks is represented by the fact that the peak of efficiency occurs at full load: in realistic driving conditions it is not convenient to drive in the vicinity of the peak because no reserve of power is available.

For example, consider a car traveling at constant velocity. Suppose that 80 kW of power are needed to overcome all the resistances (road grade resistance, aerodynamic resistance, rolling resistance). The engine of this car would work somewhere on the curve of constant 80 kW power of Fig. 4.3. The exact location depends on the ratio between the tire angular velocity and the engine shaft velocity, which is determined by the differential and the gearbox.

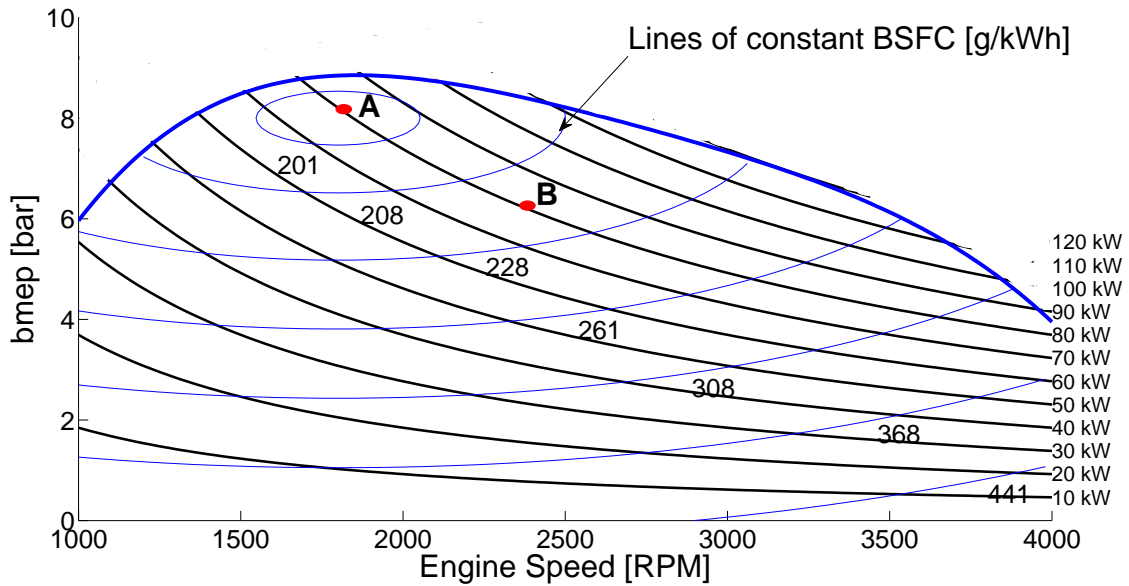


Figure 4.3: Map of a diesel engine. The power/torque specifications are the same as Figure 4.2. The *islands* represent lines of constant Brake Specific Fuel Consumption (BSFC), the grams of fuel burned to produce a kWh of energy. The maximum occurs close to 1600 RPM at full load (thicker boundary line). On the y -axis is the brake mean effective pressure (bmeep), a measure of an engine's capacity to do work directly related to the torque.

The working condition that maximizes the efficiency is located at A. If the engine is running in the A position and the driver needs some extra power to overtake another vehicle or simply because he encounters a steeper terrain, he would necessarily have to shift because the engine is already close to the full load line (the thicker upper boundary blue line). Even if it is less efficient the engine is more often operated closer to the B position which guarantees a better driving experience.

The above example illustrates that it is extremely important to properly design the gearing of the differentials and of the gearbox: the total gear ratio will determine the engine working point in Fig. 4.3. The choice of the right gearing can help to increase the efficiency (work as close as possible to the peak of efficiency at the given power requirement) but the total consumption is always increased if the power requirement grows (the power grows ten times while the efficiency almost doubles from the worst to the best case).

The analysis of the the efficiency of the full vehicle will be performed in this perspective; the objective will be the reduction of power required to drive the wheels. The drive-line usually has an efficiency between 0.87 and 0.93 while the axle differentials have virtually

unitary efficiency if the vehicle is proceeding on a straight line trajectory [8]. The power that the engine produces is transformed at the desired torque/angular velocity combination by the drive-line and it reaches the wheels where it is *transferred* to the ground (the efficiency of the drive-line is almost constant along the working range). A reduction of the power required by the wheels directly translates in a reduction of the power required from the engine, and consequently reduces the consumption.

4.1.2 Electric Motor

The electric motor is a unit that converts electrical energy into mechanical work. Electric engines are usually preferred on small robots and have recently been employed into hybrid vehicles where they work in cooperation with the ICE. Small robots often have an electric motor for every wheel: in this way the inefficiency of the drive-line is removed all together. This is possible because electric engines have an unique property; they can produce torque at zero angular velocity. For this reason they can be mounted directly on the wheel hub, no clutch or gear reduction is strictly necessary.

Figure 4.4 presents the engine map for a large electric motor. The efficiency of electric units can be fairly high ($> 90\%$) and like in ICE it benefits from working close to the full-load region. If the motor is attached to a drive-line, the correct choice of gear ratios can guarantee an improved fuel economy over a wide range of operating conditions (as seen for the ICE). If the motor is directly attached to the wheels only one vehicle speed will be optimized.

4.2 Aerodynamic Efficiency

The aerodynamic efficiency of a vehicle is a complex engineering problem that requires the most advanced techniques in the area of fluid dynamics. Genta [8] provides a detailed analysis of the aerodynamic forces acting on a vehicle, to be briefly summarized in this chapter. The air surrounding a vehicle moving on earth does not behave as an ideal/inviscid flow. The fluid viscosity causes the tangential forces which produce frictional drag and modify the pressure distribution along the body. Frictional drag is usually not very significant for low-viscosity

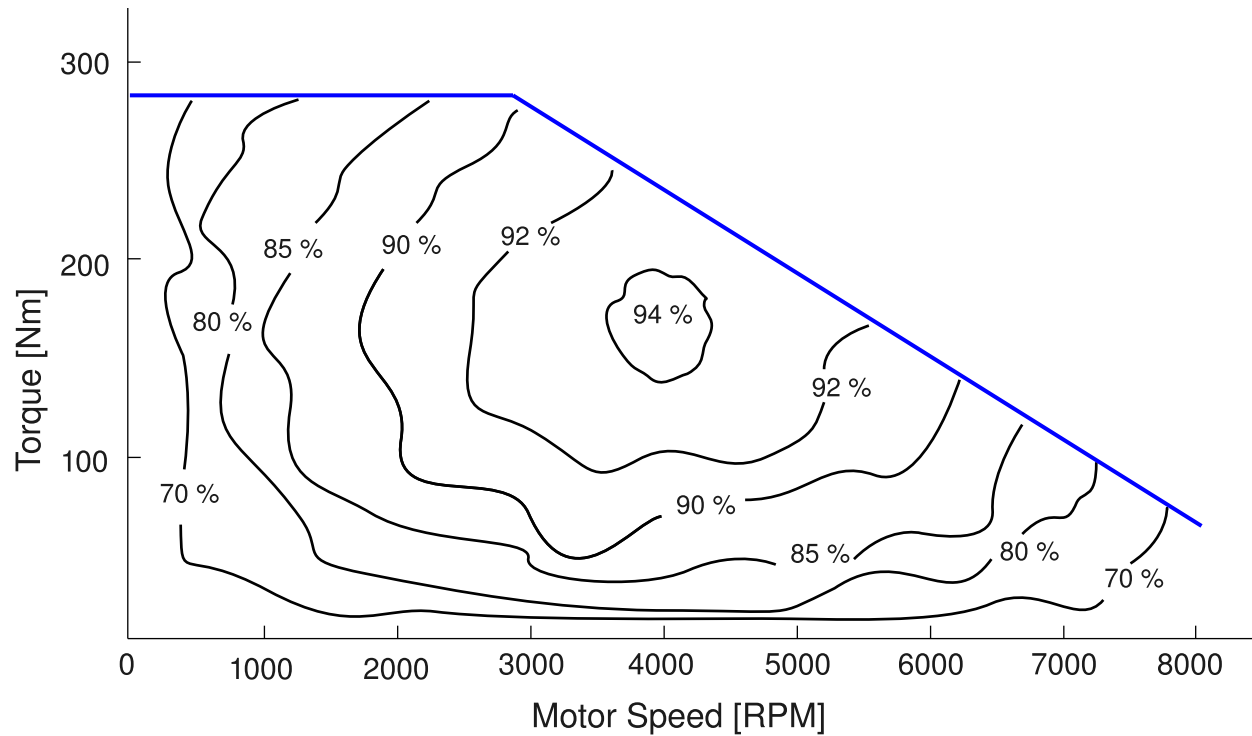


Figure 4.4: Typical efficiency map for an electric motor for hybrid vehicles applications.

fluids such as air, while the modified pressure distribution generates a lift force, a side force and a longitudinal force. The lift force and the side force will not be included in this study, while the longitudinal resistance force will be included in the full vehicle model.

The aerodynamic drag force can be decomposed in three terms:

1. friction drag,
2. induced drag,
3. shape drag.

The friction drag is due to tangential forces acting on the body and, as previously stated, does not have a significant impact when the fluid has low viscosity (almost 10% of the total aerodynamic drag can be caused by the friction drag). The induced drag is related to the energy dissipation needed for the generation of the trailing vortexes and it modestly contributes to the total drag. The shape drag is due to the field of low pressure in the wake: this represents the predominant component of the aerodynamic drag.

The total aerodynamic resistance force is expressed as:

$$F_{drag} = \frac{1}{2}\rho V^2 S C_f, \quad (4.1)$$

where:

ρ = air density,

V = longitudinal vehicle velocity,

S = vehicle frontal area,

C_f = coefficient of drag.

The coefficient of drag, usually obtained experimentally, includes the components of friction drag, induced drag, and shape drag. The aerodynamic efficiency improves for decreased values of C_f . This can be obtained with streamlined body shape, with the introduction of aerodynamic appendixes, and with the adoption of devices aimed to increase the pressure in the wake.

4.3 Tractive Efficiency

The motion resistance at the tire-soil interface is predominantly influenced by the terrain compaction that results from sinkage. A measure of the efficiency can be obtained comparing the thrust power with the driving power:

$$\eta_t = \frac{F_x v_x}{T \omega} = \frac{F_x (1 - s_d) R_l}{T}. \quad (4.2)$$

This *tractive efficiency* depends upon the slip s_d and the effective rolling radius R_l and it gives a measure of the capability to convert the power delivered to the wheels into effective mobility (the effective rolling radius is either the undeformed radius R_u for rigid wheels or $\min(R_{eff})$ for flexible tires).

Tractive efficiency can be split into two terms: efficiency of motion,

$$\eta_m = \frac{F_x R_l}{T}, \quad (4.3)$$

and efficiency of slip,

$$\eta_s = 1 - s_d. \quad (4.4)$$

The efficiency of motion is a direct measure of the ability to convert the applied torque into useful drawbar pull. The efficiency of slip measures the losses due to slip effect. For a four wheel drive vehicle, assuming same performance of the two front and rear tires, it is possible to express the slip efficiency as follows [18]:

$$\eta_s = 1 - \frac{s_{df} u_f F_f + s_{dr} u_r F_r}{u_f F_f + u_r F_r}. \quad (4.5)$$

where the indexes f and r refer to the front and rear axle respectively. Introducing the ratio of theoretical speed,

$$K_v = \frac{u_f}{u_r} = \frac{1 - s_{dr}}{1 - s_{df}}, \quad (4.6)$$

and the coefficient of thrust distribution,

$$K_d = \frac{F_r}{F_f + F_r}, \quad (4.7)$$

and through some mathematical manipulations it is possible to express the slip efficiency for a four wheel drive vehicle as follows:

$$\eta_s = 1 - \frac{s_{df}(1 - s_{dr}) - (s_{df} - s_{dr})K_d}{(1 - s_{dr}) - (s_{df} - s_{dr})K_d}. \quad (4.8)$$

Setting the first partial derivative of (4.8) with respect to K_d equal to zero it is possible to find the optimal slip distribution:

$$\frac{\partial \eta_s}{\partial K_d} = \frac{(1 - s_{df})(1 - s_{dr})(s_{df} - s_{dr})}{[(1 - s_{dr}) - (s_{df} - s_{dr})K_d]^2} = 0 \quad (4.9)$$

Equation (4.9) is satisfied when s_{df} and s_{dr} are both equal to 1 (100% slip) and when $s_{sd} = s_{dr}$. Clearly the first possibility corresponds to zero efficiency because if both axles have

100% of slip the vehicle cannot move. The slip efficiency is maximized when the slip difference between the front and the rear axle is minimized. More results regarding a full vehicle will be presented in Chapter 5. In this section the performance of a single tire is investigated. Traction efficiency for dry sand is presented in Figure 4.5. These plots regard rigid wheels since tires behave rigidly on dry sand. Larger and wider tires, decreasing the sinkage, have a beneficial impact on the efficiency. Also the multi-pass effect enhances the efficiency. This is expected because firmer soil reduces the sinkage and provides better traction. The increase of vertical load (due to increased vehicle weight or load transfer phenomena during motion) has a marginal negative effect: higher values of F_z enhance the tractive performance but at the same time increase the sinkage and deteriorate the efficiency.

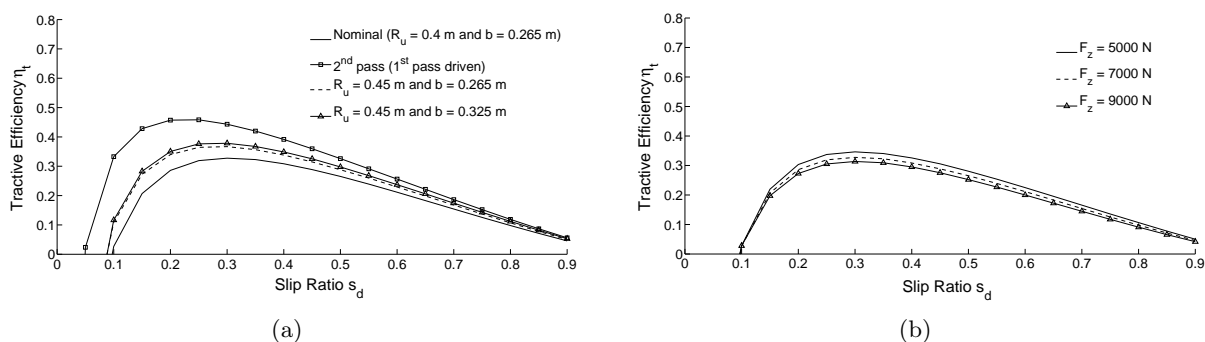


Figure 4.5: Tractive efficiency under different operational scenarios for a tire rolling on dry sand. In (a) different sizes and the multi-pass effect influence is showed. In (b) different loads are investigated.

Figure 4.6 presents the tractive efficiency for tires rolling on loam terrain. The efficiency increases for larger tires, lower inflation pressure and successive pass traveling on firmer soil. This happens because in these conditions the sinkage decreases leading to a reduced resistance compaction force. During on-road operations higher inflation pressure guarantees better fuel economy but this is not the case in off-road. Reduced inflation pressure not only improves the traction but it also reduces the sinkage, which also improves the efficiency (the hysteresis losses are negligible if compared with the terrain compaction resistance). The increase in vertical load has a stronger impact than that showed by dry sand. This is due to the fact that loam is a firmer soil and the compaction resistance due to sinkage is more significant.

The efficiency, for both soils, has a peak in the range of 10-20% slip. It should be remembered that it is not possible to force the tires to work at an imposed slip ratio (the

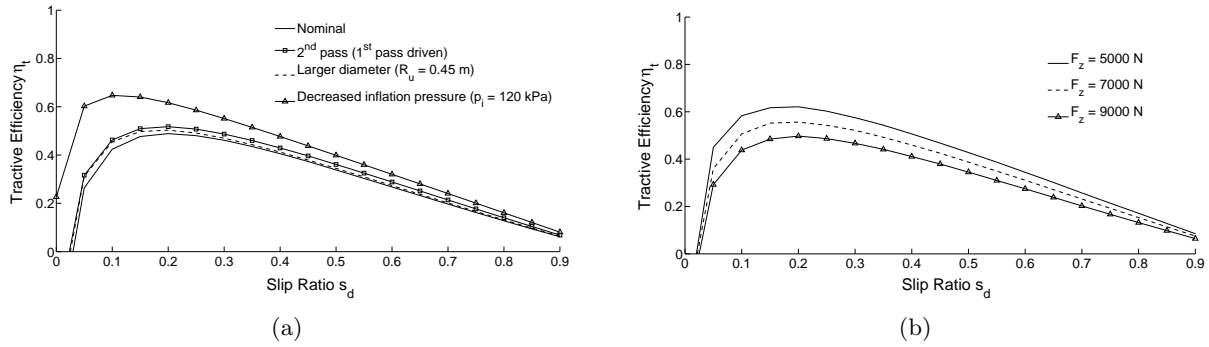


Figure 4.6: Tractive efficiency under different operational scenarios for a tire rolling on moist Yolo loam. In (a) different inflation pressures, tire sizes, and the multi-pass effect influence is showed. In (b) different loads are investigated.

slip is indirectly controlled by the driver through the control of the desired vehicle speed). What can be done is to properly match the tires, the power-train ratio and the torque distribution in order to optimize the motion in specific working conditions. This will be addressed in Chapter 5.

Chapter 5

Vehicle Model Development

In this chapter a full vehicle model is developed. In first two sections the mathematical model will be described and validated. In the results' section the efficiency of some standard driving scenarios will be analyzed and discussed.

5.1 Mathematical Model

The model described below is intended to highlight the salient features of vehicle dynamics in order to realistically simulate vehicle motion on soft terrain.

Before starting with the description of the model some basic terminology needs to be reviewed. In the automotive field the mass of the vehicle body (including the frame) is usually referred as the sprung or suspended mass. On the other hand, the mass of the wheels and moving suspension parts are called unsprung masses.

The vehicle model includes:

- the off-road tire model presented in Chapter 3,
- the sprung mass inertial properties,
- independent suspension,
- Ackermann steering geometry,

- aerodynamic drag resistance in the longitudinal direction,
- drive-train kinematics(engine, transmission, differential).

However, to limit the complexity of the simulation some simplifications are introduced:

- vehicle body flexibility is not considered,
- the steering mechanism is modeled only in its kinematics,
- the inertia properties of the drive-line are not considered,
- no camber or toe angle is considered,
- suspensions' kinematics is linear.

Next sections will discuss in details the development of the model, its validation, and the results of several case studies.

5.1.1 Equations of Motion

The vehicle model is based on the analysis discussed in [8, 79, 80, 50]. Figure 5.1 presents the vehicle model scheme. Five masses are considered:

- the vehicle sprung mass m_s , concentrated at the center of gravity of the body,
- four unsprung masses m_u located at the center of the wheel hubs. These masses account for the rims, the tires, and suspension assemblies.

Three reference frames are defined following the recommendations of SAE J670e [3]:

- the inertial reference frame X, Y, Z : a right-handed earth-fixed coordinate system
- the vehicle reference frame x, y, z : a right-handed vehicle-fixed coordinate system attached to the sprung mass. The origin is located at the center of gravity (CG) of the sprung mass.

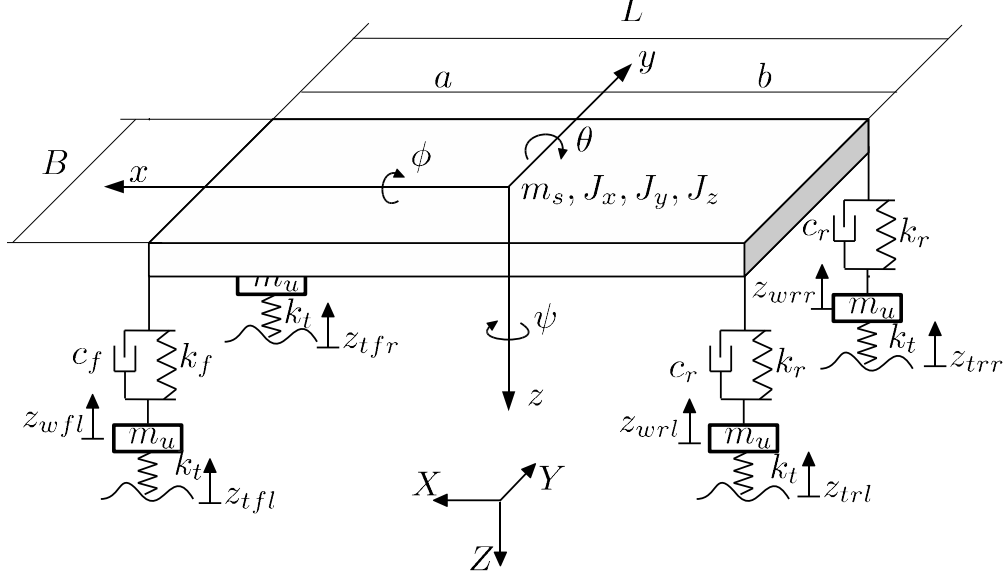


Figure 5.1: Schematic representation of the vehicle model. The earth-fixed reference frame X, Y, Z is showed and can be arbitrarily located. The vehicle motion is described in terms of the right-handed reference frame x, y, z attached to the vehicle center of gravity. The wheels displacement is constrained in the z -direction of the vehicle-fixed reference frame. To keep the plot clear the x', y', z' frame is illustrated in more detail in Figure 5.2.

- the tire reference frame x', y', z' : four right-handed tire-fixed coordinate systems attached to the unsprung masses. The z' -direction is always parallel to the vehicle-fixed z -direction. Directions x' and y' are parallel to x and y only for the rear wheels (which are not steered). The suffixes fl, fr, rl, rr will be used to refer respectively to: front-left, front-right, rear-left and rear-right (intended for an observer that is sitting in the car, facing the positive direction of the x -axis in the vehicle-fixed reference frame).

The sprung mass is modeled as a 6 degree of freedom (DOF) rigid body.

The wheels are connected to the vehicle body via springs and dampers. No relative motion in the x and y directions between the wheels and the car body is assumed. The tire displacement is constrained in the z vehicle-fixed direction only. However, the wheels have an extra degree of freedom represented by the angular velocity.

The non-linear and unsteady sprung mass motion can be described by the Newton-Euler equations, written with respect to the vehicle-fixed reference frame. This choice guarantees a straight forward calculation of the external forces acting on the body. The equations of

motion can be written as follow [79]:

$$\begin{aligned}
\sum F_x &= ms(\dot{u} + wq - vr) \\
\sum F_y &= ms(\dot{v} + ur - wp) \\
\sum F_z &= ms(\dot{w} + vp - uq) \\
\sum M_x &= \dot{L}_x + qL_z - rL_y \\
\sum M_y &= \dot{L}_y + rL_x - pL_z \\
\sum M_z &= \dot{L}_z + pL_y - qL_x,
\end{aligned} \tag{5.1}$$

where:

u, v, w = vehicle-fixed components of the sprung mass linear velocity,

p, q, r = vehicle-fixed components of the sprung mass angular velocity,

F_x, F_y, F_z = vehicle-fixed components of external and internal forces,

M_x, M_y, M_z = vehicle-fixed components of external and internal moments,

L_x, L_y, L_z = vehicle-fixed components of angular momentum.

The unsprung masses are modeled with a quarter car model. As previously stated the motion of the wheels is constrained to the z -direction in the vehicle-fixed reference frame. The dynamics of the unsprung masses can be modeled as follow:

$$\begin{aligned}
m_u \ddot{z}'_{fl} &= F_{sfl} + k_t(z'_{tfl} - z'_{fl}) \\
m_u \ddot{z}'_{fr} &= F_{sfr} + k_t(z'_{tfr} - z'_{fr}) \\
m_u \ddot{z}'_{rl} &= F_{srl} + k_t(z'_{trl} - z'_{rl}) \\
m_u \ddot{z}'_{rr} &= F_{srr} + k_t(z'_{trr} - z'_{rr}),
\end{aligned} \tag{5.2}$$

where:

$z'_{fl}, z'_{fr}, z'_{rl}, z'_{rr}$ = tires vertical displacement,

$F_{sfl}, F_{sfr}, F_{srl}, F_{srr}$ = suspension forces which will be discussed in the internal forces section 5.1.3,

k_t = tire stiffness,

$z'_{tfl}, z'_{tfr}, z'_{trl}, z'_{trr}$ = terrain vertical displacement.

The calculation of the roll, pitch, and yaw angles (Euler angles) requires the integration of the angular velocity components p, q, r through the kinematic differential equation (5.3). It should be recalled that direct integration of the angular velocity components yields erroneous results. The correct approach integrates the angular velocity components along the axes of rotation of the Euler angles. In this study the order of rotations chosen is yaw, pitch, roll:

$$\begin{aligned}\dot{\phi} &= p + (q \sin \phi + r \cos \phi) \tan \theta \\ \dot{\theta} &= q \cos \phi - r \sin \phi \\ \dot{\psi} &= (q \sin \phi + r \cos \phi) \sec \theta\end{aligned}\tag{5.3}$$

The presence of $\tan \theta$ and $\sec \theta$ introduces a singularity when the pitch angle equals $\frac{\pi}{2}$. This problem can be avoided with introducing the quaternions or an indexing scheme. However, no countermeasure is taken because the pitch angle will remain small during motion.

The external forces acting on the vehicle are:

- forces and moments generated at the tire-terrain contact patches,
- aerodynamic force (only in the x -direction),
- gravitational force,

The internal forces are:

- forces produced by the springs compression/extension,
- forces produced by the dampers compression/extension.

5.1.2 External Forces

Tire Forces

The torque generated by the engine *flows* into the transmission and the differentials and reaches the tires where it is *transferred* to the ground via the contact patch-terrain interaction. The vehicle considered in this study has steering capabilities only at the front axle, as shown in Figure 5.2.

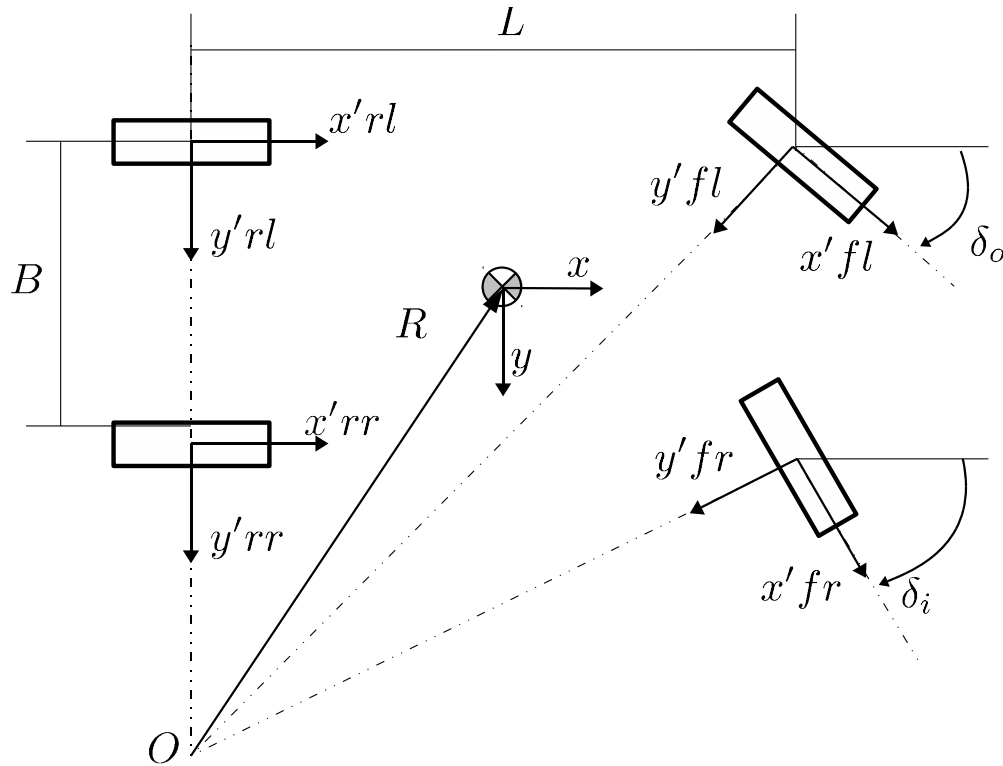


Figure 5.2: Top-view of a vehicle during a right turn. The wheels reference frames x', y', z' are highlighted and the Ackermann steering geometry is presented.

When the vehicle is turning the inner and outer wheels follow circles of different radii. To avoid slip phenomenon the left and right wheels have to be steered by a different angle. This condition is called Ackermann steering geometry and is expressed by:

$$\cot \delta_o - \cot \delta_i = \frac{B}{L}, \quad (5.4)$$

where:

δ_o = steering angle of the outer wheel,

δ_i = steering angle of the inner wheel,

B = vehicle track,

L = vehicle wheel base (see Figure 5.2).

The tire forces are calculated in the reference frame attached to the wheels. For the rear tires the wheel coordinate system is parallel (in all three directions) to the vehicle-fixed reference frame. The front tire-reference frame is rotated around the z -axis by the angle δ (see Figure 5.2).

The forces generated by the tires can be summarized as follow:

$$\begin{aligned} F_{xt} &= F_{x'fl} \cos(\delta_l) - F_{y'fl} \sin(\delta_l) + F_{x'fr} \cos(\delta_r) - F_{y'fr} \sin(\delta_r) + F_{xrl} + F_{xrr} \\ F_{yt} &= F_{x'fl} \sin(\delta_l) - F_{y'fl} \cos(\delta_l) + F_{x'fr} \sin(\delta_r) - F_{y'fr} \cos(\delta_r) - F_{y'rl} - F_{y'rr}, \end{aligned} \quad (5.5)$$

where

F_{xt} = force in the x direction of the vehicle-fixed reference frame generated by the tires

F_{yt} = force in the y direction of the vehicle-fixed reference frame generated by the tires

The steering angles δ_l and δ_r are defined according to (5.4), depending on whether the vehicle is turning left or right.

Tire forces also generate moments that can be calculated as follows:

$$\begin{aligned}
M_{xt} &= + (F_{x'fl} \sin(\delta_l) + F_{y'fl} \cos(\delta_l)) \left(z - \frac{B}{2}\phi - a\theta - z'_{fl} \right) \\
&\quad + (F_{x'fr} \sin(\delta_r) + F_{y'fr} \cos(\delta_r)) \left(z + \frac{B}{2}\phi - a\theta - z'_{fr} \right) \\
&\quad + F_{y'rl} \left(z - \frac{B}{2}\phi + b\theta - z'_{rl} \right) \\
&\quad + F_{y'rr} \left(z + \frac{B}{2}\phi + b\theta - z'_{rr} \right) \\
M_{yt} &= + (F_{x'fl} \cos(\delta_l) - F_{y'fl} \sin(\delta_l)) \left(z - \frac{B}{2}\phi - a\theta - z'_{fl} \right) \\
&\quad + (F_{x'fr} \cos(\delta_r) - F_{y'fr} \sin(\delta_r)) \left(z + \frac{B}{2}\phi - a\theta - z'_{fr} \right) \\
&\quad + F_{x'rl} \left(z - \frac{B}{2}\phi + b\theta - z'_{rl} \right) \\
&\quad + F_{x'rr} \left(z + \frac{B}{2}\phi + b\theta - z'_{rr} \right) \\
M_{zt} &= -F_{x'fl} \sin(\delta_l)a + F_{x'fl} \cos(\delta_l)\frac{B}{2} - F_{y'fl} \cos(\delta_l)a - F_{y'fl} \sin(\delta_l)\frac{B}{2} \\
&\quad - F_{x'fr} \sin(\delta_r)a - F_{x'fr} \cos(\delta_r)\frac{B}{2} - F_{y'fr} \cos(\delta_r)a + F_{y'fr} \sin(\delta_r)\frac{B}{2} \\
&\quad + F_{x'rl}\frac{B}{2} + F_{y'rl}b - F_{x'rr}\frac{B}{2} + F_{y'rr}b,
\end{aligned} \tag{5.6}$$

where:

M_{xt} = roll moment the x -direction of the vehicle-fixed reference frame generated by the tires,

M_{yt} = pitch moment the y -direction of the vehicle-fixed reference frame generated by the tires,

M_{zt} = yaw moment the z -direction of the vehicle-fixed reference frame generated by the tires.

Equations (5.5) and (5.6) contribute to the external forces acting on the sprung mass.

Aerodynamic Forces

The aerodynamic drag has been discussed in Section 4.2. The effect of air resistance is included in the model as a force acting in x -direction of the vehicle-fixed reference frame. Lateral and vertical forces due to aerodynamic effects are not considered. It is assumed that the aerodynamic drag force is applied at the CG of the vehicle, therefore no moments are generated. The drag is modeled with the following equation:

$$F_{xd} = \frac{1}{2} \rho S_c u^2, \quad (5.7)$$

where:

ρ = air density,

S_c = drag area (includes the vehicle frontal area and the coefficient of drag C_f),

u = velocity in the x -direction of the vehicle-fixed reference frame.

Gravitational Forces

The gravitational force is included into the model as an external force. A vector normal to the terrain profile is defined as follows:

$$\vec{n}_t = \begin{bmatrix} \sin(\theta_t) \cos(\phi_t) \\ -\sin(\phi_t) \\ \cos(\theta_t) \cos(\phi_t) \end{bmatrix} \quad (5.8)$$

where:

ϕ_t = terrain profile inclination in the x -direction of the vehicle-fixed reference frame,

θ_t = terrain profile inclination in the y -direction of the vehicle-fixed reference frame,

Hence, the gravitational forces acting on the vehicle can be written as a function of the terrain normal vector. \vec{n}_t :

$$\begin{bmatrix} F_{xg} \\ F_{yg} \\ F_{zg} \end{bmatrix} = \vec{n}_t \cdot g(m_s + 4m_u), \quad (5.9)$$

where:

F_{xg} = force in the x -direction of the vehicle-fixed reference frame generated by the gravity,

F_{yg} = force in the y -direction of the vehicle-fixed reference frame generated by the gravity,

F_{zg} = force in the z -direction of the vehicle-fixed reference frame generated by the gravity,

g = gravity acceleration.

Equation (5.9) defines the forces due to gravity that act on the sprung mass. It should be noted that the terrain inclination angles ϕ_t and θ_t , may have to be calculated as an average of the inclination of the terrain in contact with each wheel. However, in this study only constant terrain inclination will be considered leading to $\theta_t = 0$ and $\phi_t = const$.

5.1.3 Internal Forces

The internal forces are the forces exchanged between the sprung mass and the unsprung masses through the suspension system. Suspension forces are modeled as follow:

$$\begin{aligned} F_{sfl} &= c_f \left(w - \frac{B}{2}p - aq - \dot{z}'_{fl} \right) + k_f \left(z - \frac{B}{2} \sin(\phi) - a \sin(\theta) - z'_{fl} \right) \\ F_{sfr} &= c_f \left(w + \frac{B}{2}p - aq - \dot{z}'_{fr} \right) + k_f \left(z + \frac{B}{2} \sin(\phi) - a \sin(\theta) - z'_{fr} \right) \\ F_{srl} &= c_r \left(w - \frac{B}{2}p + bq - \dot{z}'_{rl} \right) + k_r \left(z - \frac{B}{2} \sin(\phi) + b \sin(\theta) - z'_{rl} \right) \\ F_{srr} &= c_r \left(w + \frac{B}{2}p + bq - \dot{z}'_{rr} \right) + k_r \left(z + \frac{B}{2} \sin(\phi) + b \sin(\theta) - z'_{rr} \right) \end{aligned} \quad (5.10)$$

where:

F_{sfl} = is force in the front-left suspension,

F_{sfr} = is force in the front-right suspension,

F_{srl} = is force in the rear-left suspension,

F_{srr} = is force in the rear-right suspension,

c_f = is the damping coefficient of the front suspensions,

c_r = is the damping coefficient of the rear suspensions,

k_f = is the stiffness coefficient of the front suspensions,

k_r = is the stiffness coefficient of the rear suspensions.

Since the unsprung masses are constrained to move in the z -direction of the the vehicle-fixed reference frame, the assumption that all the suspension forces act in the vehicle-fixed z -direction is made. The suspension forces, being internal forces, act on the unsprung mass (5.2) and contribute to the term F_z in the equations of motion of the sprung mass (5.1).

5.1.4 Tire Forces Generation Process

The development of the tire model (Chapter 3) showed that three parameters control the behavior of a given tire (this assumes that the inflation pressure, the tire geometry and the tire properties are fixed):

F_{zw} = vertical load acting on the wheel (generically labeled as F_z in Chapter 3),

s_d = slip ratio,

α_c = slip angle.

From the vehicle dynamics point of view the perspective is slightly different. The lateral dynamics of the tires is governed by the steering action imposed by the driver and by the

dynamics of the vehicle. The longitudinal dynamics of the tires is governed by the torque applied to the axle (decided again by the driver through the gas pedal). The amount of slip is not known *a priori* but depends on the amount of torque imposed by the engine. The process is described in Figure 5.3.

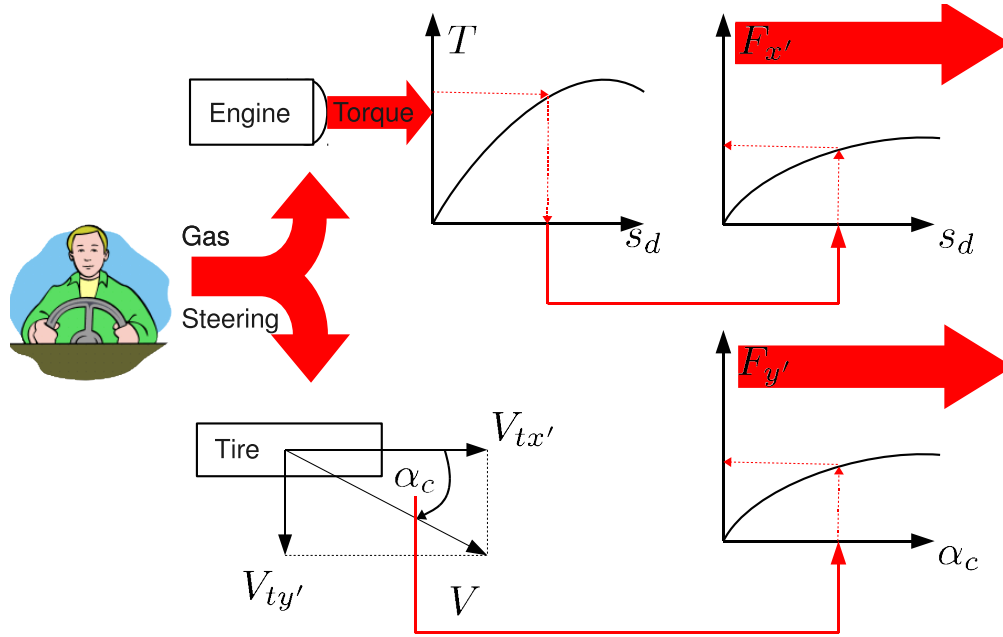


Figure 5.3: A schematic representation of how the driver input is translated into actual driving forces at the wheels.

Once the slip ratio is known it is possible to calculate the angular velocity of each wheel from the definition of the slip (2.1),

$$\omega_w = \frac{u}{R_l(1 - s_d)}, \quad (5.11)$$

where R_l is the rolling radius and it is equal to R_u (undeformed radius) for rigid wheels and $R_u - \frac{F_{zw}}{k_t}$ for flexible tires. The calculation of the angular velocity of the wheels is necessary to estimate the instantaneous power delivered to the wheels.

The above discussion showed that for the calculation of the lateral and longitudinal forces it is necessary to calculate the vertical load and the slip angle at each wheel first. The vertical load can be evaluated from the following equations:

$$\begin{aligned}
F_{zwfl} &= F_{zg} \frac{b}{4L} + F_{sfl} \\
F_{zwfr} &= F_{zg} \frac{b}{4L} + F_{sfr} \\
F_{zwrl} &= F_{zg} \frac{a}{4L} + F_{srl} \\
F_{zwrr} &= F_{zg} \frac{a}{4L} + F_{srr},
\end{aligned} \tag{5.12}$$

This formulation assumes no lateral inclination of the road profile (i.e., $\theta_t = 0$). Equations (5.12) are calculated at every time step and fed to the tire model.

The slip angle is defined as follows:

$$\alpha_c = \tan^{-1} \left(\frac{V_{ty}}{V_{tx}} \right), \tag{5.13}$$

where:

$V_{tx'}$ = velocity in the x' -direction of the tire-fixed reference frame,

$V_{ty'}$ = velocity in the y' -direction of the tire-fixed reference frame,

Assuming small pitch and roll angles, for the rigid body motion, the slip angles can be calculated as follows:

$$\begin{aligned}
\alpha_{cfl} &= \tan^{-1} \left(\frac{v + a\dot{\psi}}{u + \frac{B}{2}\dot{\psi}} \right) - \delta_l \\
\alpha_{cfr} &= \tan^{-1} \left(\frac{v + a\dot{\psi}}{u - \frac{B}{2}\dot{\psi}} \right) - \delta_r \\
\alpha_{crl} &= \tan^{-1} \left(\frac{v - b\dot{\psi}}{u + \frac{B}{2}\dot{\psi}} \right) \\
\alpha_{crr} &= \tan^{-1} \left(\frac{v - b\dot{\psi}}{u - \frac{B}{2}\dot{\psi}} \right),
\end{aligned} \tag{5.14}$$

the front slip angles have to keep into account the steering angles δ , while the rear slip angles can be directly calculated from the velocities of the *corners* of the vehicle.

5.1.5 Velocity Controller

A proportional integral (PI) controller is introduced to maintain the imposed cruise speed. The error function ϵ depends on the difference between the target velocity V_{set} and the longitudinal velocity u :

$$\epsilon(t) = V_{set} - u(t), \quad (5.15)$$

where the notation explicitly includes the time dependence. The controller acts on the torque delivered to the wheels through the following equation:

$$T(t) = K_p \epsilon(t) + K_i \int_0^t \epsilon(\tau) d\tau \quad (5.16)$$

where:

K_p = proportional gain,

K_i = integral gain.

5.1.6 Torque Distribution

For front (rear) wheel drive vehicles the torque is equally divided on the left and right wheels of the axle, in this case no torque is delivered to the rear (front) axle. The non driven wheels will receive zero torque but will produce a negative force because of the terrain compaction resistance that still acts on them.

In the case of four wheel drive vehicles the torque will be distributed equally among the left and right wheels (the axle differentials always slip the torque equally). On the other hand, the torque distribution among the front and rear axles (governed by the central differential) will be varied.

5.1.7 Vehicle Parameters

The vehicle parameters adopted in the simulations which follow represent typical values for a large SUV and have been summarized in Table 5.1.

Table 5.1: Vehicle specifications.

$m_s = 2500$ kg	$m_u = 44$ kg
$J_x = 1165$ kgm ²	$c_f = 2700$ Ns/m
$J_y = 5348$ kgm ²	$c_r = 3300$ Ns/m
$J_z = 5721$ kgm ²	$k_f = 25$ kN/m
$a = 1.48$ m	$k_r = 21$ kN/m
$b = 1.52$ m	$\rho = 1.28$ kg/m ³
$L = 3$ m	$S_c = 2.44$ m ²
$B = 1.7$ m	$k_t = 270395$ kN/m

5.2 Vehicle Model Validation

The dynamic response of the vehicle model has been validated performing two standard maneuvers:

- Acceleration and braking on a straight-line trajectory,
- Double lane change at constant velocity.

The results have been compared with *CarSim*®[®], a software for high-fidelity vehicle dynamics simulation. CarSim has been initialized in order to match closely the assumptions done in this study:

- vehicle properties have been taken from Table 5.1,
- simple independent suspensions have been selected,
- zero toe and camber angle,
- linear springs and dampers,
- aerodynamic forces only in the the x vehicle-fixed direction.

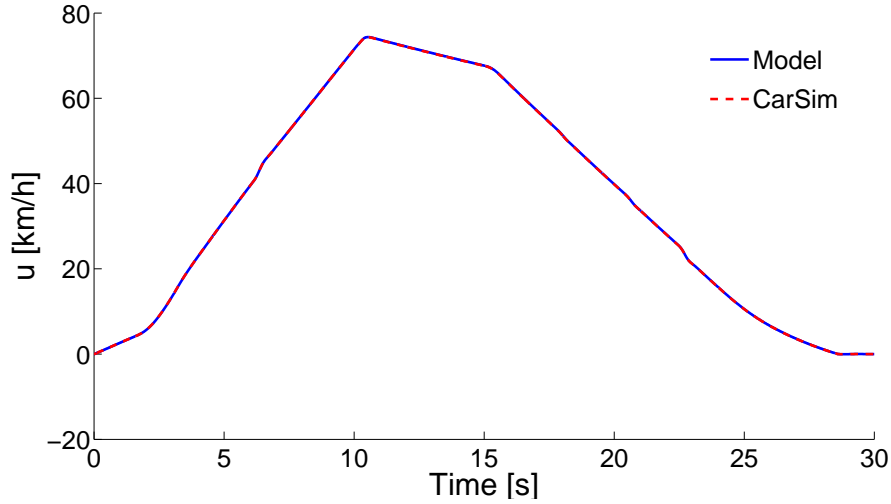


Figure 5.4: Longitudinal velocity of the vehicle during an acceleration and braking maneuver.

For this validation process the on-road tire model, built-in CarSim, has been adopted. This was the only option since no off-road tire model is implemented in CarSim. The aim of the validation is to verify that the model predicts correctly the dynamics of the vehicle: in particular it is important to estimate the weight transfer among the axle because the vertical load distribution influences the behavior of the tires. In the next sections the model developed in this thesis will be addressed simply as *model* while the results obtained from CarSim will be labeled as *CarSim*.

5.2.1 Acceleration and Braking

The first test consists in a straight-line acceleration and then braking maneuver. Since the model does not include a gearbox model (needed during an acceleration from rest up to 80k/h) the longitudinal component of tire forces has been directly fed from CarSim into the model: the variables labeled F_{x_L1} , F_{x_R1} , F_{x_L2} , F_{x_R2} , extracted from the CarSim workspace, have been equaled to $F_{x'_{fl}}$, $F_{x'_{fr}}$, $F_{x'_{rl}}$, $F_{x'_{rr}}$. Figure 5.4 shows the profile of the longitudinal velocity during the 30 second test. A perfect agreement is found between the model and CarSim.

Figure 5.5 presents the trend of the pitch angle θ . The car pitches up during the acceleration (negative pitch in the body-fixed reference frame) and down during the braking

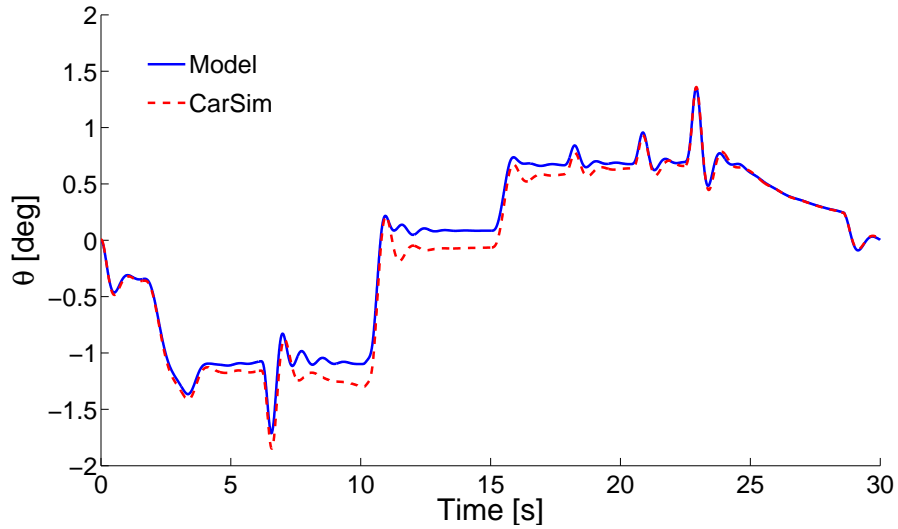


Figure 5.5: Pitch angle of the vehicle during an acceleration and braking maneuver.

section. The peaks in the graph are due to the shifting process during which a short transient occurs. Excellent agreement holds between the model and CarSim.

The variation of vertical load during the motion is showed in Figure 5.6.

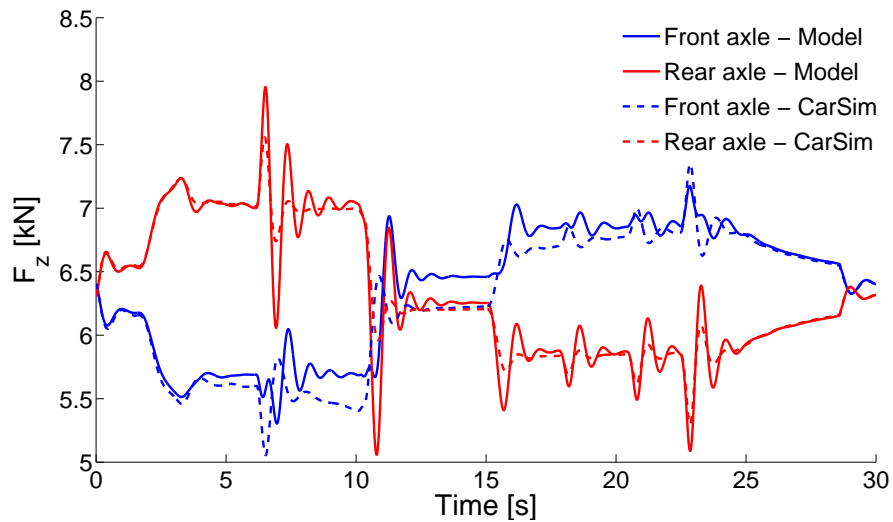


Figure 5.6: Pitch angle of the vehicle during an acceleration and braking maneuver.

During the acceleration the load is *transferred* to the rear axle, while the front axle is more loaded during the braking. As for the pitch also the load distribution is influenced by the shifting process. The agreement between the model and CarSim is good: it is noticed that the CarSim response is more dampened. This might be due to an extra damping coefficient

that has not been considered in the model.

5.2.2 Double Lane Change

The double lane change is the typical maneuver that a driver performs while passing another vehicle on the highway. The trajectory followed, at constant longitudinal velocity, by the vehicle is showed in Figure 5.7. For this test the CarSim workspace variables $Steer_L1$ and $Steer_R1$ have been passed to the the model as the steering angles δ_l and δ_r . The longitudinal velocity has been kept constant with the controller introduced by (5.16).

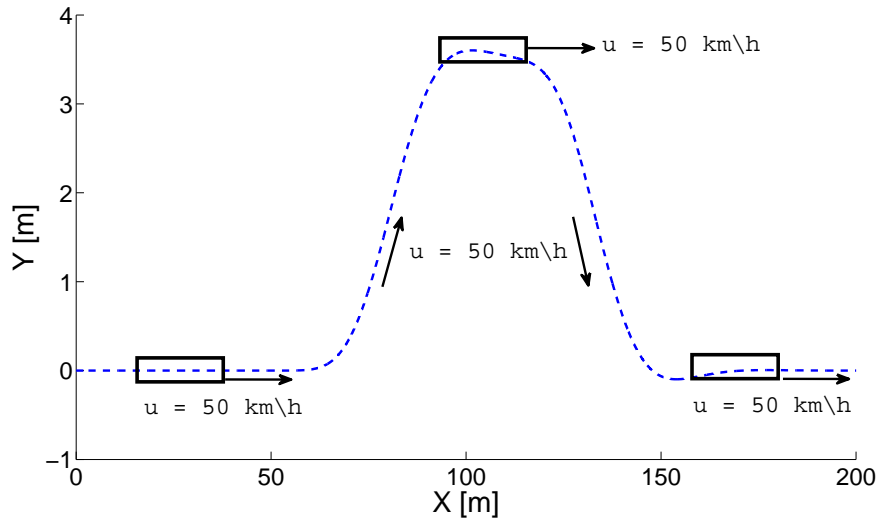


Figure 5.7: Trajectory followed by the vehicle during a double lane change maneuver.

Figure 5.8 shows the longitudinal velocity during 15 second. The response is slightly different because of the intrinsic differences between the model and CarSim. CarSim includes the compliance of the drive-line while the controller introduced in this thesis acts directly on the torque. The slight variation of longitudinal velocity occurs because of the coupling terms seen in (5.1). When the vehicle starts to steer a slip angle develops at the each corner (not only at the steered wheels) and the lateral force develops. The variation of the lateral velocity creates an unbalance in the longitudinal velocity that consequently needs to be adjusted. The trend of u reflects the the trend of the roll angle ϕ ; both variations are primarily caused by the variation of lateral velocity.

The roll angle ϕ is presented in Figure 5.9. The vehicle rolls significantly during the

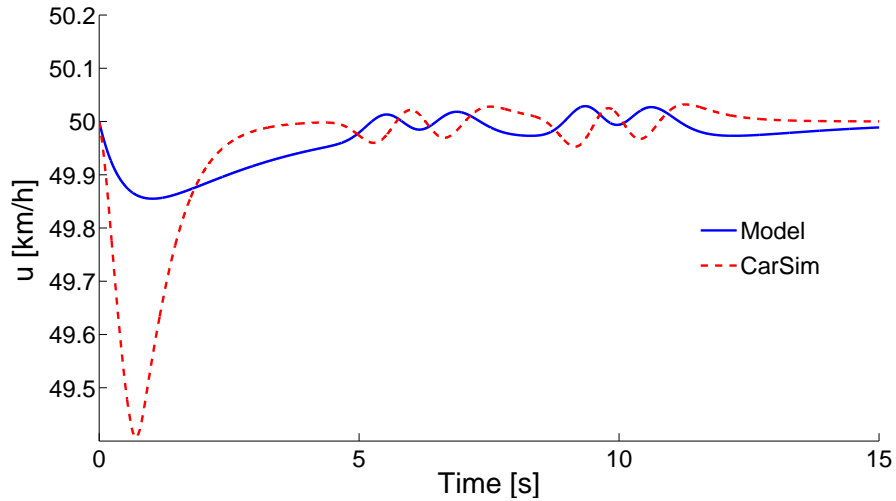


Figure 5.8: Vehicle longitudinal velocity during a double lane change maneuver.

maneuver and a fairly good agreement is found between the model and CarSim. Off-road vehicles have usually *soft* suspensions and high CG: two conditions that favor lateral weight transfer phenomena and increase the rollover risk.

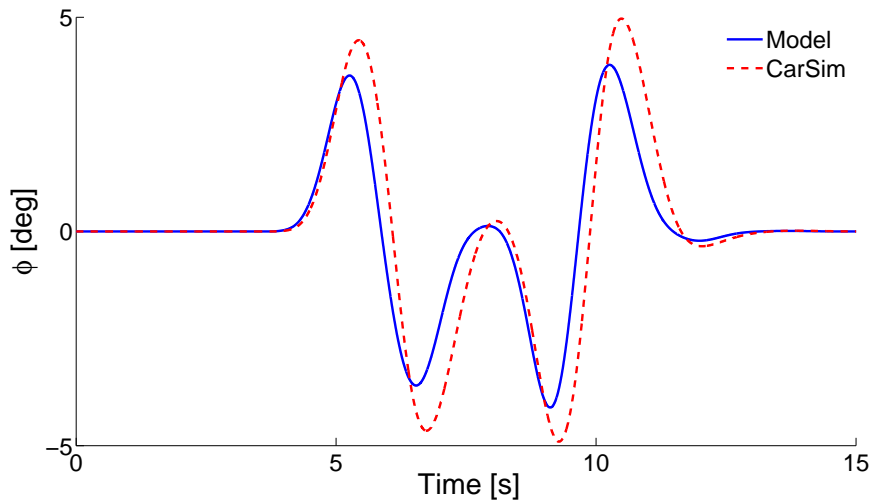


Figure 5.9: Vehicle roll angle during a double lane change maneuver.

Figure 5.10 shows the vehicle pitch angle. The model predicts the trend but it looks off with respect to CarSim data. However, it should be noted that during constant velocity tests the pitch remains small, the scale of Figure 5.10 is in fact exaggerated. In this perspective, the difference between the model and CarSim is comparable to what is presented in Figure 5.5.

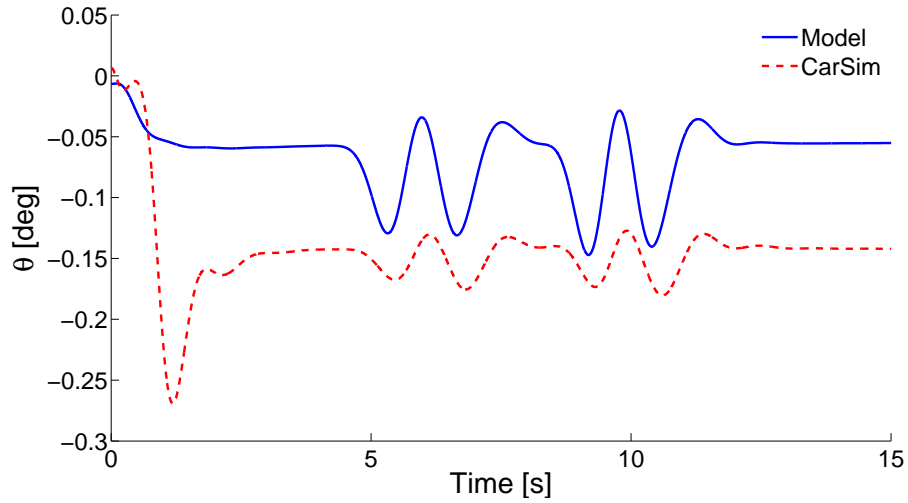


Figure 5.10: Vehicle pitch angle during a double lane change maneuver.

The vehicle yaw ψ is shown in Figure 5.11. The model estimates accurately the yaw, the result is reasonably comparable with CarSim.

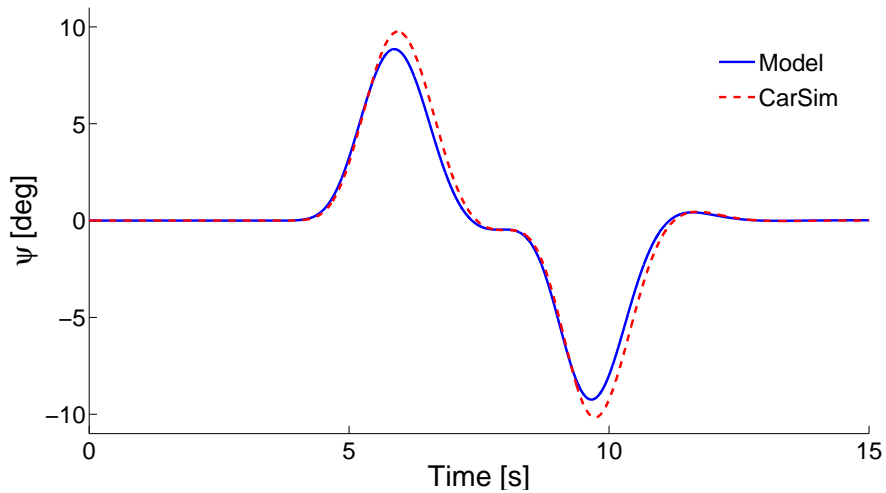


Figure 5.11: Vehicle yaw angle during a double lane change maneuver.

The last Figure 5.12 of this section shows the vertical load distribution acting on the wheels. During cornering the outer wheels are more loaded than the inner ones. This phenomenon is correctly estimated by the model: the results are in fairly good agreement with CarSim as well.

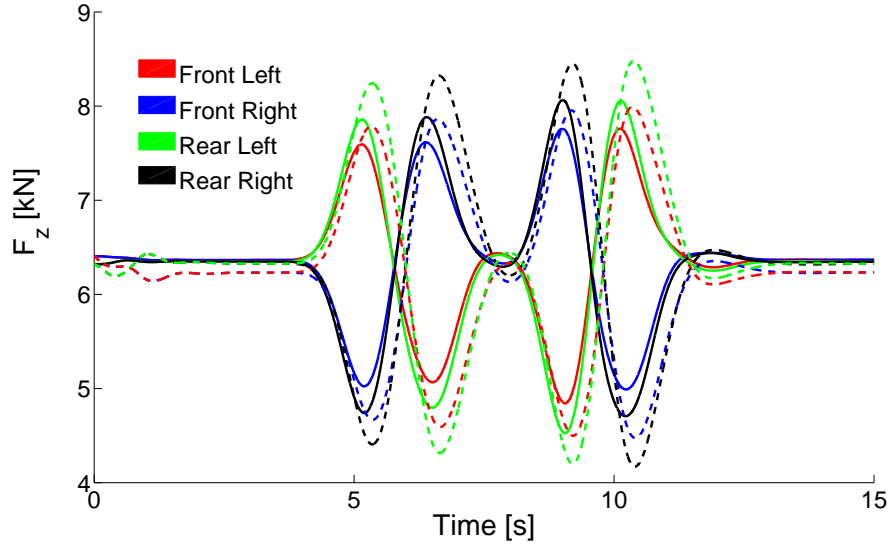


Figure 5.12: Vertical load distribution during a double lane change maneuver. Solid lines: Model. Dashed lines: CarSim. The vertical load increases on the outer wheels and decreases on the inner ones due to dynamic weight transfer phenomenon.

5.3 Results

Hitherto, the tire model and the vehicle model have been developed and explained distinctly. In this section the results for a full-vehicle, and adopting the tire model developed in Chapter 3, are presented. Since the tire model has been developed under steady state assumptions, the full-vehicle simulation is performed at constant longitudinal speed. The simulations are started at a velocity slightly lower than the target one, and the PI controller (5.16) is used to reach smoothly the cruise speed. The efficiency is analyzed when steady state conditions are reached. The transients have to be regarded as a first approximation of the vehicle dynamics.

The results are divided into four sections:

- Longitudinal motion on dry sand.
- Longitudinal motion on moist Yolo loam.
- Lateral motion on dry sand.
- Lateral motion on moist Yolo loam.

The full-vehicle model can be exploited to simulate several different maneuvers. The

influence of the vehicle and the tire-terrain parameters (Tables 5.1, 3.1, 3.2) can be investigated. For every run large amount of output data is produced and it is unpractical to present all the results here. The author decided to investigate a restricted set of parameters: details will be provided in the following sections.

5.3.1 Dry Sand Longitudinal

In this section the motion and the efficiency of a vehicle traveling on a straight line on dry sand are analyzed. The sand is a non cohesive soil and the tire will always perform as a rigid wheel in this section.

Flat Terrain

Figure 5.13 shows the velocity profile and the applied torque, for a vehicle that starts at 20 km/h and has to reach the target speed of 25 km/h. FWD, RWD and AWD configurations are plotted together: in every configuration the vehicle is able to reach the imposed speed. The PI controller adjusts the torque correctly in order to reach the target speed.

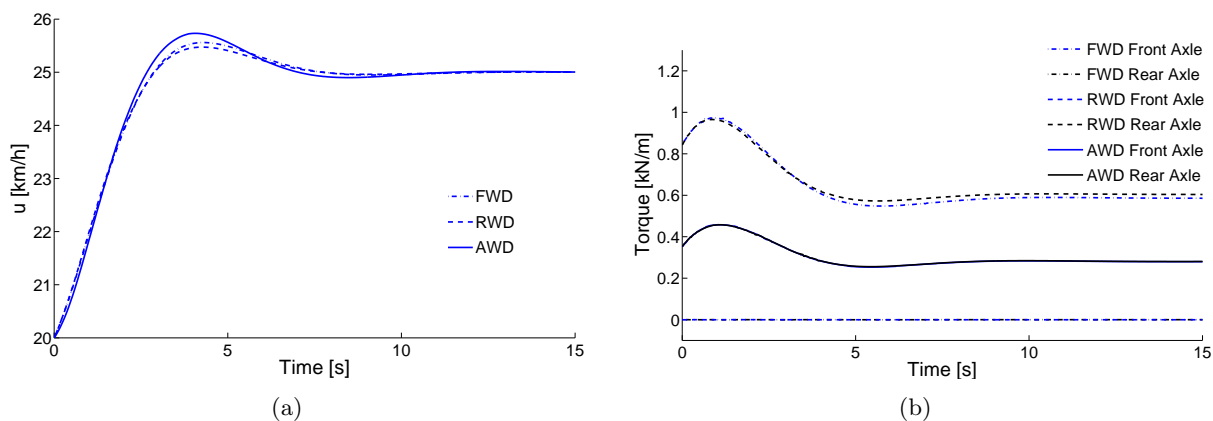


Figure 5.13: (a) Velocity profile for a vehicle running on a flat dry sand terrain. The simulation starts from a slightly lower velocity in order to reach smooth steady state conditions. (b) The torque delivered at the tires during the maneuver.

The sinkage is presented in Figure 5.14(a). The front wheels of a FWD vehicle sink considerably because they are driven ($s_d > 0$) and they negotiate a virgin patch of terrain which is less cohesive: two conditions that influence the slip-sinkage behavior. The rear

wheels have the advantage to encounter a pre-compacted, more cohesive soil; this guarantees less sinkage.

It should be mentioned that the vertical load acting on the rear wheels is marginally greater than the one acting on the front ones: evidently the greater load acting on the rear wheels is not enough to increase the sinkage (see Figure 5.14(b)). The sinkage is influenced by soil properties, vertical load, and slip phenomena: the interaction of these parameters greatly complicate the analysis.

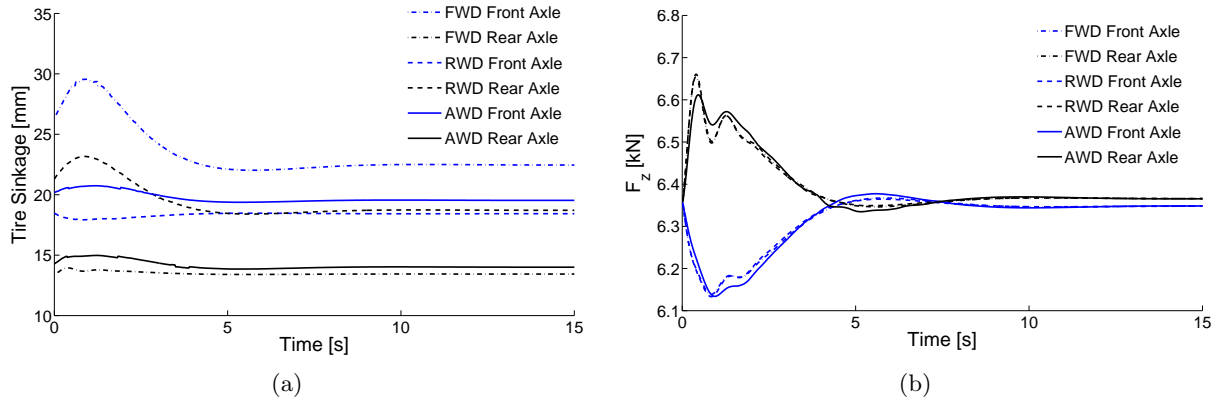


Figure 5.14: (a) Sinkage distribution for the three vehicle configurations. The value of sinkage is relative to each wheel. (b) Vertical load distribution during the maneuver. When steady state conditions are reached the load transfer phenomena still persist because the tires are still producing longitudinal forces that influence the pitch angle of the vehicle.

2WD vehicles have the handicap of the non driven wheels: these wheels, sink into the terrain and produce a negative force due to the terrain compaction, as shown in Figure 5.15(b). This causes the front (rear) wheels of the AWD (RWD) vehicle to slip significantly in order to produce the desired level of longitudinal force. Increased slip means increased sinkage and consequently poorer efficiency. The AWD vehicles, distributing the torque evenly between the front and rear axle, have more balanced performance.

The slip ratio has a direct influence on the value of tire angular velocity. Front (rear) tires of FWD (RWD) vehicles have to rotate faster (and then absorb more power) to match the velocity of the vehicle because of the slip phenomena (see Figure 5.16(a)). The instantaneous power requirement is shown in 5.16(b). The AWD vehicle is the more efficient in this particular configuration. It is interesting to notice that the FWD and the RWD vehicle tires are working close to 20% slip: this corresponds to the peak of the efficiency (see.

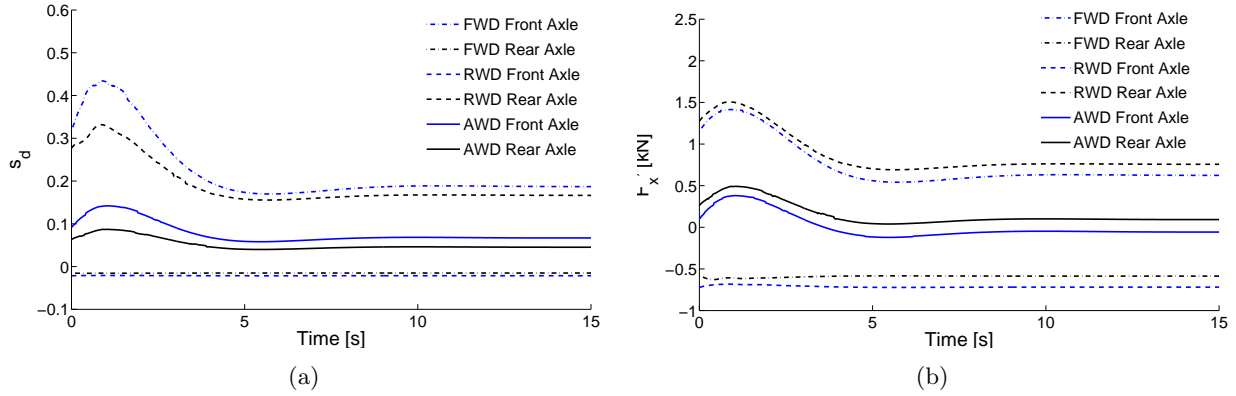


Figure 5.15: (a) Sinkage distribution for the three vehicle configurations. The value of sinkage is relative to each wheel. (b) Vertical load distribution during the maneuver. When steady state conditions are reached the load transfer phenomena still persist because the tires are still producing longitudinal forces to overcome the resistance forces; this influences the pitch angle of the vehicle.

Figure 4.5) for the tires but not for the whole vehicle. This is due to the rolling resistance of their non-drive wheel. Tests have been conducted also at 50 km/h and 100 km/h obtaining similar results. At 100 km/h the FWD and RWD vehicles would require the tires to work at more than 50% slip with power peak of 200kW: this is unpractical and it means that FWD and RWD could hardly travel at more than 50km/h on dry sand.

The influence of torque distribution on the tractive efficiency has been studied varying the torque ratio among the front and rear axle. Figure 5.17 presents the power requirement for a full range of transmission configurations. In this plot 0 % means that all the available torque is delivered to the front axle (i.e. FWD vehicle,) while 100 % means that the rear

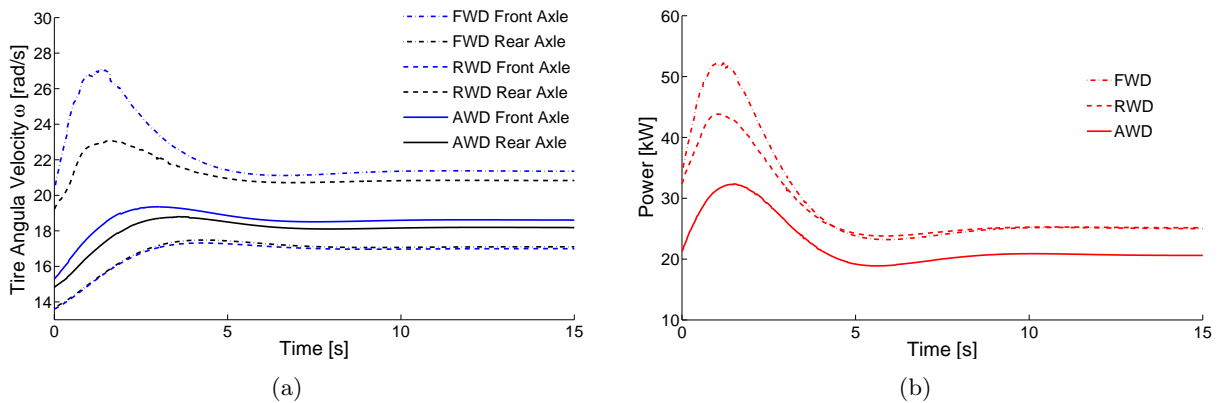


Figure 5.16: (a) Tire angular velocity and (b) instantaneous power requirement to move at 25 km/h on dry sand.

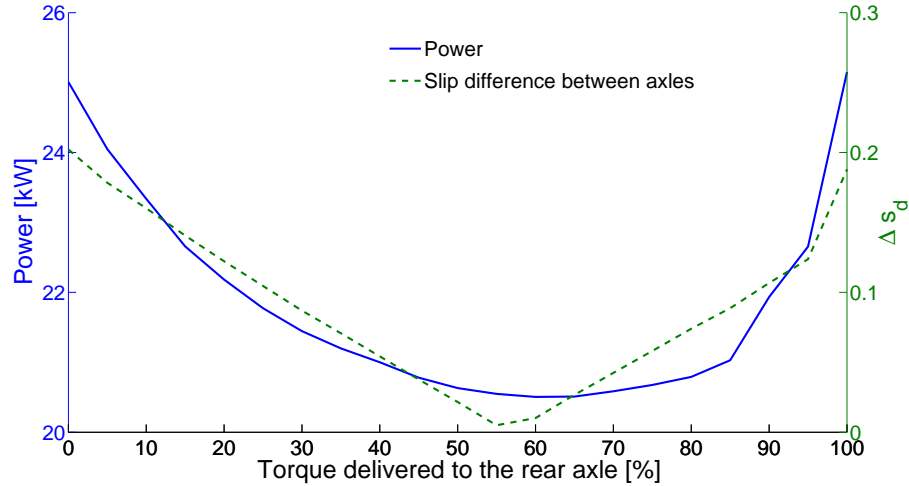


Figure 5.17: Power vs. torque distribution for a vehicle traveling at 25 km/h on flat dry sand. 0 % (100 %) on the x -axis means that the torque is fully biased on the front (rear) axle of the vehicle. On the same plot the slip difference between the front and rear axle is presented.

axle receives full torque (i.e. RWD vehicle). For a vehicle traveling at 25 km/h there is a minimum in the vicinity of 50 %. Similar trend has been observed for higher velocities. Distributing the torque slightly toward the rear axle can improve the efficiency of the vehicle without sacrificing the performance. On the same plot the slip difference between the front and rear axle is presented. The minimization of the slip difference optimizes the slip efficiency (see (4.8)) but does not necessarily improves the overall performance.

Inclined Terrain

The same analysis has been performed on a vehicle climbing a constant slope of 10 % inclination. In this scenario pure front wheel drive or rear wheel drive vehicles can't easily maintain a speed of 25 km/h. Figure 5.18 present the power vs torque distribution trend for this scenario. The trend is similar to the results obtained for flat terrain operations: the best efficiency is obtained when the torque is biased toward the rear axle.

Influence of the Static Load Distribution

The results for the torque distribution presented in Figures 5.17, 5.18 suggest that delivering more torque to the rear axle can improve tractive performance. It should be noted

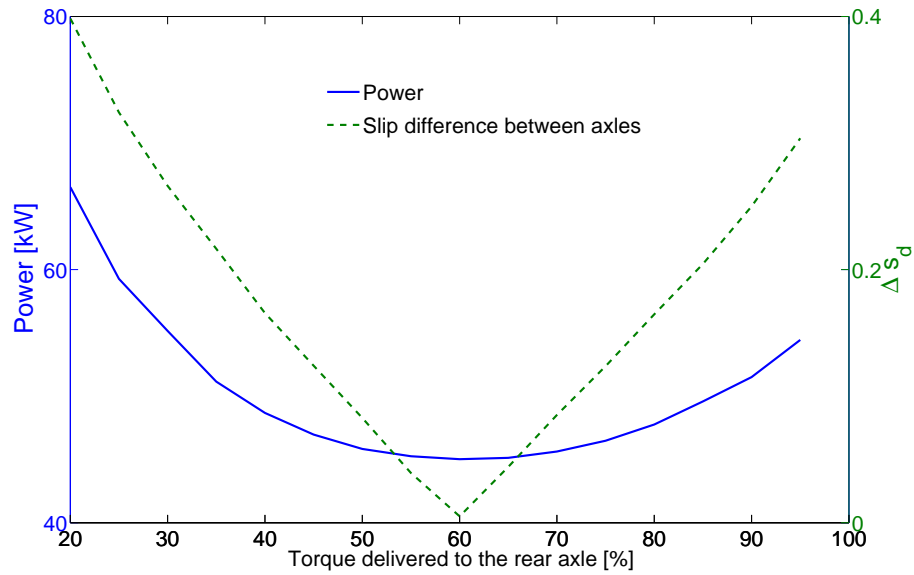


Figure 5.18: Power vs torque distribution for a vehicle traveling at 25 km/h on a 10 % incline. 0 % (100 %) on the x -axis means that the torque is fully biased on the front (rear) axle of the vehicle.

that in both cases the weight distribution during the motion was shifted to the rear axle (see Figure 5.14). In order to understand the influence of vertical load a simulation of a vehicle significantly loaded on the front axle (CG translated closer to the front axle) have been performed. The results, presented in Figure 5.19, show that the torque distribution is moderately influenced by the static load distribution: the optimum is still close to the 50% F - 50% R ratio and in spite of a significant vertical load change, has only marginally moved toward the front axle.

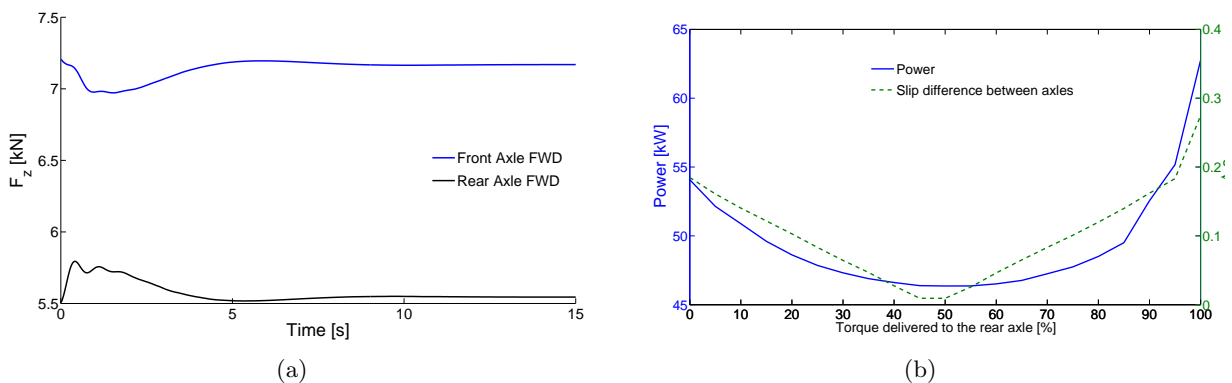


Figure 5.19: (a) Vehicle with a significant static load distribution unbalance during a straight run at 50 km/h on dry sand. (b) Power vs torque distribution among the axles.

Tire Size Influence

The efficiency has been evaluated also for tires of different dimensions. The results confirm that larger and wider tires provide better performance in off-road scenarios. Figure 5.20 presents an aggregated result obtained for an AWD vehicle running on flat dry sand at 50 km/h. The “standard” vehicle had nominal tires (radius = 0.4 m and width = 0.265 m) and torque evenly distributed among the axle (50% Front -50% Rear). The one labeled “torque optimized” adopted a torque distribution of 60 % Rear - 40% Front, while the other two vehicles adopted larger tires (radius = 0.45 m) and wider tires (width = 0.325 m). The parameter that has the strongest influence is the tire radius because it directly affects the sinkage.

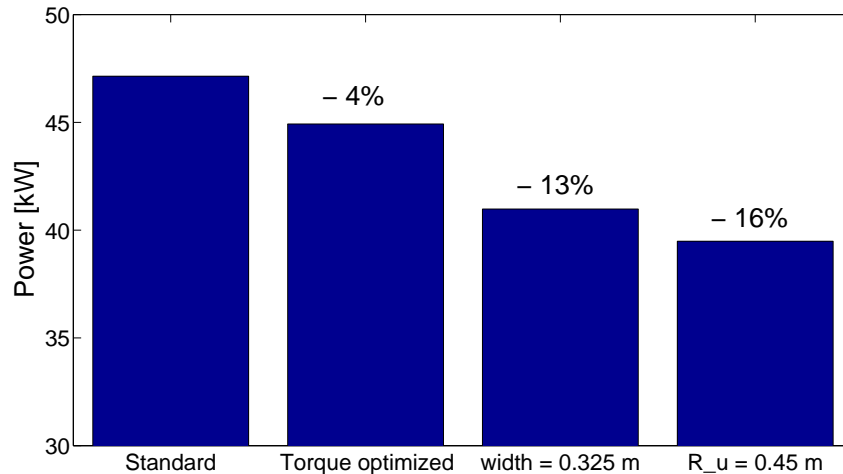


Figure 5.20: Power requirement for four vehicle configurations. Vehicle speed is 50km/h and the terrain is flat dry sand. Nominal parameters (concerning the standard case) are: Radius = 0.4 m, Width = 0.265 m, Torque = 50%F - 50% R.

However, increased tire size would imply a general increase of weight and will penalize the dynamics performance and then the consumption. Moreover, a change of tire size, would modify the kinematic ratio between tire revolutions and engine revolutions: this would require an careful analysis of the drive-line ratio. On the other hand, for vehicles with a central differential Figure 5.17 has to be considered at the design stage: a modification of the differential ratio would add no weight to the vehicle and possibly increase the efficiency. For vehicles with electric motors, mounted directly on wheels hub, the control the driving

control algorithm can directly benefit from this result.

5.3.2 Moist Yolo Loam Longitudinal

This section analyzes the motion and the efficiency of a vehicle traveling on a straight line on moist Yolo loam. The loam is a cohesive soil and the tire will always perform as a flexible tire in this section.

Flat Terrain

Figure 5.21 shows the velocity profile and the applied torque, for a vehicle that starts at 45 km/h and has to reach the target speed of 50 km/h. FWD, RWD and AWD configurations are plotted together: in every configuration the vehicle is able to reach the imposed speed. The PI controller adjust the torque correctly in order to reach the target speed.

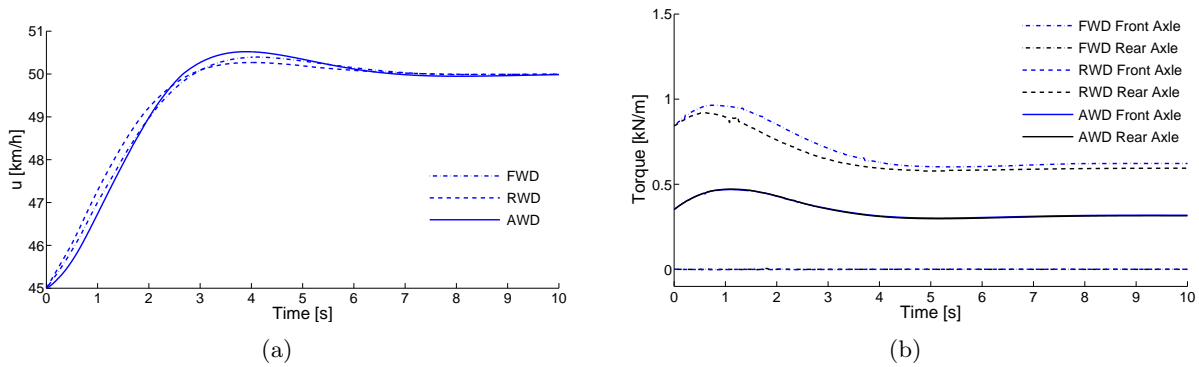


Figure 5.21: (a) Velocity profile for a vehicle running on a flat loamy terrain. The simulation starts from a slightly lower velocity in order to reach smooth steady state conditions. (b) The torque delivered at the tires during the maneuver.

The sinkage is presented in 5.22(a). For flexible tires the prediction of the sinkage is complicated by the fact that both the terrain and the tire are deforming. The sinkage value is influenced by the vertical load acting on the axle plotted in Figure 5.22(b) and by the value of the slip plotted in Figure 5.23(a). Inflation pressure, vertical load, slip, and terrain properties interact together complicating the prediction of the behavior of the vehicle. However, it is noted that the sinkage for flexible tires on moist loam is considerably smaller than the sinkage of rigid wheels on dry sand: considering the nature of the soil this

is expected.

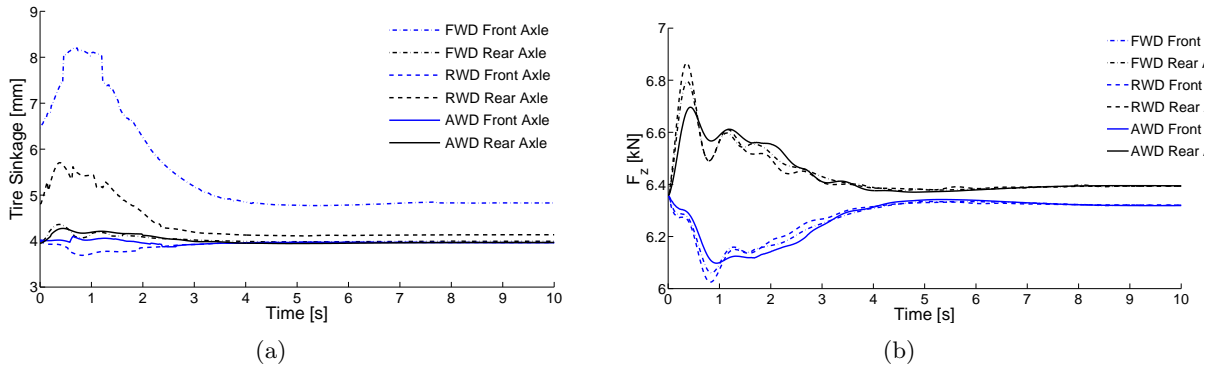


Figure 5.22: (a) Sinkage distribution for the three vehicle configurations. The value of sinkage is relative to each wheel. (b) Vertical load distribution during the maneuver. When steady state conditions are reached the load transfer phenomena still persist because the tires are still producing longitudinal forces that influence the pitch angle of the vehicle.

The reduced sinkage is compensated by the fact that the loam is a firmer soil that requires more energy to be compressed. The longitudinal force for the non driven wheels remains consistent also when traveling on moist loam, as Figure 5.23(b) shows. Also on a firmer soil the non driven wheels represent an handicap for the 2WD vehicles.

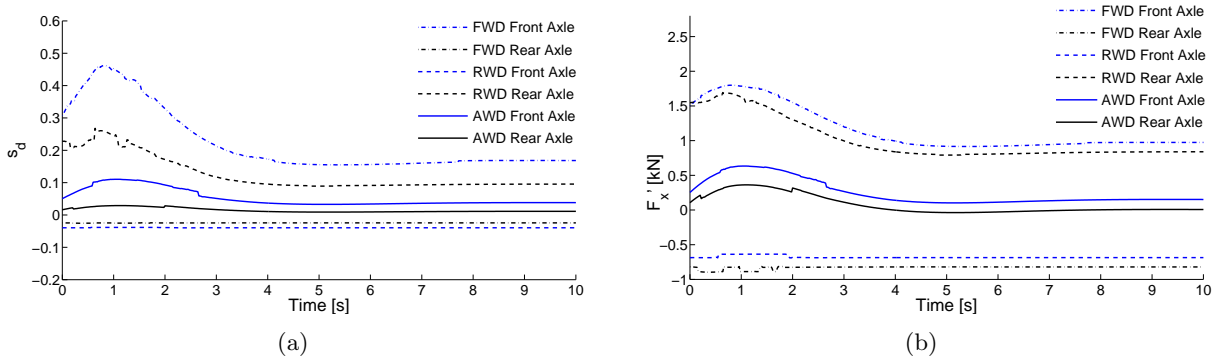


Figure 5.23: (a) Sinkage distribution for the three vehicle configurations. The value of sinkage is relative to each wheel. (b) Vertical load distribution during the maneuver. When steady state conditions are reached the load transfer phenomena still persist because the tires are still producing longitudinal forces that influence the pitch angle of the vehicle.

The slip ratio has a direct influence on the value of tire angular velocity. Front (rear) tires of FWD (RWD) vehicles have to rotate faster (and then absorb more power) to match the velocity of the vehicle because of the slip effect, as shown in Figure 5.24(a).

The instantaneous power requirement is presented in 5.24(b). The AWD vehicle is

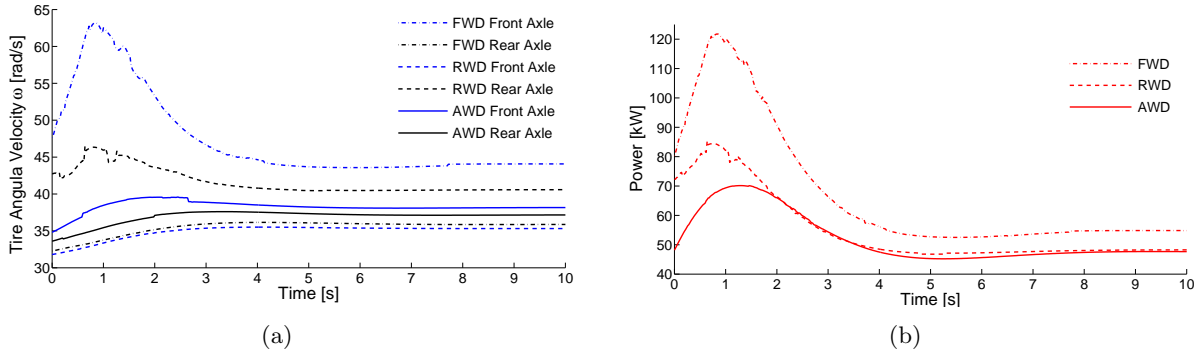


Figure 5.24: (a) Tire angular velocity and (b) instantaneous power requirement to move at 50 km/h on moist loam.

the more efficient in this particular configuration but the FWD and RWD vehicles are now closer. Flexible tires, reducing the compaction resistance of non driven wheels, improve the performance of 2 wheels drive vehicles on deformable soil. The limiting case is represented by the on-road case where the rolling resistance of the non driven wheels is extremely reduced and the 2WD configurations have better efficiency.

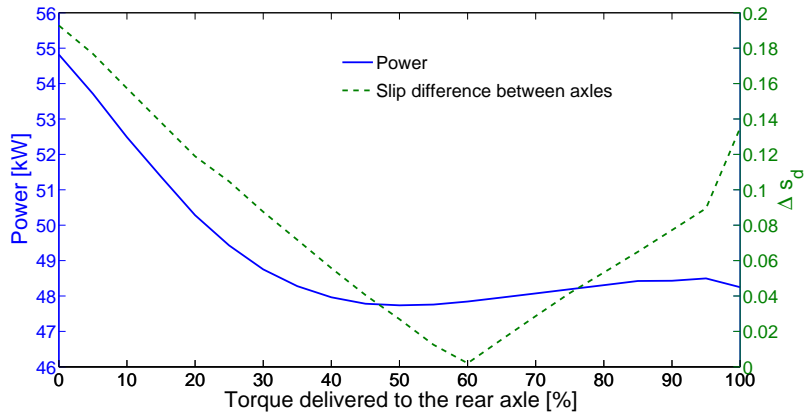


Figure 5.25: Power vs torque distribution for a vehicle traveling at 50 km/h on flat loam. 0 % (100 %) on the x -axis means that the torque is fully biased on the front (rear) axle of the vehicle.

The influence of torque distribution on the tractive efficiency has been studied varying the torque ratio among the front and rear axle. Figure 5.25 presents the power requirement for a full range of transmission configurations.

Inclined Terrain

A series of simulations for vehicles traveling on constantly inclined terrain have been performed. Road grade of 10% has been selected and the vehicle speed has been set to 50 km/h. Figure 5.26(a) shows that the RWD vehicle does not allow to comfortably reach the target speed.

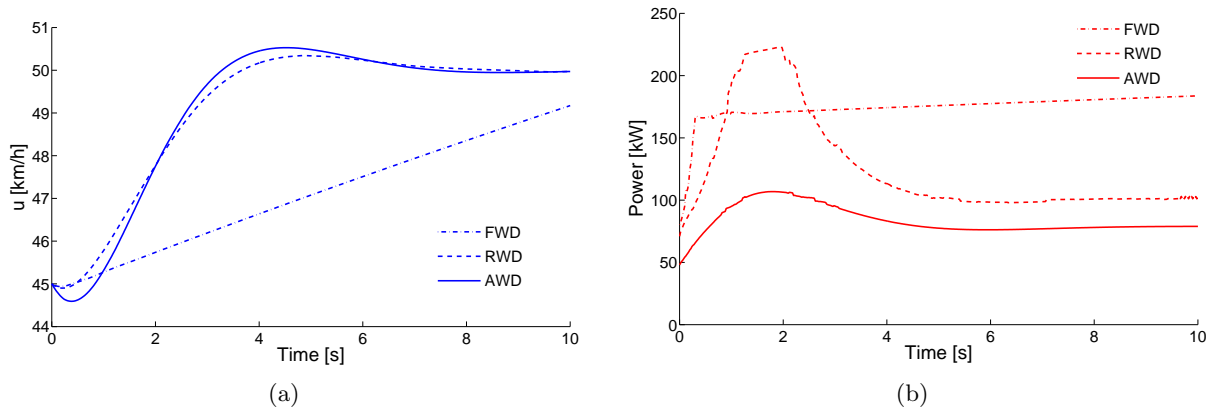


Figure 5.26: (a) Longitudinal velocity for three vehicles traveling at 50 km/h on a 10% inclined moist loam terrain. The rear wheel drive configuration does not allow to reach comfortably the desired target speed. (b) Power requirement for the same maneuver; the RWD saturates because the imposed slip ratio limit is achieved during the simulation. The FWD vehicle is able to climb the hill but it is less efficient than the AWD one.

The instantaneous power requirement plot, Figure 5.26, demonstrates that even applying an amount of power beyond 200 kW it is impossible to travel at the desired speed: tires are not able to provide enough traction. In this operational conditions the AWD vehicle provides the best performance. Figure 5.27 presents the power vs torque distribution trend for this scenario. The trend is similar to flat terrain operations: a minimum of power is observed for the the situation of torque biased toward the rear. It should be noted that on moist Yolo loam the variation of power is less significant.

Tire Inflation Pressure Influence

The tire pressure has been decreased in order to investigate its influence on the efficiency of the vehicle. Figure 5.28(a)(b) shows the sinkage and the slip for a tire inflation pressure 25% lower than the nominal one. The decrease in the inflation pressure guarantees larger contact patch area and consequently less sinkage.

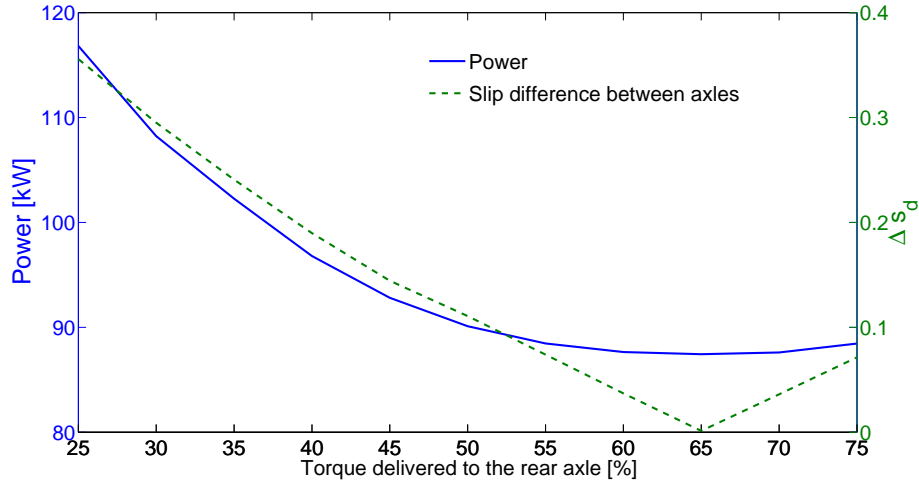


Figure 5.27: Torque distribution influence on the performance of an AWD vehicle driving at 50 km/h on a 10% inclined loam terrain. The best efficiency is reached when 60% of the total torque is delivered to the rear axle.

In this operational conditions the resistance force due to terrain compaction decreases consistently and this improves the performance. Figure 5.29 presents the longitudinal force and the instantaneous power requirement for FWD, RWD and AWD vehicles running on under-inflated tires. The AWD vehicle is the one that requires less power to be operated at 50 km/h on loamy terrain. Figure 5.30 shows the instantaneous power requirement for a large range of torque distribution. The best efficiency is reached when the torque is biased to the rear axle. Under-inflated tires provide better efficiency on off road terrain, the power requirement is about 10% less then normally inflated tires.

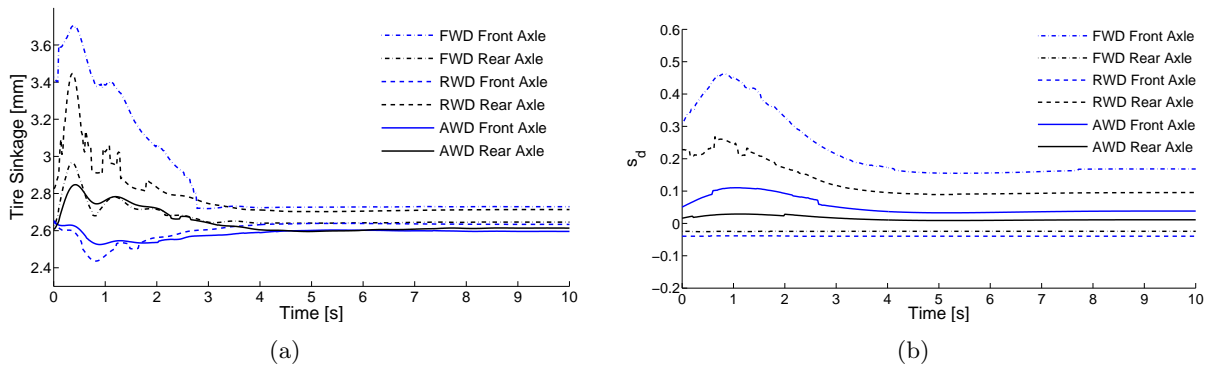


Figure 5.28: (a) Sinkage of a vehicle with decreased tire pressure traveling at 50 km/h on moist loam. (b) Slip under the same conditions.

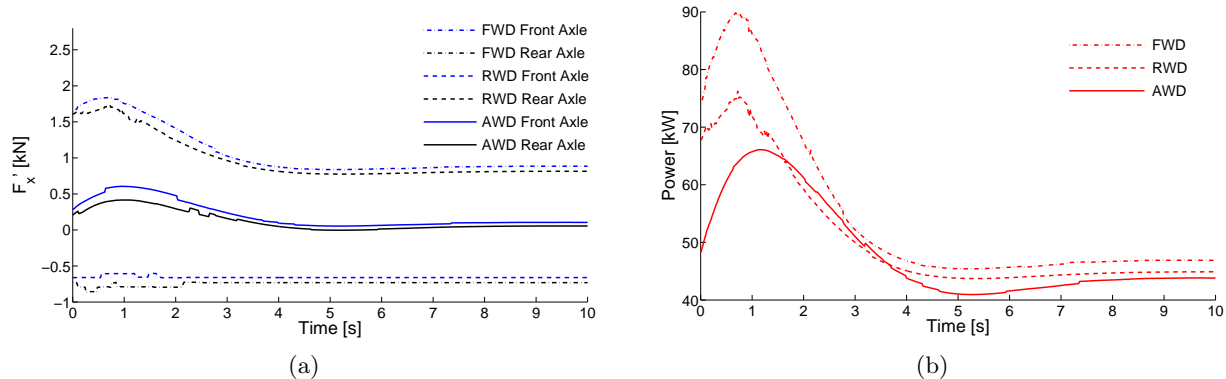


Figure 5.29: (a) Longitudinal tire forces for a vehicle with decreased tire pressure traveling at 50 km/h on moist loam. (b) Power requirement for the same maneuver.

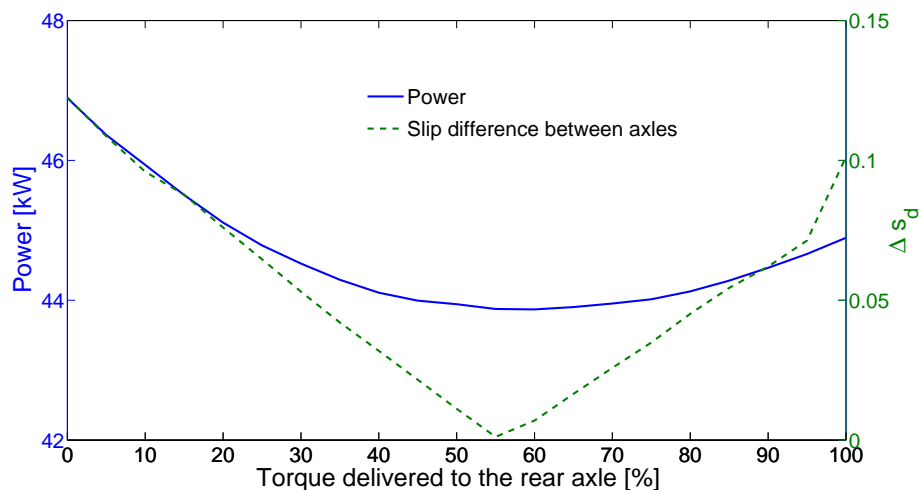


Figure 5.30: Torque distribution influence on the performance of an AWD vehicle driving at 50 km/h on a flat loamy terrain with reduced tire inflation pressure. The best efficiency is reached when 60% of the total torque is delivered to the rear axle.

5.3.3 Dry Sand Lateral

The lateral dynamics of the vehicle has been studied keeping the longitudinal velocity constant, and increasing slowly the steering angle. The steering action is showed in Figure 5.31; steering angles are zero for the first 3 seconds and increase following the Ackerman geometry (5.4) for the remaining 12 seconds. Being the steering angles are positives (see Figure 5.2), a right turn is performed. The vehicle speed is set to 50 km/h. During cornering the rear wheels do not necessarily run into the ruts created by the front ones: for this reason the rear wheels have been considered to run on unprepared virgin soil during the lateral motion

simulation.

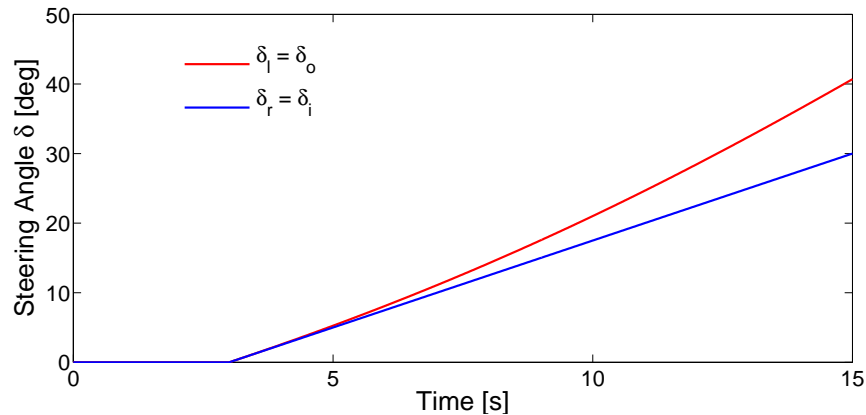


Figure 5.31: Steering action during the lateral dynamic test. The steering angles δ comply with the Ackermann steering geometry introduced in (5.4). For a right turn the outer wheel is the left one and consequently $\delta_0 = \delta_l$ and $\delta_i = \delta_r$.

Figure 5.32(a) presents the roll angle of the FWD, RWD, and AWD vehicles. The drive configuration does not affect significantly the roll angle which reaches large values toward the end of the test (the steering angle is constantly increased, the vehicle has to follow a decreasing curvature radius turn). The vertical load distribution is presented in Figure 5.32(b) and shows that the outer wheels (the left ones) are overloaded during the maneuver.

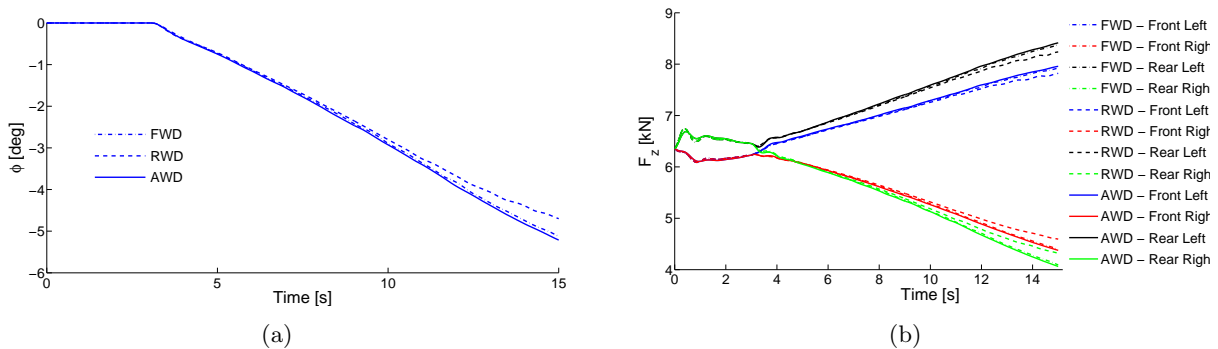


Figure 5.32: (a) Roll angle of FWD, RWD, and AWD vehicles during a right turn maneuver on dry sand. (b) The load is transferred to the outer wheels (the left ones).

Tire sinkage for this maneuver is presented in Figure 5.33(a). The outer (left) tires have to withstand more vertical load during a right turn, consequently they are sinking more. The instantaneous power requirement to complete the maneuver is presented in Figure 5.33(b). It should be noted that in normal driving conditions, most of the time is spent in straight line motion and the economy of the vehicle is primarily affected by its performance in this

working condition. Moreover, steering is an maneuver necessary to follow the road course or avoid obstacles; generally it cannot be altered arbitrarily. In this perspective Figure 5.33 can only provide general indications. AWD vehicles remain more efficient than 2WD vehicles and are less sensitive to increasing steering angle.

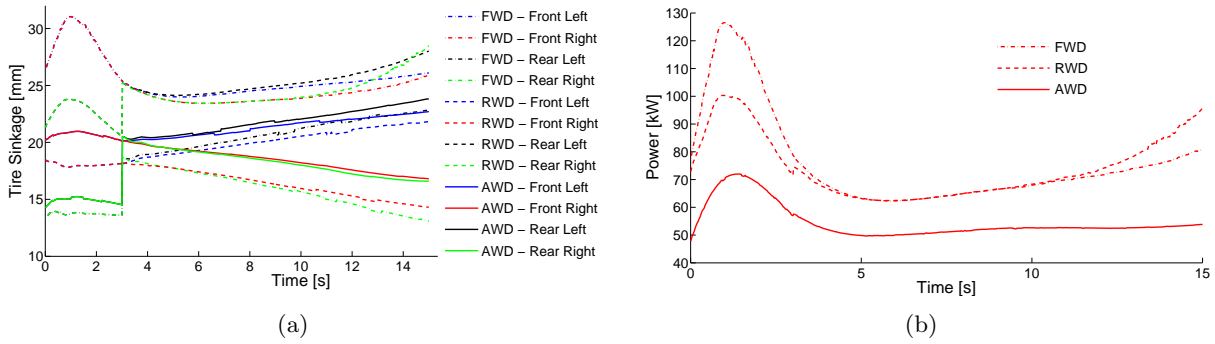


Figure 5.33: (a) Sinkage of FWD, RWD, and AWD vehicle during a right turn maneuver on dry sand. The outer wheels (left ones), being more loaded, sink more. (b) The instantaneous power requirement to complete the maneuver.

5.3.4 Moist Yolo Loam Lateral

The same maneuver showed in Figure 5.31 has been simulated for a vehicle traveling on moist Yolo loam. The longitudinal velocity has been kept constant through the PI controller; a right turn with constantly decreasing radius has been imposed. Figure 5.34(a) presents the roll angle of the FWD, RWD, and AWD vehicles. The result is similar to what it has been obtained on dry sand. The vertical load is larger on the outer wheels (the left ones), as shown in Figure 5.34(b)

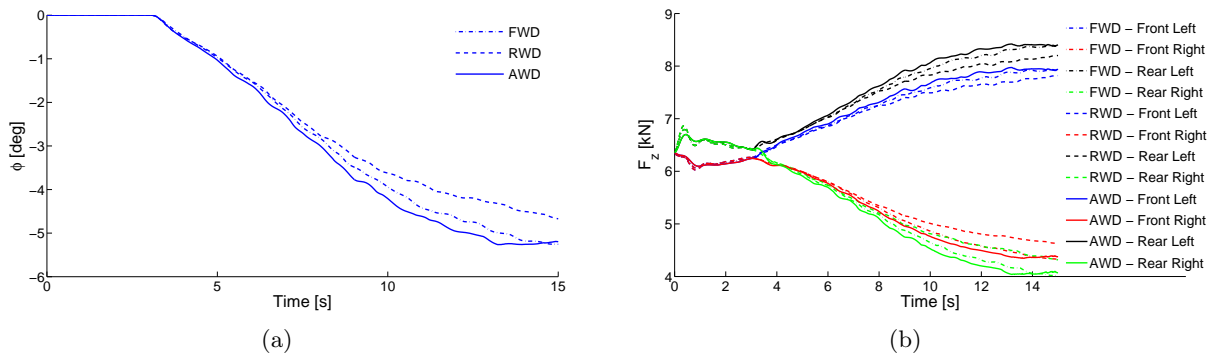


Figure 5.34: (a) Roll angle of FWD, RWD, and AWD vehicles during a right turn maneuver on moist Yolo loam. (b) The load is transferred to the outer wheels (the left ones).

Tire sinkage is reduced on moist Yolo loam (Figure 5.35(a)). The outer (left) tires have to withstand more vertical load during a right turn, consequently they are sinking more. The instantaneous power requirement to complete the maneuver is presented in Figure 5.35(b). On loamy terrain the AWD configuration provides better efficiency during cornering and, like on sandy terrain, it is less sensitive to increasing steering action.

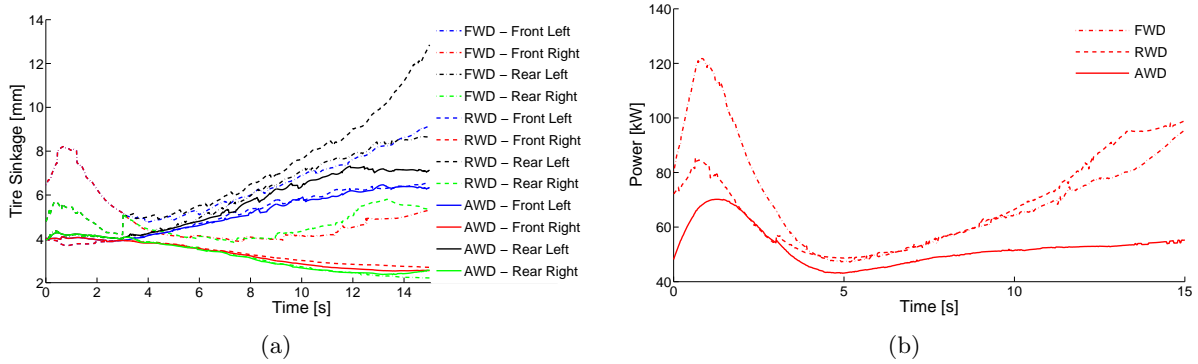


Figure 5.35: (a) Sinkage of FWD, RWD, and AWD vehicle during a right turn maneuver on moist Yolo loam. The outer wheels (left ones), being more loaded, sink more. (b) The instantaneous power requirement to complete the maneuver.

Chapter 6

Conclusions and Future Work

This chapter summarizes the contributions of this study and suggests directions for future research.

6.1 Research Summary and Contribution

This thesis established a tool for predicting mobility, handling and tractive efficiency of off-road vehicles. A semi-empirical off-road tire model, based on the work of Wong and Reece [6, 30] and Chan and Sandu [26], has been developed and modified. The model is able to predict the salient features encountered in off-road operations. The slip-sinkage behavior and the multi-pass effect have been implemented through the introduction of semi-empirical equations. The response of the model has been extensively investigated in order to verify the influence of several parameters. Variations of vertical load, tire geometry, tire inflation pressure, and soil states (i.e. multi-pass) showed that the model consistently predict tire tractive performance.

The study then moved on the analysis of a full vehicle. It has been showed that the proposed tire-model can be successfully adopted to simulate the large motion of an off-road vehicle. An analysis of the the tractive performance has been conducted. The study showed that it is possible to improve the efficiency of off-road vehicles acting on the torque distribution of the vehicle. Shifting the torque toward the rear axle can help to exploit in a

better way the tractive resources of the vehicle and obtain an improvement of the efficiency, without sacrificing the performance. This result has been obtained analyzing the vehicle with a high level of detail. The study highlighted that the motion of a vehicle can be optimized acting on torque distribution. It should be remembered that varying parameters such as the tire sizes, the static weight balance, and the torque distribution can significantly modify the response of the vehicle. This can have implications on the safety and comfort. The static load distribution influences traction but does not have a significant impact on tractive efficiency: the best tractive efficiency, under a large range of operational conditions, is reached when the torque distribution is biased toward the rear axle. This operational condition helps to optimize the slip efficiency which dominantly influences the overall tractive efficiency. This research proves that the modeling of off-road tires can have a strong impact on the design and control of off-road vehicles. Tires complex behaviors such as the multi-pass, the slip sinkage, and the parameters sensitivity cannot be ignored when analyzing off-road vehicles.

6.2 Recommendations for Future Research

Transient Maneuvering

The tire model has been developed under steady-state assumptions. In particular, the terrain semi-empirical characterization is valid for quasi-static loading conditions. Thus, there is a need to evaluate the response during transients. The problem regards both the tire and the terrain: during transient the contact patch location and shape varies and the terrain properties may not be properly described by Bekker-Reece and Janosi-Hanamoto formulations. Extending the tire model beyond steady-state assumptions will allow to realistically simulate complex maneuvers such as the J-turn or the fish-hook maneuver.

Identify the Parameters Introduced in this Thesis

This research introduced several parameters in order to relate the slip with the soil and tire properties. Experimental tests are needed to identify these parameters and fully validate the model. Soil cohesion, density, and shear modulus have to be properly characterized in order

to obtain realistic results for the multi-pass effect.

Improvement of Flexible Tire Model

The flexible tire model introduced by [26] provides a realistic computation of the tire deflected shape. However, the stress distribution along the contact patch is not necessarily consistent with the tire deformation. This happens because the tire deformation is calculated for a tire sitting on a hard surface, and the assumption that the shape stays constant during off-road motion is made. In reality, the deformation of the tire and the terrain are not two disjoint phenomena and should be considered at the same time. The approach proposed by [26] remains attractive because provides a solid, theoretical, approach but it needs to be improved in order to calculate a tire deformed shape that is consistent with the stress distribution.

Variable Tire Pressure

Variable tire pressure mechanisms (VTP) for military vehicles have been developed since War World II. Future work may exploit the results obtained in this thesis to implement control strategies for VTP systems. Differential inflation pressure among the axles might provide beneficial effects on both traction and mobility.

Differentials and in-hub Motors

In this research the differentials were considered as black-box entities. An thorough analysis of the available solutions and their implementation is suggested. Thanks to the development of lighter and more powerful electric engines, it is today possible to think about vehicles with in-hub motors. Such vehicles could directly benefit from the results obtained in this thesis. However, the vast majority of vehicles is still using mechanical coupling among the axles (even hybrid vehicles) and the study of the differentials remains a relevant topic.

Bibliography

- [1] Renewables global status report: 2009 update. Technical report, Renewable Energy Policy Network for the 21st Century, 2009.
- [2] National Research Council. Tires and passenger vehicle fuel economy. Technical report, Board on Energy and Environmental Systems, 2006. Informing Consumers, Improving Performance.
- [3] Society of Automotive Engineers. Vehicle dynamics terminology. In *SAE J670e*, Warrendale, PA, 1978.
- [4] Wheelstyres.com. <http://wheelstyres.com/> [April 2010].
- [5] C. Harnisch, B. Lach, R. Jakobs, M. Troulis, and O. Nehls. A new tyre-soil interaction model for vehicle simulation on deformable ground. *Vehicle System Dynamics*, 43(Supplement):384–394, 2005.
- [6] J. Y. Wong and A. R. Reece. Prediction of rigid wheel performance based on analysis of soil-wheel stresses, Part I. Performance of driven rigid wheels. *Journal of Terramechanics*, 4(1):81–98, 1967.
- [7] I. C. Holm. Multi-pass behaviour of pneumatic tires. *Journal of Terramechanics*, 6(3):47–71, 1969.
- [8] G. Genta. *Motor vehicle dynamics : modeling and simulation*. World Scientific, Singapore, 1997.
- [9] A. Weaver. Keynote speech: Graduate research symposium. In *26th Annual GSA Research Symposium*, Blacksburg, VA, March - 24 2010.

- [10] Toyota. *Toyota Prius website*. www.toyota.com/Prius [April 2010].
- [11] Fédération Intenationale de Motocyclisme. *FIM Road Racing World Championship Grand Prix Regulations*. www.fim-live.com, 1st edition, January 2010.
- [12] Fédération Internationale de l'Automobile. *FIA Formula One Technical Regulations*. www.fia.com, February 2010.
- [13] Ferrari. Ferrari 599 HY-Kers website. <http://www.ferrari.com> [April 2010].
- [14] Porsche. Porsche intelligent performance website. <http://www.porsche.com/microsite/intelligent-performance/usa.aspx> [April 2010].
- [15] M. L. Poulton. *Fuel Efficient Car Technology*. Computational Mechanics Publications, Southampton, 1997.
- [16] L. Guzzella. Automotive systems - an automatic control bonanza. In *American Control Conference Plenary Lecture*, Seattle, WA, June - 11 2008.
- [17] M. G. Bekker. *Theory of Land Locomotion; the mechanics of vehicle mobility*. The University of Michigan Press, Ann Arbor, 1956.
- [18] J. Y. Wong. *Theory Of Ground Vehicles*. John Wiley & Sons, New York, 3rd edition, 2001.
- [19] H. B. Pacejka. *Tire and vehicle dynamics*. SAE International, Warrendale, PA, 2nd edition, 2006.
- [20] M. G. Bekker. *Off-The-Road Locomotion; research and development in terramechanics*. The University of Michigan Press, Ann Arbor, 1960.
- [21] M. G. Bekker. *Introduction to Terrain-Vehicle Systems*. The University of Michigan Press, Ann Arbor, 1969.
- [22] Z. Janosi and B. Hanamoto. Analytical determination of drawbar pull as a function of slip for tracked vehicles in deformable soils. In *Proceedings of the 1st International Conference on Terrain-Vehicle Systems*, Turin, Italy, 1961.

- [23] J. Y. Wong. *Terramechanics and Off-Road Vehicles*. Elsevier, Amsterdam, The Netherlands, 1989.
- [24] G. N. Durham. Powered wheels in the turned mode operating on yielding soils. Technical report, US Army Waterways Experiment Station, Vicksburg, 1976.
- [25] W. Brixius. Traction prediction equations for bias-ply tires. In *Transactions of the ASAE (871622)*, St. Joseph, MI, 1987.
- [26] B. J. Chan. *Development of an off-road capable tire model for vehicle dynamics simulations*. PhD thesis, Virginia Polytechnic Institute and State University, Blacksburg, VA, 2008.
- [27] B. J. Chan and C. Sandu. A semi-analytical approach to off-road tire modeling for vehicle dynamics simulations. In *Proceedings of 16th ISTVS International Conference*, Turin, Italy, 2008.
- [28] B. J. Chan and C. Sandu. A novel wheel-soil interaction model for off-road vehicle dynamics simulation. In *Proceedings of ASME IDETC, 9th Int. Conf. on AVTT*, Sept. 4-7, 2007, Las Vegas, NV.
- [29] B. J. Chan, N. Thompson, C. Sandu, and H. Dankowicz. A novel tire-soil interaction model for simulation of off-road vehicles. In *Proceedings of 14th ISTVS International Conference*, Sept. 25-29, 2005, Hayama, Japan.
- [30] J. Y. Wong and A. R. Reece. Prediction of rigid wheel performance based on analysis of soil-wheel stresses, Part II. Performance of towed rigid wheels. *Journal of Terramechanics*, 4(2):7–25, 1967.
- [31] H. Schwanghart. Lateral forces on steered tyres in loose soil. *Journal of Terramechanics*, 1(1):9–29, 1968.
- [32] R. R. P. Hettiaratchi and A. R. Reece. Symmetrical three-dimensional soil failure. *Journal of Terramechanics*, 4(3):45–76, 1967.
- [33] K. Terzaghi, R. B. Peck, and G. Mesri. *Soil Mechanics in Engineering Practice*. John Wiley & Sons, New York, 3rd edition, 1996.

- [34] A. Grečenko. Slip and drift of the wheel with tyre on soft ground. In *Proceedings of 3rd ISTVS International Conference*, volume II, pages 76–95, Essen, Germany, 1969.
- [35] A. Grečenko. The slip and drift model of a wheel with tyre compared to some other attempts in this field. *Journal of Terramechanics*, 29(6):599–604, 1992.
- [36] C. Liang, R. W. Allen, T. J. Rosenthal, J. Chrstos, and P. Nunez. Tire modeling for off-road vehicle simulation. In *Proceedings of the 2004 SAE Automotive Dynamics, Stability & Controls Conference*, Detroit, MI, 2004.
- [37] L. L. Karafiath and E. A. Nowatzki. *Soil Mechanics For Off-Road Vehicle Engineering*. Trans Tech Publications, Clausthal, Germany, 1978.
- [38] S. Shoop, , I. Darnell, and K. Kestler. Analysis of tire models for rolling on a deformable substrate. *Tire Science and Technology*, 30(3):180–197, July 2002.
- [39] S. Shoop, K. Kestler, and R. Haehnel. Finite element modeling of tires on snow. *Tire Science and Technology*, 34(1):2–37, March 2006.
- [40] S. Oida, E. Seta, H. Heguri, and K. Kato. Soil/tire interaction analysis using fem and fvm. *Tire Science and Technology*, 2005.
- [41] H. Nakashima and A. Oida. Algorithm and implementation of soil-tire contact analysis code based on dynamic fede method. *Journal of Terramechanics*, 41:127–137, April-July 2004.
- [42] J. R. Luchini, M. M. Motil, and W. V. Mars. Tread depth effects on tire rolling resistance. *Tire Science and Technology*, 29(3):134–154, July 2001.
- [43] R. Zhang and J. Li. Simulation on mechanical behavior of cohesive soil by distinct element method. *Journal of Terramechanics*, 43(3):303–316, July 2006.
- [44] T. Koizumi, N. Tsujiuchi, and S. Mori. Simulation of grouser-soil interaction by using 3-dimensional dem considering particle roughness. In *Proceedings of 16th ISTVS International Conference*, pages 221–227, Turin, Italy, 2008.
- [45] T. D. Gillespie. *Fundamentals of vehicle dynamics*. Society of Automotive Engineers, Warrendale, PA, 1992.

- [46] M. D. Letherwood and D. D. Gunter. Ground vehicle modeling and simulation of military vehicles using high performance computing. *Parallel Computing*, 27:109–140, 2001.
- [47] R. J. Godwin, J. L. Brighton, K. Blackburn, T. E. Richards, D. Ansorge, and P. N. Wheeler. Off-road dynamics research at cranfield university at silsoe. In *ASABE Annual International Meeting*, Portland, OR, July 9-12.
- [48] Defense Advanced Research Projects Agency. Darpa urban challenge. <http://www.darpa.mil/grandchallenge/index.asp> [April 2010].
- [49] G. M. Hoffmann, C. J. Tomlin, M. Montemerlo, and S. Thrun. Autonomous automobile trajectory tracking for off-road driving: Controller design, experimental validation and racing. In *American Control Conference*, New York, NY, July 11-13 2007.
- [50] A.M. Sharaf, H. Rahnejat, and P.D. King. Analysis of handling characteristics of all-wheel-drive off-road vehicles. *Int. J. Heavy Vehicle Systems*, 15(1):89–106, 2008.
- [51] F. M. Zoz and R. D. Grisso. Traction and tractor performance. In *Agricultural Equipment Technology Conference*, volume Tractor Design, Louisville, KY, February 2003.
- [52] S. Mohan. All-wheel drive / four-wheel drive systems and strategies. In *FISITA World Automotive Congress*, Seoul, Korea, June 12-15 2000.
- [53] A. M. Sharaf, G. Mavros, H. Rahnejat, P. D. King, and S. K. Mohan. Optimisation of awd off-road vehicle performance using visco-lock devices. *Int. J. Heavy Vehicle Systems*, 15(2/3/4):188–207, 2008.
- [54] J. Yamakawa, A. Kojima, and K. Watanabe. A method of torque control for independent wheel drive vehicles on rough terrain. *Journal of Terramechanics*, 44:371–281, 2007.
- [55] A. Vivake, D. Delap, and C. Creager. The development of wheels for the lunar roving vehicle. Technical report, NASA, Glenn Research Center, Cleveland, OH, December 2009.
- [56] R. Bauer, W. Leung, and T. Barfoot. Experimental and simulation results of wheel-soil interaction for planetary rovers. In *International Conference on Intelligent Robots and Systems*, Edmonton, August 2-6 2005.

- [57] H. Nakashima, H. Fujiib, A. Oidaa, M. Momozuc, Y. Kawasea, H. Kanamorid, S. Aokie, and T. Yokoyamae. Parametric analysis of lugged wheel performance for a lunar micro-rover by means of dem. *Journal of Terramechanics*, 44(2):153–162, April 2007.
- [58] N. E. Dowling. *Mechanical Behavior of Materials*.
- [59] K. Iagnemma. *Terrain Estimation Methods for Enhanced Autonomous Rover Mobility*, chapter 17. TSI Press, July 2006.
- [60] K. Iagnemma, S. Kang, H. Shibly, and S. Dubowsky. On-line terrain parameter estimation for planetary rovers. *IEEE Transactions on Robotics and Automation*, 20(5):921–927, October 2004.
- [61] K. Iagnemma and S. Dubowsky. *Mobile Robots in Rough Terrain: Estimation, Motion Planning, and Control with application to Planetary Rovers*, volume 12 of *Springer Tracts in Advanced Robotics (STAR) Series*. Springer, June 2004.
- [62] C. Brooks and K. Iagnemma. Visual detection of novel terrain via two-class classification. In *Proceedings of the 24th Annual ACM Symposium on Applied Computing*, Honolulu, HI, March 2009.
- [63] A. Angelova, L. Matthies, D. Helmick, and P. Perona. Fast terrain classification using variable-length representation for autonomous navigation. In *IEEE Conference on Computer Vision and Pattern Recognition (CVPR)*, 2007.
- [64] J. G . Perumpral, J. B. Liljedahl, and W. H. Perloff. A numerical method for predicting the stress distribution and soil deformation under a tractor wheel. *Journal of Terramechanics*, 8(1):9–22, 1971.
- [65] B. P. Taylor. Experimental evaluation and semi-empirical modeling of the tractive performance of rigid and flexible wheels on lunar soil simulant. Master’s thesis, Virginia Polytechnic Institute and State University, Blacksburg, VA, 2009.
- [66] H. Shibly, K. Iagnemma, and S. Dubowsky. An equivalent soil mechanics formulation for rigid wheels in deformable terrain, with application to planetary exploration rovers. *Journal of Terramechanics*, 42:1–13, 2005.

- [67] D. Liang, G. Hai-bo, D. Zong, and T. Jian-guo. Wheel slip-sinkage and its prediction model of lunar rover. *J. Cent. South Univ. Technol.*, 17:129–135, 2010.
- [68] M. Loo. A model analysis of tire behavior under vertical loading and straight-line free rolling. *Tire Science and Technology*, 13(2):67–90, 1985.
- [69] Z. Yu, H. Tan, X. Du, and L. Sun. A simple analysis method for contact deformation of rolling tire. *Vehicle System Dynamics*, 36(6):435–443, 2001.
- [70] S. Gong. *A Study of in-plane Dynamics of Tires*. PhD thesis, T.U. Delft, Delft, Netherlands, 1993.
- [71] D. R. Freitag and M. E. Smith. Center-line deflection of pneumatic tires moving in dry sand. *Journal of Terramechanics*, 3(1):31–46, 1966.
- [72] M. Laysko. Slip sinkage effect in soil-vehicle mechanics. *Journal of Terramechanics*, 47:21–31, 2010.
- [73] G. Ishigami, A. Miwa, K. Nagatani, and K. Yoshida. Terramechanics-based for steering maneuver of planetary exploration rovers on loose soil. *Journal of Field Robotics*, 24(3):233–250, 2007.
- [74] Y. Fujimoto. Performance of elastic wheels on yielding cohesive soils. *Journal of Terramechanics*, 14(4):191–210, 1977.
- [75] J. I. Ramos. *Internal combustion engine modeling*. Hemisphere Pub. Corp., New York, 1989.
- [76] J. B. Heywood. *Internal combustion engine fundamentals*. McGraw-Hill, New York, 1988.
- [77] C. F. Taylor. *The internal-combustion engine in theory and practice*. M.I.T. Press, Cambridge, MA, 1985.
- [78] B. Georgi, S. Hunkert, J. Liang, and M Willmann. Realizing future trends in diesel engine development. *Society of Automotive Engineers*, (972686), August 1997.
- [79] B. Etkin. *The Dynamics of Flight, Stability and Control*. John Wiley & Sons, New York, NY, 3rd edition, 1995.

- [80] T. D. Day, S. G. Roberts, and A. R. York. SIMON: A new vehicle simulation model for vehicle design and safety research. *SAE International*, (2001-01-0503), 2001.